THERMAL MANAGEMENT OF HYBRID ELECTRICAL VEHICLES USING HEAT PIPES

Gerhardus Swanepoel

Thesis presented in partial fulfilment of the requirements for
the degree M. Sc. in Engineering
at the University of Stellenbosch

Thesis Supervisor:
R. T. Dobson

Department of Mechanical Engineering
University of Stellenbosch

November 2001

DECLARATION

I, Gerhardus Swanepoel, the undersigned, hereby declare that the work contained in this thesis is my own original work and has not previously, in its entirety or in part, been submitted at any university for a degree.

.....
Signature of candidate

26 day of NOVEMBER 2001

Abstract

In an effort to improve the fuel efficiency and to reduce emission levels of automobiles, the development of Hybrid Electrical Vehicles (HEVs) has been a major focus area of the automotive industry. The Centre of Automotive Engineering (CAE) at the University of Stellenbosch in conjunction with the Electric and Industrial Engineering Departments are currently developing an HEV. For this thesis, however, the focus is limited to the utilization of Pulsating Heat Pipes (PHPs) for the purpose of the thermal management and control of HEV components.

As part of the study of PHPs a theoretical model is developed to simulate the heat transfer rate of PHPs. Several experiments were devised to assist in the understanding of the operating principles of PHPs.

An experiment was conducted to determine the average thickness of the liquid film deposited at the trailing end of a liquid plug as it moves down a vertically orientated glass capillary tube under gravity. It was found that the average liquid film thickness varied between 100 and 200 μm for water.

The movement of a liquid plug in a vertically orientated U-shaped capillary tube due to gravity and heat transfer was experimentally investigated. It was possible to observe the deposition and the evaporation of a liquid film at the trailing end of the liquid plug with the naked eye. The movement of the liquid plug was then theoretically determined and compared to the experimental results. The theoretical model did not predict the exact movement of the liquid plug but the final steady state values was predicted within 7.39%.

The movement of a liquid plug in a horizontally orientated straight capillary tube was experimentally investigated. It was noticed that the plug exhibited a wide variety of movement ranging from irregular oscillations with amplitudes of ~ 50 mm to more steady oscillations with amplitudes of ~ 1 mm. Again it was possible to observe the deposition and evaporation of a liquid film at the trailing end of the liquid plug with the naked eye.

A PHP was manufactured using glass and filled with pentane as the working fluid. This made it possible to visually observe the fluid motion inside the PHP. It was found that the liquid plugs moved in an irregular oscillatory manner. It was also observed that two plugs

sometimes coalesce to form a single plug and that a plug can split up to form two separate plugs.

The heat transfer rate was determined for a stainless steel closed end PHP and an aluminium closed loop PHP for different working fluids, power inputs, filling ratios and inclination angles. It was found that the overall heat transfer coefficient varied between 100 and 500 W/m^2K for the stainless steel closed end PHP using water. The overall heat transfer coefficient varied between 0 and 400 W/m^2K for the aluminium closed loop PHP using water. It was found that the stainless steel closed end PHP with ammonia as working fluid was not able to transfer heat in the top heat mode. The inside diameter of the tube (3.34 mm) exceeds the required diameter of 2.96 mm which prevents liquid plugs and vapour bubbles to form causing the PHP to operate similarly to a thermosyphon. The overall heat transfer coefficient varied between 170 and 3000 W/m^2K. It is concluded that the experimentally determined heat transfer coefficients can be used to design similar PHPs in the future.

The theoretical model was used to predict the heat transfer rate of the stainless steel closed end PHP. The experimental heat transfer rate in the top heat mode was 61 W compared to 60 W predicted by the theoretical model. In the bottom heat mode the experimental heat transfer rate was 63 W compared to the predicted value of 90 W.

The theoretical model currently only caters for closed end PHPs. It is recommended that the model be extended to include closed loop PHPs.

The internal diameter of the PHPs is too great for ammonia to be used as working fluid. It is recommended that a PHP be constructed with $d_i < 2.5$ mm to allow for ammonia to be used as working fluid.

Concepts were generated for the thermal management of selected HEV components. A concept was developed for the thermal management of the HEV batteries. It was found that a Stereo-type heat lane can provide promising solutions for the thermal management of Insulated Gate Bipolar Transistors (IGBTs).

Opsomming

In 'n poging om voertuie se brandstof-benuttingsgraad te verbeter en die vlakke van uitlaatgasse te verminder word daar deur die motorvoertuigindustrie gefokus op die ontwikkeling van 'n Hibriede Elektriese Voertuig (HEV). Die Centre of Automotive Engineering (CAE) aan die Universiteit van Stellenbosch in samewerking met die Elektriese - en Bedryfsingenieurswese Departemente is tans besig met die ontwikkeling van 'n HEV. Die fokus van hierdie tesis is egter beperk tot die gebruik van Pulserende Hittepype (PHPe) vir die doel van die termiese beheer van HEV komponente.

As deel van die studie van PHPe is 'n teoretiese model ontwikkel waarmee die warmte oordragstempo van PHPe simuleer kan word. Verskeie eksperimente is prakseer om die beginsels waarvolgens PHPe werk, beter te verstaan.

'n Eksperiment was uitgevoer om die gemiddelde dikte van die vloeistof-film wat gedeponeer word by die agterkant van 'n vloeistofprop wat in 'n vertikaal georiënteerde kapillêre pypie onderworpe aan gravitasie, beweeg. Dit was gevind gewees dat die gemiddelde dikte van die vloeistof-film het gewissel tussen 100 en 200 μm vir water.

Die beweging van 'n vloeistofprop in 'n vertikaal georiënteerde U-vormige kapillêre pyp as gevolg van gravitasie en warmte-oordrag was eksperimenteel ondersoek. Dit was moontlik gewees om die deponering en verdamping van 'n vloeistof-film by die agterkant van die vloeistofprop met die oog te sien. Die beweging van die vloeistofprop was teoreties bepaal en vergelyk met die eksperimentele resultate. Die teoretiese resultate het nie die presiese beweging van die vloeistofprop voorspel nie maar die finale gestadigde posisie was voorspel binne 7.39%.

Die beweging van 'n vloeistofprop in 'n horisontaal georiënteerde reguit kapillêre pyp was eksperimenteel bestudeer. 'n Wye verskeidenheid van beweging van die vloeistofprop was waargeneem wat wissel van onreëlmatige ossilasies met amplitudes van ~ 50 mm tot meer reëlmatige ossilasies met amplitudes van ~ 1 mm. Die deponering en verdamping van die vloeistof-film by die agterkant van die vloeistofprop was weereens met die oog waargeneem.

'n PHP was van glas vervaardig en met pentaan gevul as die vloeier. Dit het dit moontlik gemaak om die vloeistofbeweging binne die PHP visueel waar te neem. Dit was gevind gewees dat die vloeistofproppe in 'n onreëlmatige ossilerende wyse beweeg. Dit was ook

waargeneem dat twee vloeistofproppe somtyds saamsmelt om een vloeistofprop te vorm en dat 'n vloeistrofprop kan opbreek om twee aparte vloeistofproppe te vorm.

Die warmte oordragstempo was bepaal van 'n vlekvrye-staal geslote ent PHP en van 'n aluminium geslote lus PHP vir verskillende vloeiers, drywing insette, vulverhoudings en inklinasie hoeke. Die algehele warmte oordragskoëffisiënt was tussen 100 en 500 W/m^2K vir die vlekvrye-staal geslote end PHP gevul met water en tussen 0 en 400 W/m^2K vir die geslote lus aluminium PHP gevul met water. Dit was gevind gewees dat die vlekvrye-staal geslote ent PHP gevul met ammoniak nie in staat was om warmte oor te dra in die boonste verhittingsmodus nie. Die binnediamter van die pyp (3.34 mm) is groter as die vereiste diameter van 2.96 mm wat verhoed dat vloeistofproppe en gasborrels gevorm word wat veroordaak dat die PHP soortgelyk aan 'n termoheuwel werk. Die algehele warmte oordragskoëffisiënt was tussen 170 en 3000 W/m^2K. Die eksperimentele bepaalde waardes vir die warmte oordragskoëffisiënte kan gebruik word vir ontwerpdoeleindes van soortgelyke PHPe in die toekoms.

Die toeretiese model was aangewend om die warmte oordragstempo van die vlekvrye staal geslote end PHP te bepaal. Die eksperimentele warmte oordragstempo in die boonste verhittingsmodus was 61 W in vergeleke met die teoretiese waarde van 60 W. In die onderste verhittingsmodus was die eksperimentele warmte oordragstempo 63 W in vergeleke met die voorspelde waarde van 90 W.

Die teoretiese model kan huidiglik slegs geslote ent PHPe simuleer. Dit word aanbeveel dat die model uitgebrei word sodat dit geslote lus PHPe ook kan simuleer.

Die binne diameter van die PHPe is te groot om ammoniak te gebruik as vloeier. Dit word aanbeveel dat 'n PHP vervaardig word met $d_i < 2.5$ mm sodat ammoniak ook gebruik kan word as vloeier.

Verskeie konsepte was gegenereer vir die termiese beheer van geselekteerde HEV komponente. 'n Konsep was ontwikkel vir die termiese beheer van die HEV batterye. Dit was gevind gewees dat 'n Stereo-type heat lane belowende oplossings kan bied vir die termiese beheer van Insulated Gate Bipolar Transistors (IGBTs).

List of Figures

List of Tables

Nomenclature

Alphabetical

A area, m^2

C_f friction factor (Fanning)

c_v specific heat at constant volume, J/kgK

c_p specific heat at constant pressure, J/kgK

d diameter, m

F force, N

h heat transfer coefficient, W/m^2K

i enthalpy, J/kg

i_{fg} latent heat, J/kg

L length, m

K curvature, m

M molar mass, kg/Kmol

m mass, kg

$\dot{m}''$ mass flux, kg/m^2s

n number

p pressure, N/m^2

q heat flux, W/m^2

$\dot{Q}$ heat transfer rate, power, W

r radius, m

t time, s

R specific gas constant, J/kgK, working fluid fill ratio, dimensionless, resistance, K/W

Re Reynolds number

$\Re$ universal gas constant, J/kmolK

T temperature, K

U overall heat transfer coefficient, W/m^2K

u internal energy, J

V volume, m^3

v velocity, m/s

W width, m

$\dot{x}$ velocity, m/s

Greek letters

δ thickness, m

ϕ Inclination angle, deg

μ viscosity, Pas

θ contact angle, deg

ρ density, kg/m^3

σ surface tension, N/m

$\hat{\sigma}$ accommodation coefficient

τ shear stress, Pa

Subscripts

a advancing

c cross sectional, condenser, contact, conduction, condensation, calculated, capillary

chan channels

cr critical

cw cooling water

d disjoining, dry

dep deposited

e evaporator

elec electrical

f film, frictional surface area, friction

i interface, inside, initial

l loss

ℓ liquid

lead leading

max maximum

min minimum

mod modified

o outside

p plug, pressure

PHP pulsating heat pipe

r receding

sat saturated

t tube, theoretical

trail trailing

v vapour

w wall

Acronyms and Abbreviations

CAE Centre for Automotive Engineering

HEV Hybrid Electrical Vehicle

IGBT Insulated Gate Bipolar Transistor

PHP Pulsating Heat Pipe

VCHP Variable Conductance Heat Pipe

1 INTRODUCTION

In an effort to improve the fuel efficiency and to reduce emission levels of automobiles, the development of Hybrid Electrical Vehicles (HEVs) has been a major focus area of the automotive industry. The Centre of Automotive Engineering (CAE) at the University of Stellenbosch in conjunction with the Electric and Industrial Engineering Departments is currently developing an HEV. HEVs typically consist of a conventional internal combustion engine combined with an electrical motor to serve as the vehicles propulsion system. To increase the fuel efficiency of the vehicle, the vehicle is driven by the internal combustion engine during parts of the drive cycle when the efficiency of the internal combustion engine is high and to switch to the electrical motor when the efficiency of the internal combustion engine is low. During braking energy is also stored in the batteries and made available later during acceleration. Due to the fact that the vehicle is powered by the electrical motor during stages of the drive cycle, the overall emission levels are reduced.

For this thesis the focus will be on the development of a theoretical model of Pulsating Heat Pipes (PHPs) and the utilization of PHPs for the thermal management of the HEV components. Patented by its inventor H. Akachi in 1990 in the USA (USA Patent Number 4,921,041), PHPs are a relatively new innovation in heat transfer technology and, like its more conventional counterparts such as thermosyphons and heat pipes, owe its low thermal resistance to the evaporation and condensation processes taking place in the device.

A literature survey was conducted to gain insight into HEVs and PHPs. Information regarding the hardware configurations and thermal requirements of HEVs was studied. Since there are no useful PHP theoretical models available, a major part of the thesis is dedicated to the development of a theoretical model of a PHP. The literature survey covers the mechanisms believed to be important for the purpose of developing a theoretical model of a PHP.

To assist in the development of a theoretical model several experiments were devised to visualise the typical fluid motion inside a PHP. A PHP was also constructed to study the effect of various parameters on the heat transfer rate of the PHP. The experimentally determined heat transfer rate is then compared with the heat transfer rate predicted by the theoretical model. A heat transfer coefficient was also defined and correlated with the different parameters affecting the heat transfer rate, to assist in the design of future PHPs.

Following the comparison of the theoretical results with the experimental results and the determination of the PHP heat transfer coefficient, several concepts are developed in which PHPs are used for the thermal management of selected components of the CAE's HEV.

After the generation of concepts for the thermal management of HEV components the results of the thesis will be discussed with conclusions. Recommendations regarding the improvement of the current experimental set-ups, the thermal management of HEVs and the course of action to be taken for future theoretical modelling of PHPs are made after the discussions and conclusions.

2 LITERATURE SURVEY

As part of the literature survey, literature regarding HEVs and PHPs was studied. Information for HEVs regarding typical hardware configurations and the thermal requirements of thermal critical components was studied. Several existing schemes for the thermal management of these components using heat pipes as well as PHPs were also obtained.

Only a few existing theoretical models of PHPs are available at present and will be discussed later in more detail. The physical phenomena that are relevant to the modelling of PHPs were studied and include the mass transfer across the interface between a liquid and vapour interface (interfacial mass transfer), the wall shear stress of a liquid plug moving in a capillary tube, capillary forces experienced by a liquid plug moving in a capillary tube and the behaviour of a liquid film sandwiched between its vapour and a solid. In addition, the chaotic nature of PHPs and the parameters affecting the performance of PHPs were studied. Parameters affecting the performance are the tube diameter, the number of channels, the filling ratio, the operating (or inclination) angle, the latent heat of the working fluid and the relationship between the saturation pressure and temperature of the working fluid.

2.1 Hybrid Electrical Vehicles

HEVs consist of a conventional petrol or diesel internal combustion engine combined with an electrical motor to serve as the propulsion system of the vehicle. Several hardware configurations exist. Depending on the hardware configuration used the thermal critical components and the associated thermal requirements can be determined.

2.1.1 Hybrid Electrical Vehicle Hardware Configurations

Several hardware configurations exist whereby the internal combustion engine is combined with the electrical motor to form the hybrid propulsion system. The major hardware configurations are series, parallel and series/parallel arrangements. The hardware configuration adopted by the CAE is the parallel configuration as shown in Figure 2.1. From Figure 2.1 it can be seen that in addition to the internal combustion engine, which is the sole source for mechanical power in conventional motor vehicles, an electrical system is added consisting of batteries, a motor controller and an electrical motor/generator. Part of the motor controller is the inverter electrical circuit which converts the direct current of the batteries to alternating current to run the electrical motor and converts alternating current from the

generator to direct current to store electrical energy in the batteries. At the core of the inverter circuit is insulated gate bipolar transistors or IGBTs

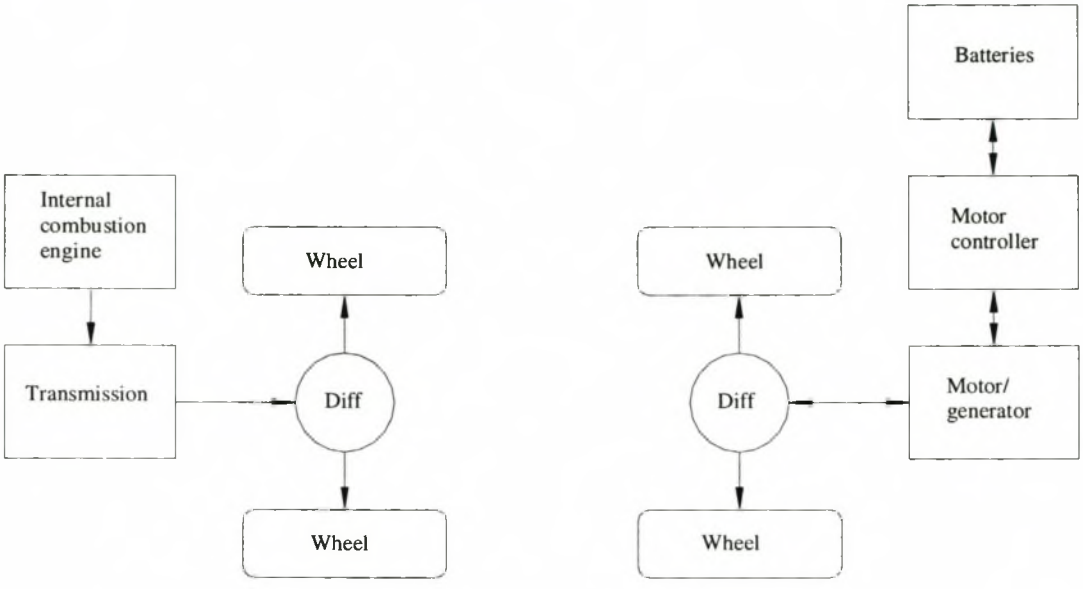

Figure 2.1 Parallel configuration of Hybrid Electrical Vehicle (Richter, 2000)

2.1.2 Thermal Requirements of Hybrid Electrical Vehicle Components

The thermal requirements of selected components are as follows

NaS batteries. During normal operation and rapid recharge heat, due to internal resistance heating, must be removed from the batteries. During quiescent periods the heat transferred to or from the battery must be adequate to maintain the temperature of the battery at an ideal temperature range in order to minimise the losses of stored energy. Ideally, the temperature of the batteries must be maintained in the region of 320 – 350°C (Burch et al., 1995).

Lead acid batteries. According to Richter (2000) the ideal operating temperature range for lead acid batteries is between 15 - 35°C.

IGBT modules. It is desirable that heat at a rate of 15 W/m^2 be removed from IGBT modules in order to maintain an ideal temperature of less than 80°C (Akachi and Polášek, 1997). According to de Villiers (2000) the case temperature of IGBTs should not exceed 100°C.

2.1.3 Thermal Management of Hybrid Electrical Vehicle Components

In order to maintain the temperature of batteries in the specified range Burch et al. (1995) uses a variable conductance insulator (VCI). A VCI basically consists of a multilayer-

vacuum insulation, similar to a Dewar flask, with a temperature dependent hydrogen source. As the temperature increases more hydrogen is supplied to the originally vacuumed space. The thermal resistance is therefore reduced by introducing thermally conducting hydrogen. At lower temperatures the hydrogen is removed to return the insulation to its original high thermal resistance state.

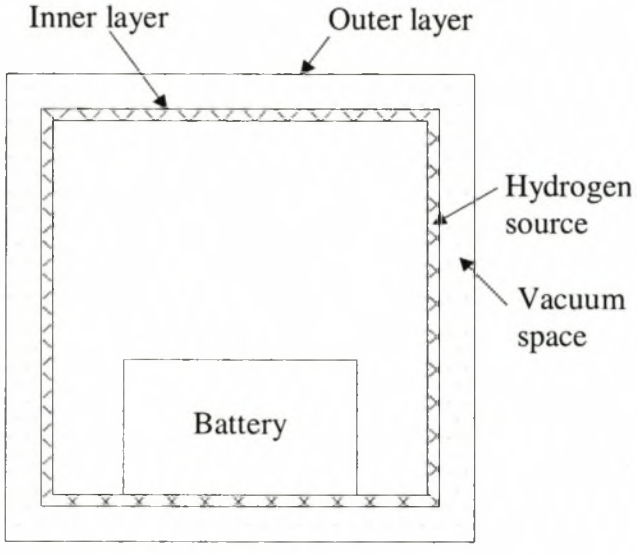

Figure 2.2 Thermal management of batteries using a VCI

Kawabata et al. (1997) uses variable conductance heat pipes (VCHP) to address the same problem. The VCHPs are connected to the batteries at the one side and to fins at the other sides as shown Figure 2.3. The difference between VCHP and a conventional heat pipe is that a reservoir of non-condensable gasses is attached to the heat pipe as shown in Figure 2.3. Due to the presence of non-condensable gasses the thermal resistance of the heat pipe will be low if the battery temperature is high but will be high when the battery temperature is low, thereby maintaining the battery temperature in the desired range.

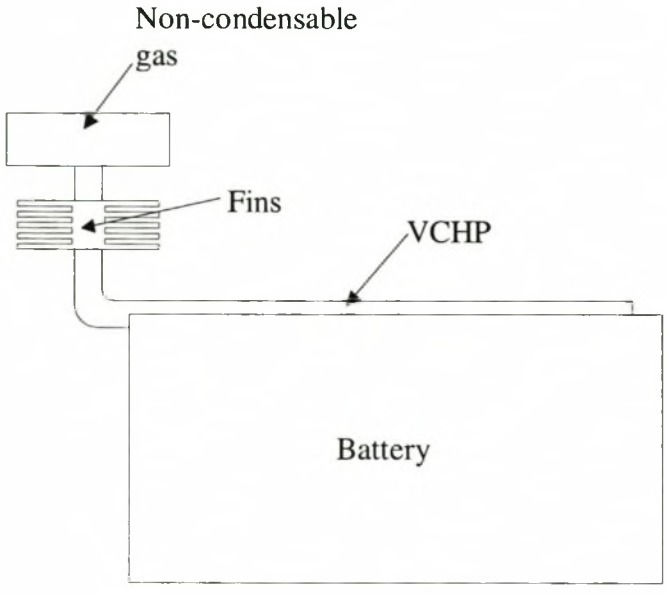

Figure 2.3 The use of variable conductance heat pipes to control the temperature of batteries (Kawabata et al., 1997)

To control the temperature of IGBTs Akachi and Miyazaki (1997) used a Stereo-type heat lane, which consists of a flat plate-like PHP, or heat lane, bent and sandwiched between two heat input plates as shown in Figure 2.4. The IGBTs are then attached to the heat input plates as shown in Figure 2.5 and are cooled using forced convection. De Villiers (2000) has evaluated the Stereo-type heat lane and concluded that the use of this device dramatically reduces the size of cooling systems currently used for the same application.

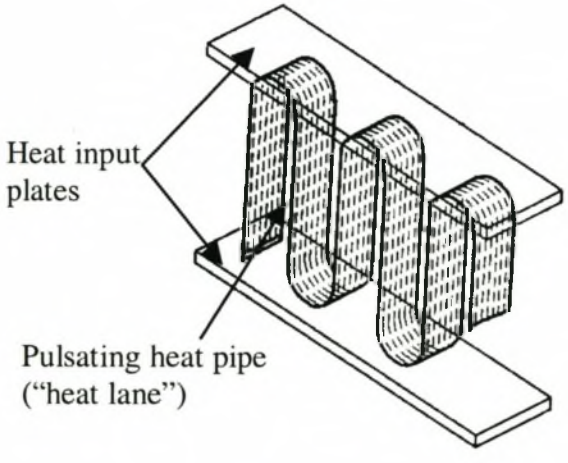

Figure 2.4 Construction of Stereo-type heat lane (Akachi and Miyazaki, 1997)

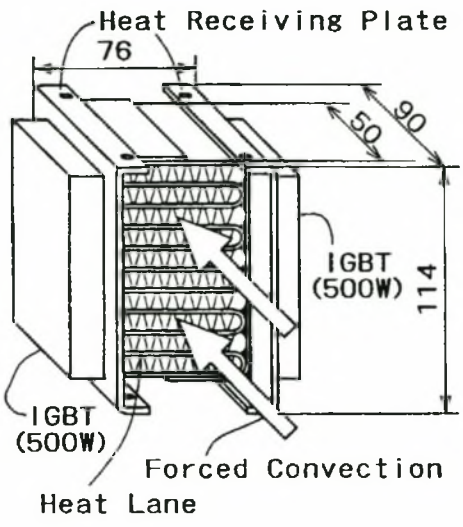

Figure 2.5 Cooling of IGBT's using a Stereo-type heat lane (Akachi and Miyazaki, 1997)

2.2 Pulsating Heat Pipes

A major part of the thesis is dedicated to the development of a theoretical model of a PHP. The mechanisms that are important for the purpose of developing a theoretical model of a PHP as well as paramaters affecting the performance of PHPs will follow.

A PHP consists of a long meandering tube filled with a working fluid as shown in Figure 2.6. In Figure 2.6 two different PHP configurations are shown, a closed loop PHP in which the tube forms a closed loop and a closed end PHP in which the tube does not form a continuous loop (Charoensawan et al., 2000). The internal diameter of the tube is in the region of the capillary length, given by $L=\left(\sigma/(\rho_\ell-\rho_v)g\right)^{0.5}$. Due to the small inside diameter and surface tension discrete liquid plugs and vapour bubbles co-exist. In the heated section evaporation takes place causing the pressure in the vapour bubbles to increase. This increase in pressure in the vapour bubbles causes pressure differentials across some of the liquid plugs. Due to these pressure differentials some of the liquid plugs will move. In the cooled section condensation takes place causing the pressure to decrease in the vapour bubbles. These decreases in pressure also causes pressure differentials across some of the liquid plugs causing those plugs to move as well. Due to the fact that all the liquid plugs and vapour bubbles are interconnected by a single tube the movement of any plug will cause neighbouring liquid plugs to move as well, causing all the liquid plugs to oscillate in an irregular aperiodic manner. The liquid plugs do not move as discrete entities all the time and some of the liquid plugs can coalesce to create a single plug or some split up to form two separate liquid plugs.

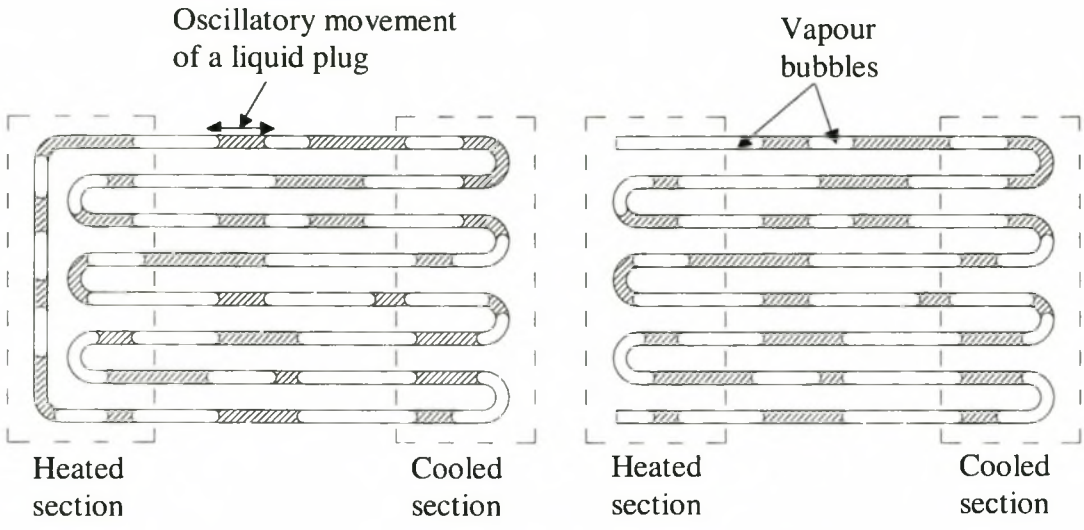

Figure 2.6 Two different PHP configurations

2.2.1 Theoretical Modelling of Pulsating Heat Pipes

Up to date very limited research has been carried out on the theoretical modelling of pulsating heat pipes. A number of theoretical modelling attempts are, however, summarised below.

Dobson and Harms (1999). In this model an open ended PHP is modelled. The PHP consists of a tube with its open ends submerged in water as shown in Figure 2.7. The tube is initially filled with liquid water. Due to symmetry only the one half of the PHP as shown in Figure 2.8 is modelled. In each half a liquid plug is present with one end exposed to vapour and the other end exposed to the water. It is assumed that a thin liquid film is present on the inner tube wall on the end where the liquid plug is exposed to the vapour. As the heat is transferred from the inner tube wall to the liquid film, the film is heated causing evaporation to take place. The portion of the film that evaporates enters the vapour causing the mass and consequently the pressure of the vapour to increase. At this stage the vapour is exposed to the heated end only. The increase in pressure causes the liquid plug to move into the water. At some stage the liquid plug moves far enough so that the vapour is exposed to the cooled end also so that vapour condenses. The mass of the vapour decreases and consequently the pressure of the vapour also decreases. At some stage the external pressure is higher than the internal vapour pressure causing the liquid plug to move back towards the evaporator section. The process is repeated causing the liquid plug to move in a chaotic oscillatory fashion. Heat

is therefore transferred from the evaporator section to the condenser section by liquid evaporating in the evaporator section and condensing in the condenser section.

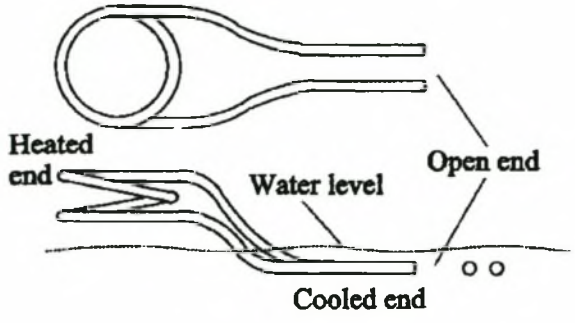

Figure 2.7 Physical configuration of the PHP model by Dobson and Harms (1999)

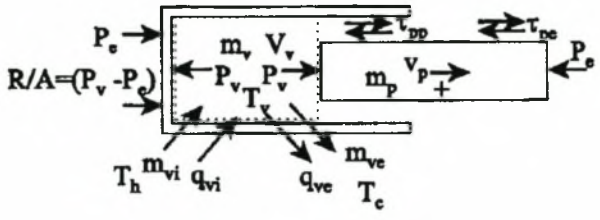

Figure 2.8 Liquid plug in one halve of PHP (Dobson and Harms, 1999)

Maezawa et al. (2000). In this model the PHP is modelled as a single loop as shown in Figure 2.9. The flow is approximated as homogeneous flow and not as discrete liquid plugs and vapour bubbles. Heat is transferred to the liquid in the evaporator section causing the liquid to evaporate and hence the vapour and quality inside the loop increase. The quality of the fluid is determined as a function of position and time. The main goal of this work was to investigate the chaotic characteristics of the theoretical developed model. The theoretical model was not experimentally validated.

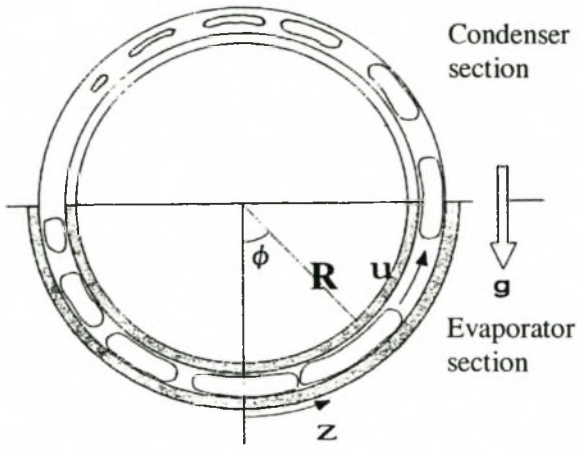

Figure 2.9 Pulsating heat pipe model by Maezawa et al. (2000)

Zuo et al. (2001) The approach used by the authors was to simplify the PHP as a structure consisting of two branches as shown in figure Figure 2.10 and to represent the liquid plugs and vapour bubbles by a single point situated at the centre of mass of the working fluid. As evaporation and condensation take place the vapour and liquid content will change in both branches. Due to the change in the amount of vapour and liquid in both branches the centre of mass changes. The PHP is therefore simulated by determining the position of the centre of mass as a function of time due to the heat transfer taking place.

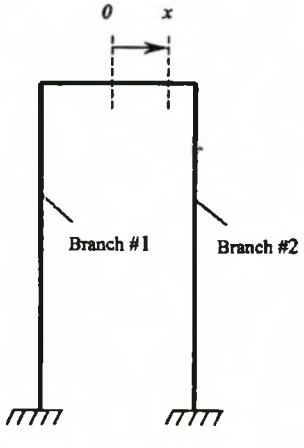

Figure 2.10 Pulsating heat pipe model by Zuo et al. (2001)

Wong et al. (1999). The model consists of discrete liquid plugs and vapour bubbles inside a tube as shown in Figure 2.11. The plugs were given an initial velocity to study the effect of this initial movement on the other plugs. The movement of the liquid plugs was therefore not induced by any heat transfer processes and the model seems of little use from a heat transfer

point of view. The modelling of the movement of the liquid plugs might be useful when modelling a PHP as a tube containing discrete liquid plugs and vapour bubbles.

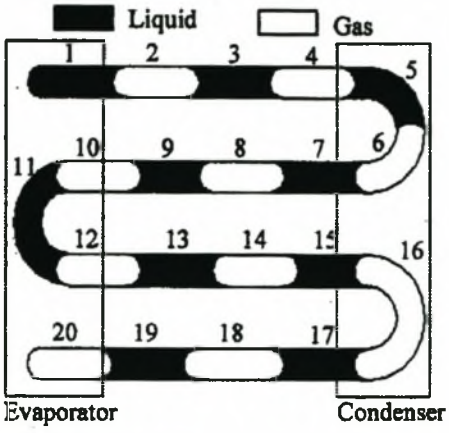

Figure 2.11 Pulsating heat pipe model by Wong et al. (1999)

2.2.2 Background Theory

It was opted to model the PHP as a tube containing several discrete liquid plugs and vapour bubbles (more or less) as shown in Figure 2.11 and to adopt a similar model for the heat transfer processes taking place as that by Dobson and Harms (1999). The mechanisms that form the building blocks for the model are the interfacial mass transfer, the wall shear stress experienced by the liquid plug as it moves, the capillary forces experienced by the liquid plug due to surface tension and the behaviour of a thin liquid film exposed to its vapour. These aspects will now be addressed.

2.2.2.1 Interfacial Mass Transfer

For a liquid film-vapour system the interfacial mass transfer is derived from the kinetic gas theory and is given by Carey (1992), Mills (1992) and Khrustalev and Faghri (1995) as:

$$\dot{m}'' = \frac{2\hat{\sigma}}{2-\hat{\sigma}} \frac{1}{\sqrt{2\pi R}} \left(\frac{p_v}{\sqrt{T_v}} - \frac{p_\ell}{\sqrt{T_\ell}} \right) \tag{2.1}$$

In equation (2.1) it is assumed that p_v and p_ℓ correspond to the saturation pressures evaluated at T_v and T_ℓ respectively. Paul (1962) has compiled a list of accommodation coefficients, $\hat{\sigma}$, for different substances (Carey, 1992). According to Paul (1962) the value of the accommodation coefficient for water is $0.02 \leq \hat{\sigma} \leq 0.04$, but according to Mills (1992)

it is now generally accepted that $\hat{\sigma} \approx 1$ provided that the water surface is not contaminated. According to Carey (1992) the lower values of $\hat{\sigma}$ are attributed to either the failure of the kinetic gas theory used to define $\hat{\sigma}$ or system contamination. According to Sukhatme and Rohsenow (1966) for a system with relatively constant contamination levels a relatively constant value of $\hat{\sigma}$ is attainable (Carey, 1992). From the statements above it can be concluded that although values of $\hat{\sigma}$ for the working fluid are known, almost unavoidable contamination levels in typical practical engineering applications will result in lower values of $\hat{\sigma}$.

According to Khrustalev and Faghri (1995) the pressure p_ℓ in equation (2.1) must be corrected for the effect of the disjoining and capillary pressure in the case of a non-horizontal liquid vapour interface where the liquid layer is relatively thin. The disjoining pressure is the difference between the liquid film pressure and the vapour pressure (Adamson, 1990) and is induced by van der Waals attractions (Burelbach et al., 1988). The corrected pressure is then given by

$$p_\ell = p_{sat}(T_\ell)\exp\left[\frac{p_\ell - p_{sat}(T_\ell) + p_d - \sigma K}{\rho_\ell R T_\ell}\right] \tag{2.2}$$

For a horizontal surface the curvature K = 0. Holm and Goplen (1979) gives the following expression for the disjoining pressure for water (Khrustalev and Faghri, 1995)

$$p_d = \rho_\ell R T_\ell \ln\left[1.5336\left(\frac{\delta_{\ell f}}{3.3}\right)^{0.0243}\right] \tag{2.3}$$

Several other equations were found in the literature which predict the mass transfer due to phase change. The following equation is given by Kobayashi et al. (1996):

$$\dot{m}'' = \frac{\hat{\sigma} i_{fg}\rho_v}{T_i\sqrt{2\pi R T_i}}\left[(T_i - T_v) + \frac{T_v}{i_{fg}\rho_\ell}(p_\ell - p_v)\right] \tag{2.4}$$

The interfacial mass flux is given by Bankoff (1990) as

$$\dot{m}'' = \frac{\hat{\sigma} i_{fg}\rho_v}{T_i^{\frac{3}{2}}}\sqrt{\frac{M}{2\pi\Re}}(T_v - T_i) \tag{2.5}$$

Dunn and Reay (1994) give the interfacial mass flux as

$$\dot{m}'' = \frac{1}{\sqrt{2\pi R T_\ell}}(p_{sat}(T_\ell) - p_v) \tag{2.6}$$

For relatively high heat fluxes, the heat flux due to phase change is attributed to Solov'ev and Kovalev (Khrustalev and Faghri, 1995) as

$$q = 3.2\sqrt{RT_v}(p_\ell - p_v) \tag{2.7}$$

2.2.2.2 Wall Shear Stress

Dobson and Harms (1999) estimated the shear stress between a moving liquid plug in a tube and the tube wall from the relation $\tau_w = C_{fp}\rho_\ell \dot{x}_p^{\,2}/2$. The coefficient of friction is given by $C_{fp} = 16/Re$ if $Re = \rho_\ell \dot{x}_p d_i/\mu_\ell \leq 1180$ otherwise $C_{fp} = 0.078Re^{-0.25}$.

For the wall shear stress Wong et al. (1999) used the same correlation $\tau_w = C_{fp}\rho_\ell \dot{x}_p^{\,2}/2$ where the friction coefficient is given by $C_{fp} = 16/Re$ if $Re \leq 2000$ but otherwise $C_{fp} = 0.25(0.0056 + 0.5\,Re^{-0.32})$.

Zuo et al. (2001) give the expression $F_{f\ell} = -8\,\mu_\ell R^2 L\pi/d_i \dot{x}_p$ for the total frictional force experienced by the liquid phase, where R is the fill ratio and L the length of the tube

2.2.2.3 Capillary Forces

The Young-Laplace equation relates the capillary pressure drop across the liquid vapour interface to the surface tension and the shape of the interface described by principle radii r_I and r_{II} (Carey, 1992):

$$\Delta p = \sigma\left(\frac{1}{r_I} + \frac{1}{r_{II}}\right) \tag{2.8}$$

Equation (2.8) can be used to estimate the capillary force experienced by a moving liquid plug in a capillary tube. A similar analysis is done by Peterson (1994) to calculate the maximum length of a stationary liquid plug in a vertical tube that can be supported against gravity, by the capillary force. Consider a moving liquid plug with the geometry as shown in Figure 2.12. It is assumed that the principle radii of the liquid plug-vapour interface at both

the receding and advancing end are the same, therefore $r_I = r_{II} = r_I$ and $r_I = r_{II} = r_2$ for the receding and advancing end respectively. From Figure 2.12 it can be seen that (if the liquid plug-vapour interface is spherical) $r_I = r_i/\cos\theta_r$ and $r_2 = r_i/\cos\theta_a$. Substituting these relationships for r_I and r_2 into equation (2.8) and simplifying, the capillary pressure difference across the vapour liquid plug interface at the receding end is $\Delta p_r = -2\sigma\cos\theta_r / r_i$ and the capillary pressure drop for the advancing end is $\Delta p_a = 2\sigma\cos\theta_a / r_i$. The pressure difference across the plug due to capillary pressure across the two vapour liquid-interfaces is given by

$$\Delta p = \Delta p_a + \Delta p_r = 2\sigma(\cos\theta_r - \cos\theta_a)/r_i = 4\sigma(\cos\theta_r - \cos\theta_a)/d_i \qquad (2.9)$$

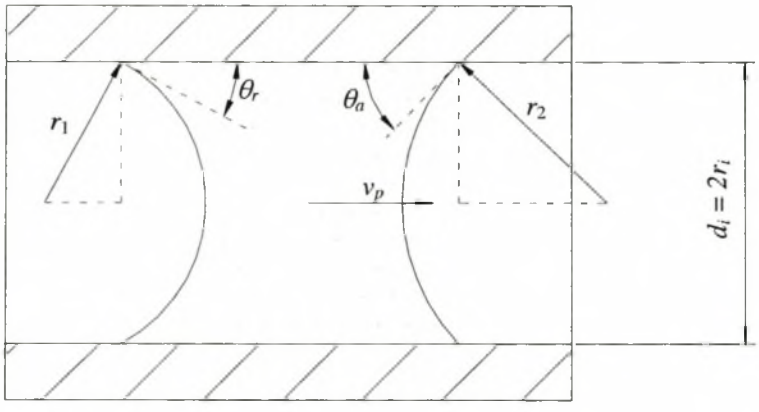

Figure 2.12 Liquid plug moving in capillary tube

The line formed where the vapour, liquid and solid phase meet is termed the contact line (Kandlikar et al., 1999). If the liquid plug is moving, θ_r and θ_a in equation (2.9) are termed *dynamic* contact angles. The typical variation of the contact angle with the velocity of the contact line, is shown in Figure 2.13 (Kandlikar et al., 1999). From Figure 2.13 it can be seen that the value of the static contact angle depends on the history of the movement of the contact line of the system and can therefore be taken as any value between θ_r and θ_a (Kandlikar et al., 1999). This nonuniqueness of the static contact angle is referred to as contact-angle hysteresis. The history of the surface across which the contact line moves can also influence the value of the advancing contact angle, i.e. the advancing contact angle of a contact line moving across a dry surface will be different from that of a contact line moving across an already wetted surface. As the velocity of the contact line increases a critical

velocity $\dot{x}_{a,cr}$ is reached where the advancing contact angle is $\theta_a = 180°$. Similarly a critical velocity $\dot{x}_{r,cr}$ exists where the receding contact angle attains a value of $\theta_r = 0°$.

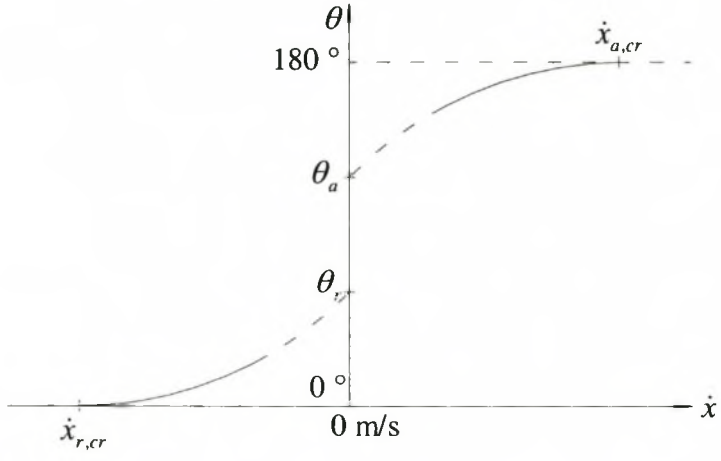

Figure 2.13 Typical variation of the contact angle with the contact line velocity (Kandlikar et al., 1999)

Some empirical correlations exist for the dynamic contact angle but it is not advisable to use them unless good similarity exists between the actual system and the one used to obtain the experimental data (Kandlikar et al., 1999). One such a correlation for the advancing contact angle, which was determined from a liquid plug moving in a capillary tube, is given by Friz (1965) and is valid only for velocities greater than 0.01 m/s (Gutoff and Kendrick, 1982)

$$\tan\theta_a = 3.4\left(\frac{\mu\dot{x}}{\sigma}\right)^{1/3} \tag{2.10}$$

For velocities less than 0.01 m/s the correlation attributed to Blake and Haynes (Gutoff and Kendrick, 1982), but which is not given there, can be used.

The advancing and receding static contact angles for several systems are shown in Table 2.1. Note that these contact angles are for horizontal surfaces.

Table 2.1 Advancing and receding contact angles for several systems. The higher values are for the advancing and lower values for the receding contact angles (Faghri, 1995).

	Acetone	Water	Ethanol	R-113
Aluminium		73/34		
Beryllium	25/11	63/7	0/0	
Brass		82/35	18/8	
Copper		84/33	15/7	
Nickel	16/7	79/34	16/7	
Silver		63/38	14/7	
Steel	14/6	72/40	19/8	16/5
Titanium		73/40	18/8	

2.2.2.4 Liquid Film Behaviour

As a liquid film evaporates it becomes thinner until a certain point where, after some perturbation or disturbance of the liquid film vapour interface, the interface becomes unstable, ruptures and droplets are formed. When the stability of thin liquid films is investigated, typically an initial perturbation is applied to the shape of the liquid film vapour interface so that the shape of the interface is sinusoidal as shown Figure 2.14 (Burelbach et al., 1988).

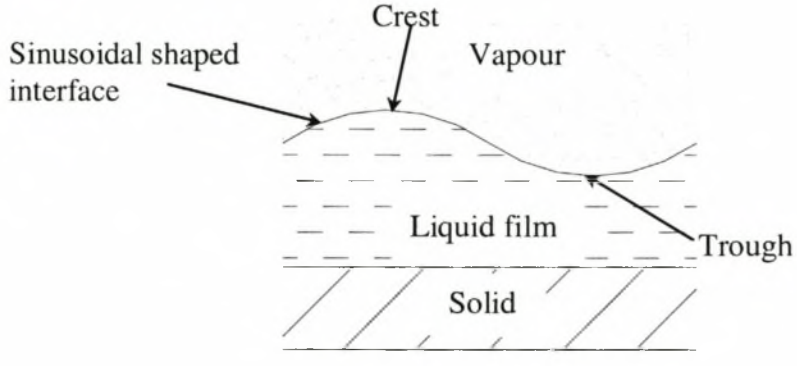

Figure 2.14 Thin liquid film with sinusoidal shaped liquid vapour interface

Several coupled mechanisms that governs the stability of the liquid film after the initial perturbation are the mass loss (evaporation) or gain (condensation) by the liquid film, vapour recoil, thermocapillary flow (Marangoni effect), disjoining pressure, surface tension and viscous forces (Burelbach et al., 1988). The contribution of these mechanisms is as follows (Burelbach et al., 1988):

Evaporation. The liquid film evaporates (blowing) until it reaches a thickness whereby other mechanisms cause the film to rupture. Evaporation also contributes to vapour recoil which has a destabilising effect on the liquid film as will be explained later.

Vapour recoil. A liquid particle moves slowly at the liquid vapour interface but accelerates when it becomes vaporised. The backward reaction on the liquid film vapour interface is termed vapour recoil. A disturbance in the liquid film vapour interface can cause an increase in the evaporation rate at a surface trough, resulting in a normal force on the interface due to vapour recoil. The pressure gradient existing due to the vapour recoil causes liquid to flow away from the trough to neighbouring crests amplifying the disturbance.

Condensation. The mass gained by the liquid film due to condensation (suction) has a stabilising effect on the liquid film. However, vapour recoil also occurs during condensation which has a destabilising effect on the liquid film (the stabilising effect of the condensation is greater than the destabilising effect of the vapour recoil).

Thermocapillary flow. If a surface tension gradient is maintained along the liquid film surface, liquid flow is induced so that the liquid flows from regions of low surface tension to regions of higher surface tension. This flow is called the Marangoni effect. If the film is heated the temperature is higher in a trough than on a crest, causing liquid to flow away (from the trough) to neighbouring crests therefore accentuating the instability, provided that for the liquid $d\sigma / dT < 0$. During condensation the temperature of the film is higher on the crest than in a through causing the direction of flow to reverse and therefore the thermocapillary flow then has a stabilising effect on the liquid film.

Disjoining pressure. As an initially thick film evaporates, it reaches a certain thickness where the disjoining pressure can cause rapid rupture of the film.

Surface tension. In an isothermal liquid film on a smooth solid substrate, the surface tension has a stabilising effect. If the surface is not smooth the radius of curvature of the film is smaller at sharp edges than at more smooth regions. Due to the difference in curvature flow is induced towards the sharp edges causing film break-up and liquid drops to form at the sharp edges.

Viscous forces. Viscous forces retard the destabilisation of the liquid film.

Gravity. For thin films (less than 0.1 mm) the effects of gravity on the stability of the film can be neglected.

2.2.3 Chaotic Behaviour of Pulsating Heat Pipes

Strogatz (1995) defines a chaotic system as follows: "When a deterministic system exhibits aperiodic behaviour that depends sensitively on the initial conditions thereby rendering long-term prediction impossible, the system is chaotic." This definition suggests that PHPs are possibly chaotic due to the observed irregular aperiodic oscillations of the liquid plugs. Indeed, it was found by Maezawa et al. (1997) that PHPs exhibit chaotic behaviour. The approach followed by Maezawa et al. (1997) can be summarised by the paragraph below.

To determine whether a system is chaotic from experimental data it is first necessary to determine whether the measured data is not periodic. This is done by determining the frequency spectrum by applying a Fast Fourier Transform (FFT) analysis to the data. If the frequency spectrum does not have a specific peak it can be concluded that the data is not periodic. The fact that the frequency spectrum does not have a specific peak can also signify white noise. To determine whether the data is white noise or not, attractors, using Takens' embedding theorem, are plotted. If the attractors expand indefinitely then the data is white noise. To determine whether the attractors are strange attractors, the sensitivity of the system to initial conditions has to be determined. The Liapunov exponent determines the sensitivity or dependence of the system on initial conditions. If the Liapunov exponent is positive then the system is sensitive to different initial conditions. If the system is sensitive to initial conditions then the attractors are strange attractors and hence the system is *chaotic*.

2.2.4 Performance Parameters of Pulsating Heat Pipes

Several parameters affect the performance of PHPs. These parameters are closely coupled and should not be considered isolated. The parameters can be summarised as follows

Tube diameter. To ensure that liquid plugs and vapour bubbles co-exist the maximum internal diameter of the tube should be less than twice the capillary length (Dobson and Harms, 1999)

$$d_i \leq 2\sqrt{\frac{\sigma}{(\rho_\ell - \rho_v)g}} \tag{2.11}$$

If the internal tube diameter is too small, the pressure required to overcome the capillary forces might be too great. From hearsay the internal diameter of the tube should be

$$1.8\sqrt{\frac{\sigma}{(\rho_\ell - \rho_v)g}} > d_i > 0.7\sqrt{\frac{\sigma}{(\rho_\ell - \rho_v)g}} \tag{2.12}$$

The lower value should be used where the PHP is subjected to a body force field of the order of 12 g's, which is typical for the aerospace industry.

Number of channels and inclination angle. According to Akachi and Polášek (1996). The thermal resistance is practically independent of the inclination angle of the PHP if the number of channels is greater than a certain minimum number of channels. For the L-KENZAN fin the minimum number of channels is n_{chan} = 80. According to Charoensawan et al. (2000) the performance of the PHP decreases as the inclination angle, as defined in Figure 2.15, is increased. The range of inclination angles tested was $0 \leq \phi \leq 90°$. The number of channels of the PHPs tested by Charoensawan et al. (2000) for different inclination angels is 24, 56 and 82.

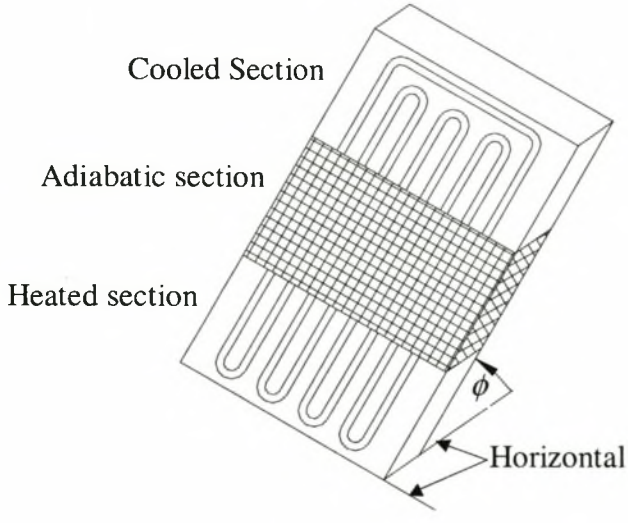

Figure 2.15 Inclination angle ϕ of the PHP as defined by Charoensawan et al. (2000)

Working fluid filling ratio. The filling ratio R is defined as the ratio of the total volume of working fluid to the total inner volume of the PHP. According to Akachi and Polášek (1996) R should be more than 50%. For their PHP configuration, Charoensawan et al. (2000) found that a filling ratio of 50 to 70% gave optimal performance. Maezawa et al. (1997) obtained good results with R = 40 - 50%.

Latent heat. According to Schneider et al. (2000) it is reasonable to believe that an optimum latent heat exists. The growth of vapour bubbles in the evaporator section is inversely proportional to the latent heat. If the latent heat of the working fluid is too high the rate of change of the volume of vapour bubbles in the evaporation section is low, which causes insufficient pressure pulses, leading to reduced oscillations. If the latent heat is too low, vapour bubbles form very fast in the evaporator section causing all the working fluid to collect in the condenser section. This problem can be overcome by increasing the fill ratio.

Saturation Curve. The relationship between the pressure and temperature at saturated condition plays a significant role in the performance of a PHP. If $(dP/dT)_{sat}$ is high it implies that small change in temperature will cause a significant change in pressure. Since the movement of the liquid plugs in a PHP is caused by the pressure differentials across the plugs, a working fluid with a high $(dP/dT)_{sat}$ ratio will perform better. The ratio $(dP/dT)_{sat}$ is much higher for ammonia than for water and is therefore preferred, to say water, from a performance point of view.

3 THEORETICAL MODELLING OF PULSATING HEAT PIPES

The pulsating heat pipe is modelled as a tube of a length L_{tube}, inside diameter d_i and outside diameter d_o, containing several liquid plugs with a vapour bubble at each end of a liquid plug, as shown in Figure 3.1. Portions of the tube may be heated, cooled or insulated and a liquid film of varying thickness $\delta_{\ell f}$ may be present on the inner wall of the tube.

For a portion of the wall covered with a liquid film, heat may be transferred from the tube wall to the liquid film. The temperature of the liquid film then increases causing evaporation to take place. The portion of the liquid film that evaporates enters the adjacent vapour bubble causing the mass and the internal energy of that vapour bubble to increase. For portions of the wall not covered with a liquid film, heat is directly transferred from the wall to the vapour bubble for the case where the wall is hotter than the vapour bubble and vice versa. If the wall is cooler than the vapour bubble, condensation can take place causing a liquid film to form on the tube wall.

The increase in the mass and internal energy of the vapour bubble causes the pressure in the vapour bubble to increase. The change in pressure is not the same for all the vapour bubbles. A situation therefore arises where the vapour pressure difference across a liquid plug causing the plug to move. As the liquid plug moves it experiences a frictional shear stress exerted by the tube wall, a force caused by the capillary pressure that exists across the liquid plug due to surface tension and a gravitational force.

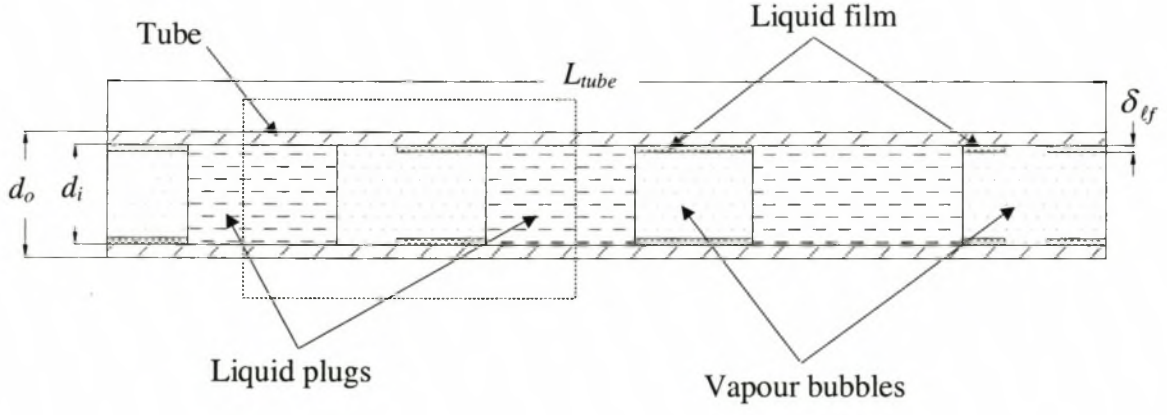

Figure 3.1 Pulsating heat pipe model

3.1 Derivation of the Governing Equations of Change

The governing equations are derived by considering the conservation of energy, momentum and mass.

3.1.1 Conservation of Energy

Consider the vapour bubble between the two liquid plugs as shown in the squared area of the tube in Figure 3.1 and shown enlarged in Figure 3.2. Consider the liquid film in Figure 3.2 as shown in Figure 3.3. Heat is transferred from the tube wall to the liquid film and from the liquid film to the vapour bubble. Evaporation of the liquid film can also take place causing mass, and hence energy, to leave the film. An energy balance on the liquid film gives

$$\frac{dU_{\ell f}}{dt} = h_{\ell fw} A_{\ell f} \left(T_w - T_{\ell f}\right) - h_{\ell fv} A_{\ell f} \left(T_{\ell f} - T_v\right) - \dot{m}''_{\ell f} A_{\ell f} i_v \tag{3.1}$$

where

$$\frac{dU_{\ell f}}{dt} = m_{\ell f} c_{v\ell f} \frac{dT_{\ell f}}{dt},\ A_{\ell f} = \pi d_i L_{\ell f},\ m_{\ell f} = \rho_{\ell f} V_{\ell f} \text{ and } V_{\ell f} = \tfrac{1}{4}\pi\left(d_o^2 - (d_i - 2\delta_{\ell f})^2\right) L_{\ell f}$$

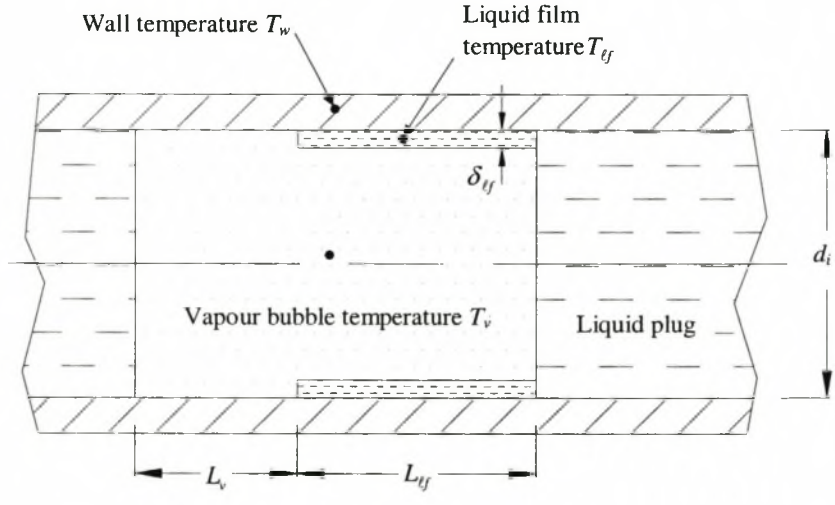

Figure 3.2 Enlarged view of a vapour bubble with adjacent dry wall and film

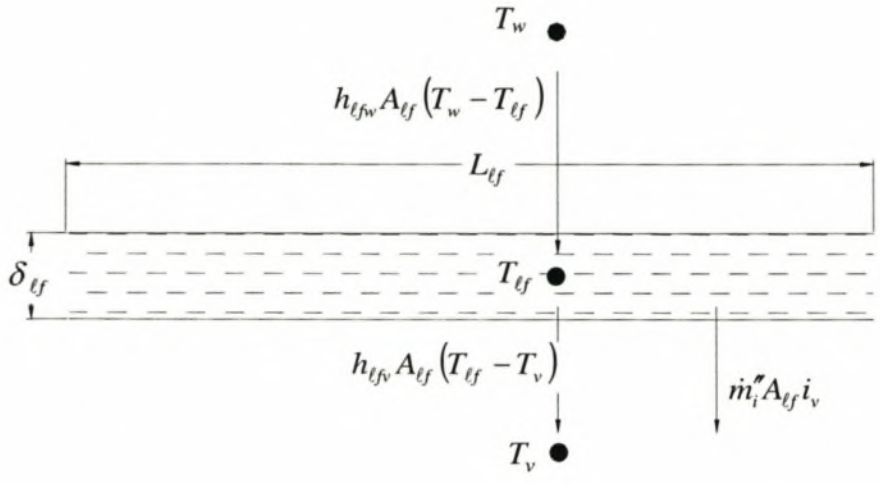

Figure 3.3 Energy balance on a liquid film

Figure 3.4 shows the heat transfer between the wall and the vapour bubble, the liquid film and the vapour bubble and the energy transfer due to mass transfer. Also shown is the work done by the vapour bubble as it expands. An energy balance on the vapour bubble gives

$$\frac{dU_v}{dt} = h_{wv} A_v (T_w - T_v) + h_{\ell fv} A_{\ell f} (T_{\ell f} - T_v) + \dot{m}_{\ell f}'' A_{\ell f} i_v - \dot{m}_{wv}'' A_v i_v - p_v \frac{dV_v}{dt} \tag{3.2}$$

where

$$\frac{dU_v}{dt} = m_v c_{vv} \frac{dT_v}{dt},\ A_v = \pi d_i L_v,\ A_{\ell f} = \pi d_i L_{\ell f},\ m_v = \rho V_v \text{ and } V_v = \tfrac{1}{4}\pi d_i^2 (L_{\ell f} + L_v)$$

(Note that the effect of the volume of the liquid film is ignored in determining the vapour bubble volume)

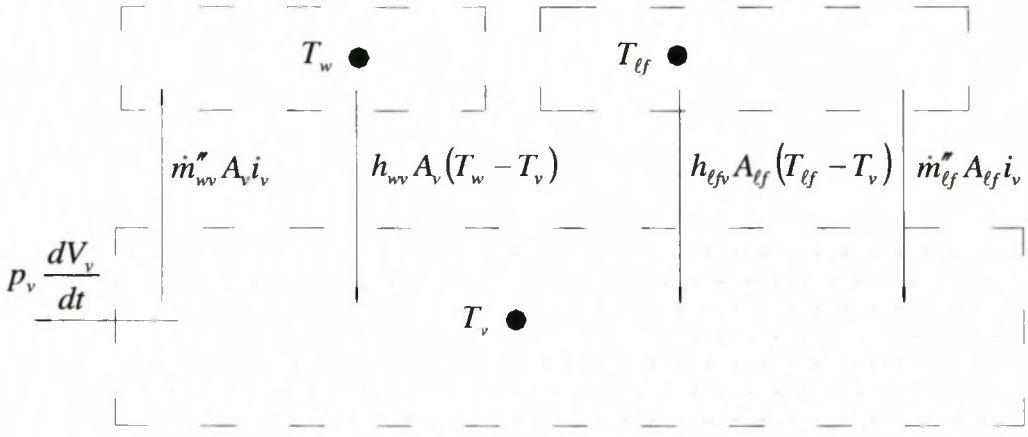

Figure 3.4 Energy balance on the vapour bubble shown in Figure 3.2

3.1.2 Conservation of Momentum

Consider a liquid plug of mass m_p as shown in Figure 3.5. A net force is exerted on the liquid plug causing it to move. As the liquid plug moves it experiences a shear stress due to friction against the tube walls. A capillary force due to surface tension, and the effect of gravity is also taken into account. A momentum balance on the liquid plug gives

$$m_p \frac{d^2 x_p}{dt^2} = p_{v1} A_c - p_{v2} A_c - \tau_w A_f + m_p g - 4\sigma(\cos\theta_r - \cos\theta_a) A_c / d_i \tag{3.3}$$

where $A_f = \pi d_i L_p$ and $A_c = \pi d_i^2/4$

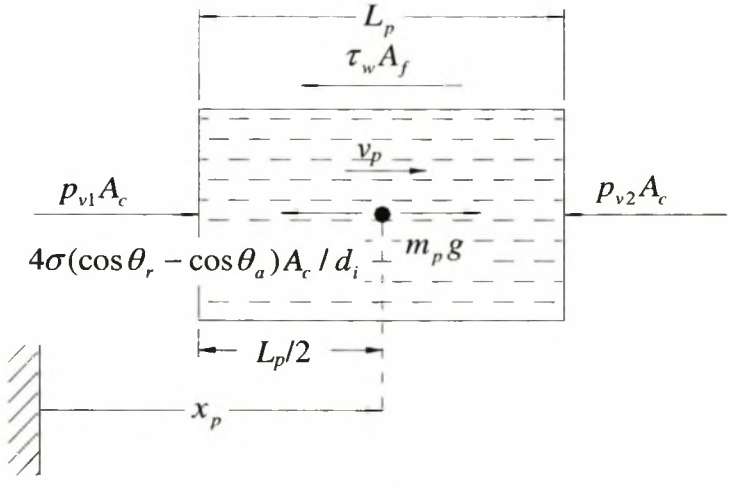

Figure 3.5 Momentum balance on a liquid plug

3.1.3 Conservation of mass

A mass balance on the liquid film shown in Figure 3.6(a) gives

$$\frac{dm_{\ell f}}{dt} = -\dot{m}''_{\ell f} A_{\ell f} \tag{3.4}$$

where $m_{\ell f} = \rho_{\ell f} L_{\ell f} \frac{1}{4}\pi\left(d_i^2 - (d_i - 2\delta_{\ell f})^2\right)$

A mass balance on the vapour bubble shown in Figure 3.6(b) gives

$$\frac{dm_v}{dt} = \dot{m}''_{\ell f} A_{\ell f} - \dot{m}''_{wv} A_v \tag{3.5}$$

where $\dot{m}''_{wv} = 0$ if $T_w > T_v$, $m_v = \rho V_v$, $V_v = \frac{1}{4}\pi d_i^2\left(L_{\ell f} + L_v\right)$, $A_{\ell f} = \pi d_i L_{\ell f}$ and $A_v = \pi d_i L_v$

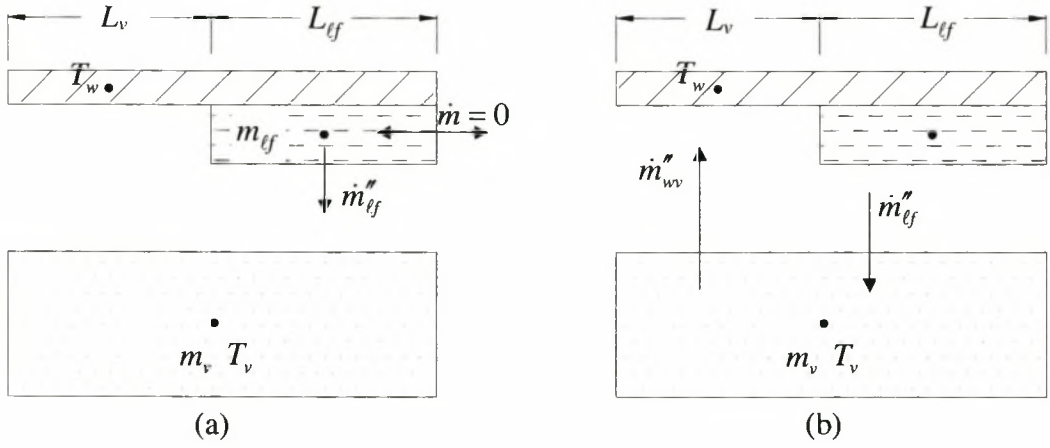

Figure 3.6 Mass balance on the liquid film and the vapour bubble

3.1.4 Liquid plug and liquid film interaction

Consider a plug moving at speed v_p as shown in Figure 3.7. Due to the curvature of the interface of the liquid plug and the liquid film with the vapour, liquid will be *pumped* from the liquid film into the liquid plug. The mass flowing into the liquid plug from the leading end will be different from that flowing into the liquid plug from the trailing end because of the difference in shape of the interface between the vapour and liquid. In addition to the pumping of liquid into the liquid plug, liquid is deposited onto the tube wall at the trailing end of the plug. To model this phenomenon it will be assumed that a film of a prescribed thickness is deposited at the trailing end, and at the leading end that a portion of the liquid

film is *sucked* into the liquid plug. These approximations will be explained later in more detail in section 3.2.

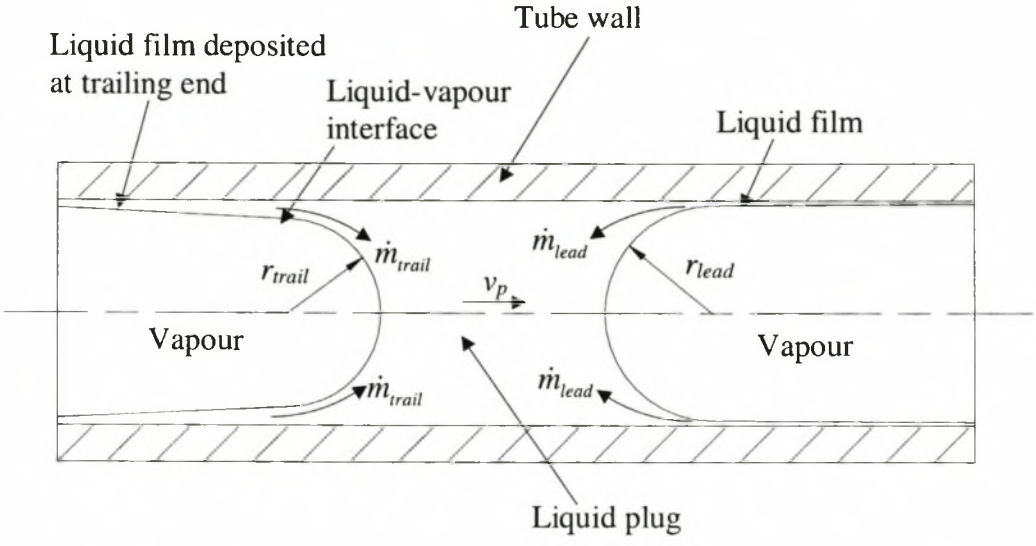

Figure 3.7 Liquid plug and liquid film interaction

3.1.5 Mass Transfer Rate

A number of different equations are given for the mass transfer rate in the literature survey (refer to section 2.2.1). Two basic types of equations are given, the one type asserts that evaporation takes place mainly as a result of a pressure difference between the liquid and vapour pressure and is derived from kinetic gas theory. For the second type the evaporation is proportional to the difference between the liquid and vapour temperature.

These two basic types of equations will be considered, a *pressure difference controlled* equation given as

$$\dot{m}''_{\ell f} = \frac{2\hat{\sigma}}{2-\hat{\sigma}} \frac{1}{\sqrt{2\pi R}} \left(\frac{p_v}{\sqrt{T_v}} - \frac{p_{\ell f}}{\sqrt{T_{\ell f}}} \right) \tag{3.6}$$

and a *heat transfer controlled* equation given as

$$\dot{m}''_{\ell f} \propto T_{\ell f} - T_v \tag{3.7}$$

The proportionality term in equation (3.7) is determined experimentally, but may be approximated as U/i_{fg} where U is the overall heat transfer coefficient and i_{fg} is the latent heat of vaporization.

3.1.6 Wall Shear Stress

The shear stress between the liquid plug and tube wall is correlated by

$$\tau_w = C_{fp}\rho_\ell v_p^{\,2} / 2 \tag{3.8}$$

where $C_{fp} = 16/Re$ if $Re = \rho_\ell v_p d_i / \mu_\ell \leq 1180$ otherwise $C_{fp} = 0.078Re^{-0.25}$.

3.1.7 Capillary Force

In order to determine the capillary force experienced by a liquid plug it is necessary to know the contact angles at the leading and trailing end of the plug. The only information available that can be easily implemented in the theoretical model is the correlation of the advancing contact angle with the plug velocity speed (refer to section 2.2.2.3). No similar information could be obtained for the receding contact angle. A simple relationship will therefore be derived for the capillary forces. From equation (2.10) it can be seen that due to the tangents in the equation that the equation break downs as the contact angle approaches $\theta_a = 90°$. Taking the advancing angle as $\theta_a = 80°$ and solving equation (2.10) for the velocity of a water liquid plug at 40°C it is found that the speed of the liquid plug is $v_p = 492$ m/s. The maximum speed of a liquid plug rarely exceeds $v_{pmax} = 10$ m/s (see section 3.3) it is therefore reasonable to believe that $\theta_a < 80°$, but it will be taken as $\theta_a = 90°$ as a worse case assumption. The smallest receding contact angle possible is $\theta_r = 0°$. Substituting these values into equation (2.9) the pressure difference will be the maximum value possible $\Delta p_{max} = 4\sigma/d_i$ Pa. If a liquid plug is stationary $\theta_a = \theta_r$ rendering the pressure difference $\Delta p = 0$. The actual pressure difference between the leading and trailing end will therefore be $0 \leq \Delta p \leq \Delta p_{max}$ depending on the velocity of the plug. It will be assumed that the relationship between the plug velocity and the capillary pressure difference due to surface tension is linear as follows

$$\Delta p = k v_p \tag{3.9}$$

where $k = \Delta p_{max} / v_{pmax}$

3.1.8 Fluid Properties

The specific heat of vapour at constant pressure is given by Yaws (1999) as

$$c_{pv} = \frac{1000}{M}\left(A + BT_v + CT_v^2 + DT_v^3 + ET_v^4\right) \text{ [J/kgK]} \tag{3.10}$$

where T_v is in Kelvin and M (molar mass of the fluid) and the coefficients are given by

Fluid	A	B	C	D	E	M [g/mole]
Pentane	26.671	0.32324	4.282E-5	-1.664E-7	5.6E-11	72.15
Water	33.933	-0.008419	2.991E-5	-1.783E-8	3.69E-12	18.015
Ammonia	33.573	-1.258E-2	8.891E-5	-7.178E-8	1.86E-11	17.03

The specific heat at constant volume is determined from the specific heat at constant pressure as

$$c_{vv} = R - c_{pv} \text{ [J/kgK]} \tag{3.11}$$

where R is the specific gas constant

The specific heat of the liquid is given by Yaws (1999) as

$$c_{p\ell} = \frac{1000}{M}\left(A + BT_\ell + CT_\ell^2 + DT_\ell^3\right) \text{ [J/kgK]} \tag{3.12}$$

where T_ℓ is in Kelvin and M (molar mass of the fluid) and the coefficients are given for different fluids by

Fluid	A	B	C	D	M [g/mole]
Pentane	80.641	6.2195E-1	-2.2682E-3	3.7423E-6	72.15
Water	92.053	-3.9953E-2	-2.1103E-4	5.3469E-7	18.015
Ammonia	-182.157	3.3618	-1.4398E-2	2.03715E-5	17.03

The density of the liquid is given by Yaws (1999) as

$$\rho_\ell = 1000AB^{-(1-T_\ell/T_c)^n} \text{ [kg/m}^3\text{]} \tag{3.13}$$

where T_ℓ is in Kelvin and A, B, T_c (critical temperature) and n are given for different fluids by

Fluid	A	B	T_c [K]	n
Pentane	0.23143	0.26923	469.65	0.28215
Water	0.3471	0.274	647.13	0.28571
Ammonia	0.23689	0.25471	405.65	0.2887

The viscosity of the liquid is given by Yaws (1999) as

$$\mu_\ell = 0.001 \cdot 10^{A+B/T_t+CT_t+DT_t^2} \text{ [Pas]} \tag{3.14}$$

where T_ℓ is in Kelvin and the coefficients for different fluids are given by

Fluid	A	B	C	D
Pentane	-7.1711	747.36	2.1697E-2	-2.7176E-5
Water	-10.2158	1.7925E3	1.773E-2	-1.2631E-5
Ammonia	-8.591	8.764E2	2.681E-2	-3.612E-5

The surface tension of the liquid is given by Yaws (1999) as

$$\sigma_\ell = 0.001A\left(1 - T_\ell / T_c\right)^n \text{ [N/m]} \tag{3.15}$$

where T_ℓ is in Kelvin and the coefficients for different fluids are given by

Fluid	A	T_c	n
Pentane	52.09	469.65	1.2054
Water	132.674	647.13	0.955
Ammonia	100.098	405.65	1.2222

The enthalpy of vaporization is given by Yaws (1999) as

$$i_{fg} = \frac{10^6}{M} A\left(1 - T / T_c\right)^n \text{ [J/kg]} \tag{3.16}$$

where T is in Kelvin and the coefficients for different fluids are given by

Fluid	A	T_c [K]	M [g/mole]	n
Pentane	39.854	469.65	72.15	0.398
Water	52.053	647.13	18.015	0.321
Ammonia	31.523	405.65	17.03	0.364

3.2 Solution of Equations

Equations (3.1) to (3.5) are numerically solved using an explicit finite difference numerical scheme. To solve these equations numerically the PHP is divided into elements of length ΔL each that $L_{tube} = n_{elements}$ x ΔL. The energy equation for a liquid film element in explicit finite difference form is (note that for convenience only the new superscripts $t + \Delta t$ are included in the equations)

$$T_{\ell f}^{\,t+\Delta t} = \frac{\Delta t}{m_{\ell f} c_{v\ell f}} \left[h_{\ell fw} A_{\ell f} \left(T_w - T_{\ell f} \right) - h_{\ell fv} A_{\ell f} \left(T_{\ell f} - T_v \right) - \dot{m}''^{\,t+\Delta t}_{\ell f} A_{\ell f} i_v \right] + T_{\ell f} \tag{3.17}$$

In (3.17) the mass flux $\dot{m}''^{\,t+\Delta t}_{\ell f}$ can be given by either the kinetic mass transfer model (pressure difference controlled) equation (3.6) or the heat transfer controlled mass transfer model equation (3.7). If the kinetic mass transfer model is used it is assumed that the pressure of the liquid film, $p_{\ell f}$, is the saturation pressure evaluated at the liquid film temperature $T_{\ell f}$. For both mass transfer models the mass flux is positive for evaporation and negative for condensation. When evaporation takes place, i.e. the mass flux is positive, the enthalpy of the vapour i_v is assumed to be the enthalpy of vapour at $T_{sat} = T_{\ell f}$ and $p_{sat} = p_{\ell f}$. When condensation takes place, i.e. the mass flux is negative, the vapour bubble can be superheated and therefore it is necessary to account for the superheat. For condensation the enthalpy is then given by

$$i_v = \left(i_v \right)_{@\, p_{sat} = p_v} + \bar{c}_{pv} \left(T_v - \left(T_{sat} \right)_{@\, p_{sat} = p_v} \right) \tag{3.18}$$

where $\bar{c}_{pv}$ is the specific heat of the vapour at constant pressure and is approximated by $\frac{1}{2}\left((c_p)_{@T_v} + (c_p)_{@T_v = T_{sat} @\, p_v} \right)$

The enthalpy as calculated from (3.18) is compared to values obtained from thermodynamic tables in Çengel and Boles (1989) in APPENDIX D. For the case where a wall element is exposed to a vapour bubble and the wall temperature is cooler than the vapour temperature it is assumed that condensation will take place. But since there is not a liquid film present, it is not possible to do an energy balance on the liquid film. It is therefore assumed that in this case the temperature of the newly formed liquid film can be taken the same as the vapour bubble temperature

$$T_{\ell f}^{\,t+\Delta t} = T_v \tag{3.19}$$

The kinetic mass transfer model is derived from the kinetic theory of gases and is therefore only valid at the interface of a liquid-vapour system. For the case where there is no film present the vapour is now in contact with a solid and not a liquid. Equation (3.6) is therefore not valid when condensation takes place on a wall element. The following will be used to model the condensation onto a dry tube wall element

$$\dot{m}_{\ell f}''^{t+\Delta t} = \frac{h_c}{i_{fg}}\left(T_{\ell f} - T_v\right) \tag{3.20}$$

where h_c is the heat transfer coefficient between the vapour and the wall

The latent heat i_{fg}, in (3.20) has to be adjusted to take into account that the vapour bubble might be in a superheated state and is given by the following

$$i_{fg} = \left(i_{fg}\right)_{@\ p_{sat}=p_v} + \bar{c}_{pv}\left(T_v - \left(T_{sat}\right)_{@\ p_{sat}=p_v}\right) \tag{3.21}$$

The mass of a film element at the new time step is obtained from (3.4)

$$m_{\ell f}^{\ t+\Delta t} = -\dot{m}_{\ell f}''^{t+\Delta t} A_{\ell f} \Delta t + m_{\ell f} \tag{3.22}$$

The energy and mass transferred from all the wall and liquid film elements to the vapour bubble must be summated to obtain the total energy and mass transferred to the vapour bubble. The energy equation of the vapour bubble is expressed in the form of the following finite difference equation:

$$T_v^{\ t+\Delta t} = \frac{\Delta t}{m_v c_{vv}}\left(\sum_{k=1}^{n_{wc}} h_{wv} A_v \left(T_w - T_v\right) + \sum_{j=1}^{n_{lf}}\left(h_{\ell fv} A_{\ell f}\left(T_{\ell f} - T_v\right) + \dot{m}_{\ell f}'' A_{\ell f} i_v\right) - \sum_{l=1}^{n_{wm}} \dot{m}_{wv}'' A_v i_v - p_v \frac{V_v - V_v^{\ t-\Delta t}}{\Delta t}\right) + T_v \tag{3.23}$$

where n_{wc} is the number of areas where heat is transferred from the wall to the vapour bubble, $n_{\ell f}$ is the number areas where the film is in contact with a vapour bubble and n_{wm} is the number of dry areas onto which condensation may take place.

From the momentum equation, equation (3.3), the new velocity of the plug in explicit finite difference form is

$$\dot{x}_p^{\ t+\Delta t} = \frac{\Delta t}{m_p}\left(p_i A_c - p_{i+1} A_c - \tau_w A_f + m_p g - 4\sigma(\cos\theta_r - \cos\theta_a) A_c / d_i\right) + \dot{x}_p \tag{3.24}$$

The wall shear friction, τ_w, in (3.24) is taken as $\tau_w = \frac{1}{2} C_{fp} \rho_\ell \dot{x}_p^{\,2}$ where the liquid plug friction coefficient is $C_{fp} = 16/Re$ if $Re = \rho |\dot{x}_p| d_i / \mu_\ell \leq 1180$ and $c_{fp} = 0.078 Re^{-0.25}$ if $Re > 1180$. If $\dot{x}_p = 0$ the Reynolds number is taken as $Re = 0.0000001$.

From (3.24) the plug position, $x_p^{\,t+\Delta t}$, is determined as follows

$$x_p^{\,t+\Delta t} = \dot{x}_p \Delta t + x_p \tag{3.25}$$

To take into account the interaction of the liquid plug with the liquid film the mass of the liquid film element is modified depending on how much the plug moved during a time step. Consider the plug at time t and position $x_p^{\,t}$ as shown in Figure 3.8(a). From the figure it can be seen that the second ΔL from the left hand side is partially covered by the liquid plug. The dashed lines indicate the portion of the ΔL where liquid would have been if it had not been covered by the liquid plug. The third ΔL is fully covered by the liquid plug and in effect does not contain any liquid. The first and fourth ΔL is fully exposed to the vapour bubble. As the plug moves to the new position $x_p^{\,t+\Delta t}$ as shown in Figure 3.8(b), an additional mass of liquid is deposited at the trailing end of the liquid plug. The total mass of the second ΔL film has therefore increased. At the leading edge the liquid plug has now crossed a length $x_p^{\,t+\Delta t} - x_p^{\,t}$ of the fourth element resulting in the decrease of the mass of the fourth element. The mass of the second liquid film element is modified as follows after the new position of the liquid plug is known

$$\left(m_{\ell f}^{\,t+\Delta t}\right)_{\text{mod}} = m_{\ell f}^{\,t+\Delta t} + \tfrac{1}{4}\pi\rho_\ell \left(d_i^2 - \left(d_i - 2\delta_{dep}\right)^2\right)\left(x_p^{\,t+\Delta t} - x_p\right) \tag{3.26}$$

The mass of the fourth liquid film element is modified as follows

$$\left(m_{\ell f}^{\,t+\Delta t}\right)_{\text{mod}} = m_{\ell f}^{\,t+\Delta t} - \frac{x_p^{\,t+\Delta t} - x_p^{\,t}}{\Delta L} m_{\ell f}^{\,t+\Delta t} \tag{3.27}$$

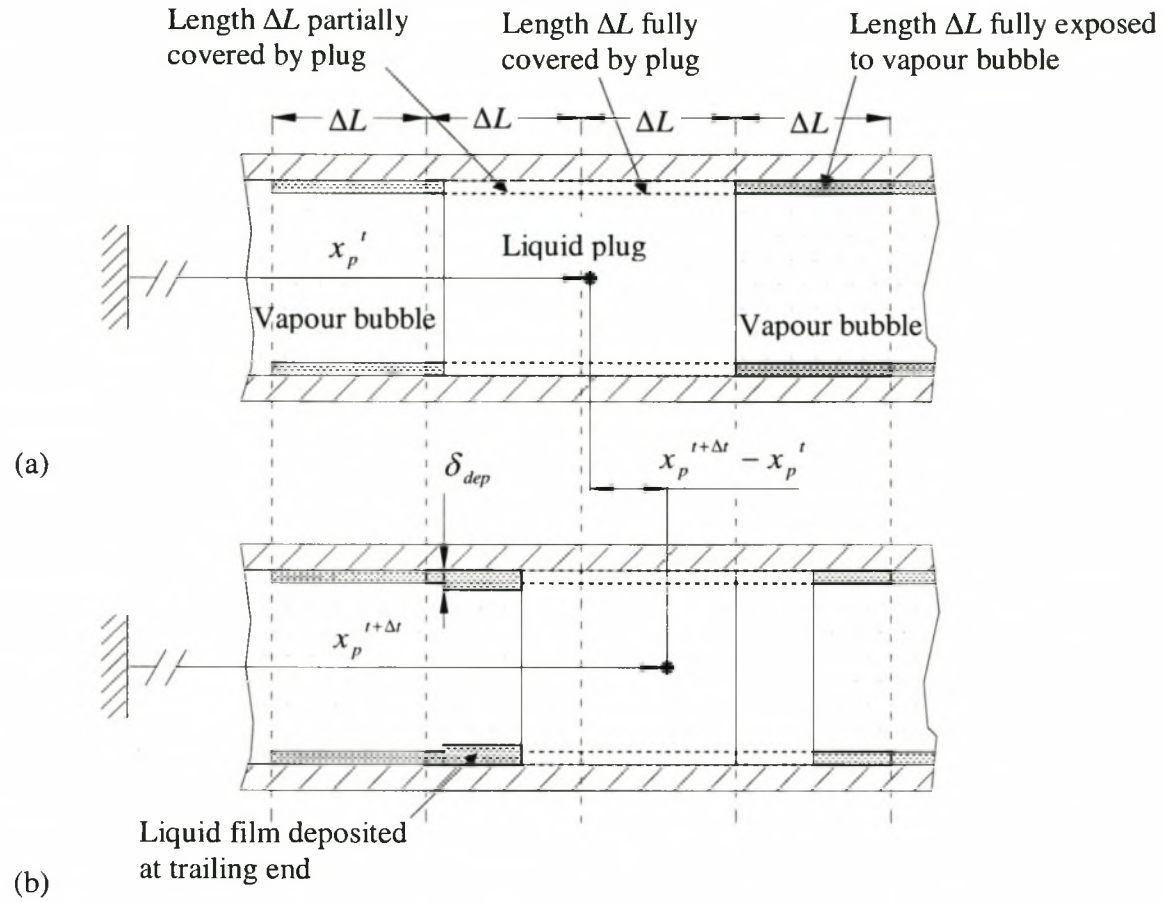

Figure 3.8 Approximation for the interaction of a liquid plug with the liquid film

The mass of a vapour bubble at the new timestep is obtained from equation (3.5) in explicit finite difference form

$$m_v^{t+\Delta t} = \left(\sum_{j=1}^{n_{\ell f}} \dot{m}''^{t+\Delta t}_{\ell f} A_{\ell f} - \sum_{l=1}^{n_{wm}} \dot{m}''^{t+\Delta t}_{wv} A_v \right) \Delta t + m_v \tag{3.28}$$

The new volume of each vapour bubble can be determined from the newly calculated plug position of the plugs j and $j+1$, at each end of a vapour bubble as follows

$$V_v^{t+\Delta t} = A_c \left(\left(x_p^{t+\Delta t} - L_p/2 \right)_{j+1} - \left(x_p^{t+\Delta t} - L_p/2 \right)_j \right) \tag{3.29}$$

With the volume known the pressure of each vapour bubble can be calculated from the ideal gas law

$$p_v^{t+\Delta t} = \frac{m_v^{t+\Delta t} R_v T_v^{t+\Delta t}}{V_v^{t+\Delta t}} \tag{3.30}$$

The process is repeated for the next time step from (3.17) to (3.30).

3.3 Results of Theoretical Model

To investigate the behaviour of the theoretical model a single plug and a multi-plug PHP were simulated.

3.3.1 Single Plug Pulsating Heat Pipe

The single plug PHP consists of a tube with a single plug as shown in Figure 3.9. The initial conditions and geometry used in the program are shown in Table 3.1. The goal of the simulation is to investigate the characteristics of the heat and mass transfer taking place inside a vapour bubble for both the kinetic mass transfer model (filename: php3ver5H2O_singleplug.pas) and the heat transfer controlled mass transfer model (filename: php1ver6H2O_singleplug.pas) and to investigate the effect of the initial plug position on the subsequent movement of the plug. Note that for the heat transfer controlled mass transfer model that the energy equation of the liquid film is ignored and that the temperature of the liquid film is taken as the wall temperature.

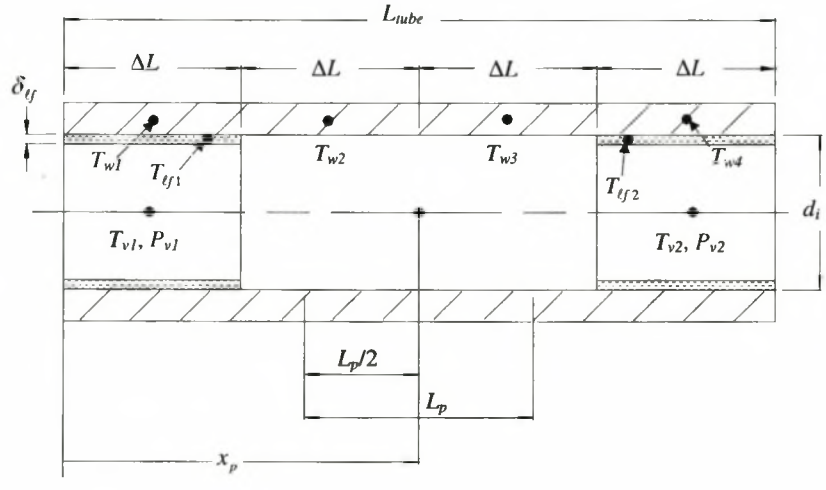

Figure 3.9 Single plug PHP model

Table 3.1 Single plug PHP geometry and initial conditions

ΔL	56.25 mm
x_{p0}	112.5 mm
L_{tube}	225 mm
L_p	112.5 mm
d_i	3.34 mm
T_{v10}, T_{v20} $T_{\ell f10}$, $T_{\ell f20}$	40 °C
P_{v10}, P_{v20}	7238 Pa
T_{w1}, T_{w4}	60 °C
T_{w2}, T_{w3}	20 °C
$\delta_{\ell f}$	0.00001 m
δ_{sep}	0.00001 m

To investigate the heat and mass transfer characteristics of a single vapour bubble the position of the liquid plug is chosen in the centre of the PHP thus enforcing symmetry so that the plug will remain stationary i.e. the rate of change of pressure in both vapour bubbles is the same so that the net force acting on the plug is zero. Figure 3.10(a) shows the change in the vapour bubble temperature and pressure as a function of time for the heat transfer controlled mass transfer model and Figure 3.10(b) shows the same for the kinetic mass transfer model. It can be seen that for the heat transfer controlled mass transfer model that the temperature increases quickly to that of the wall temperature. The pressure of the vapour bubbles also increases quickly to a steady pressure. Figure 3.10(b) shows that the vapour bubble temperature increases relatively slowly to that of the wall temperature. The vapour bubble pressure increases relatively slowly and settles at a steady pressure that is higher than that predicted by the heat transfer controlled mass transfer model. It can also be seen from Figure 3.10(b) that the temperature of the liquid film increases more slowly than that of the vapour bubble, but that it reaches the same temperature after $t \sim 3$ s.

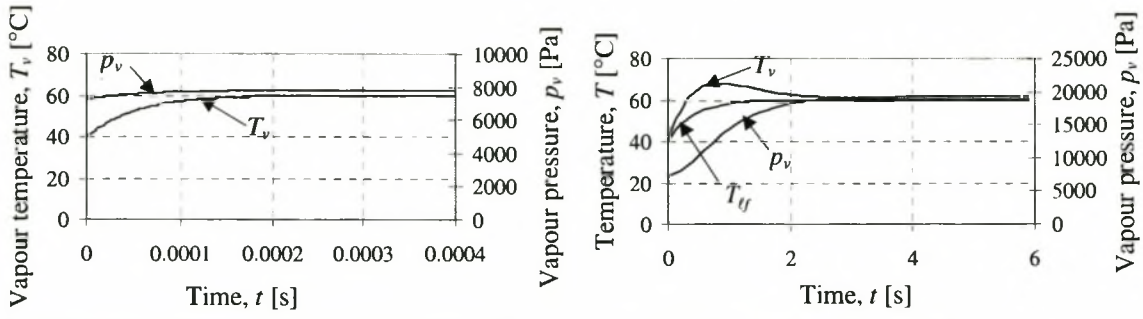

(a) Heat transfer controlled mass transfer model (b) Kinetic mass transfer model

Figure 3.10 Variation of the vapour bubble temperature, liquid film temperature and vapour bubble pressure for different mass transfer models

Looking at Figure 3.11(a) it can be seen that the mass transfer rate shoots up rapidly to a maximum and then quickly reduces to zero. Consequently the mass of the vapour only slightly increases. From Figure 3.11(b) it can be seen that the mass transfer rate steadily increases to a maximum and then slowly decreases to zero. The mass of the vapour increases to higher value than that of the heat transfer controlled mass transfer model. The vapour pressure is calculated from the ideal gas equation given by (3.30). From equation (3.30) it can be seen that for constant T_v, R and V_v the pressure is directly proportional to the mass. Since the vapour mass for the kinetic mass transfer model is higher than for the heat transfer controlled mass transfer model the pressure will also be higher.

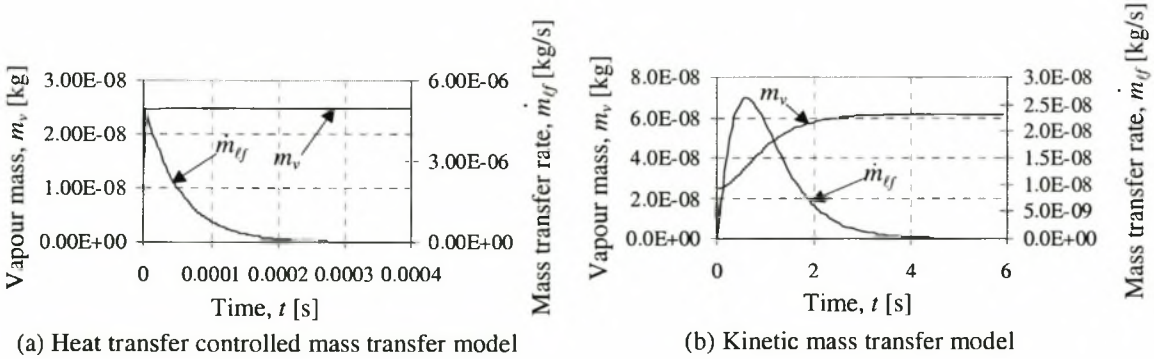

(a) Heat transfer controlled mass transfer model (b) Kinetic mass transfer model

Figure 3.11 The variation of vapour bubble mass and mass transfer rate for different mass transfer models

The movement of the plug for different initial plug positions is shown in Figure 3.12. From Figure 3.12(a) it can be seen that the movement of the plug for the heat transfer controlled mass transfer model is quite different for different initial positions. For the kinetic mass transfer model the movement of the plug is less dramatic and attains a steady position x_p = 0.1125 m for all the initial positions as shown in Figure 3.12(b). It can be seen in Figure

3.12(a) for $0 < t < 2$ s as the plug moves that small oscillations are superimposed on the general direction of movement. The increase in vapour mass in a very short time causes a higher pressure pulse (and consequently force) to be exerted onto the liquid plug for the heat transfer mass transfer controlled model. These pressure pulses might offer an explanation for the small oscillations.

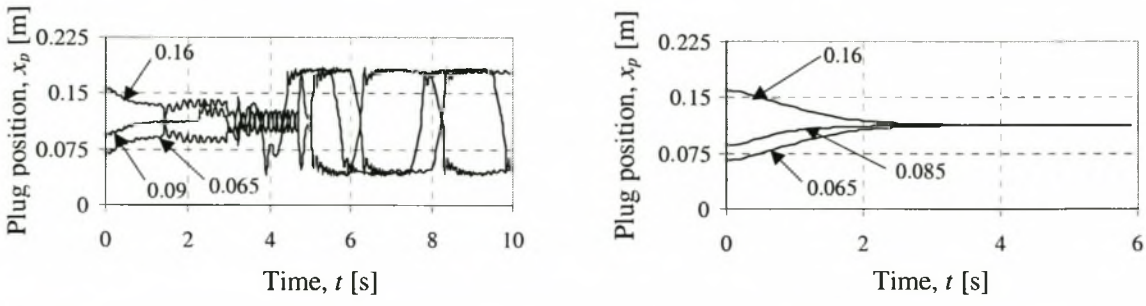

(a) Heat transfer controlled mass transfer model

(b) Kinetic mass transfer model

Figure 3.12 The variation of the plug position for different initial positions and different mass transfer models

Besides the small oscillations described above it can be seen at $t \sim 1.5$ s (for $x_{p0} = 0.16$ m) that the plug suddenly shoots from $x_p \sim 0.13$ to $x_p \sim 0.09$ m and at $t \sim 3.2$ s the plug suddenly shoots in the opposite direction from $x_p \sim 0.09$ m to 0.14 m. This type of movement is even more pronounced at $t \sim 6$ s where the plug shoots from $x_p \sim 0.06$ to $x_p \sim 0.176$ m and then back in the opposite direction at $t \sim 7.5$ s from $x_p \sim 0.175$ to $x_p \sim 0.06$ m. Figure 3.13 shows the variation of the liquid plug position (for $x_{p0} = 0.16$ m) and the mass of the liquid film on either side of the plug. It can be seen from Figure 3.13 that as a liquid film dries up ($m_{lf} = 0$ kg) that the plug shoots into the direction of the dried up film. When the mass of the liquid film becomes zero evaporation cannot take place and as a consequence the pressure of the vapour bubble adjacent to the dried up liquid film does not increase at the same rate as the other vapour bubble where evaporation may still be taking place. This brings about a great imbalance in the vapour bubble pressures causing the rapid movement of the plug.

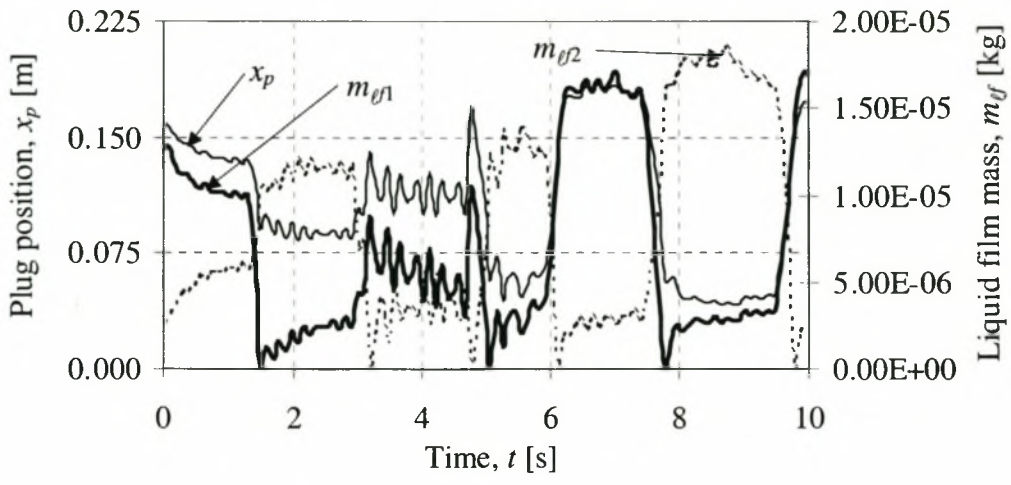

Figure 3.13 The variation of the liquid plug position and liquid film mass

The different forces exerted onto the liquid plug are shown in Figure 3.14. From Figure 3.14 it can be seen that the force due to the difference in vapour bubble pressure F_p is the most dominant followed by the frictional force F_f and then the capillary force F_c. From Figure 3.14 it can be concluded that the capillary force is negligible in comparison to the other force components.

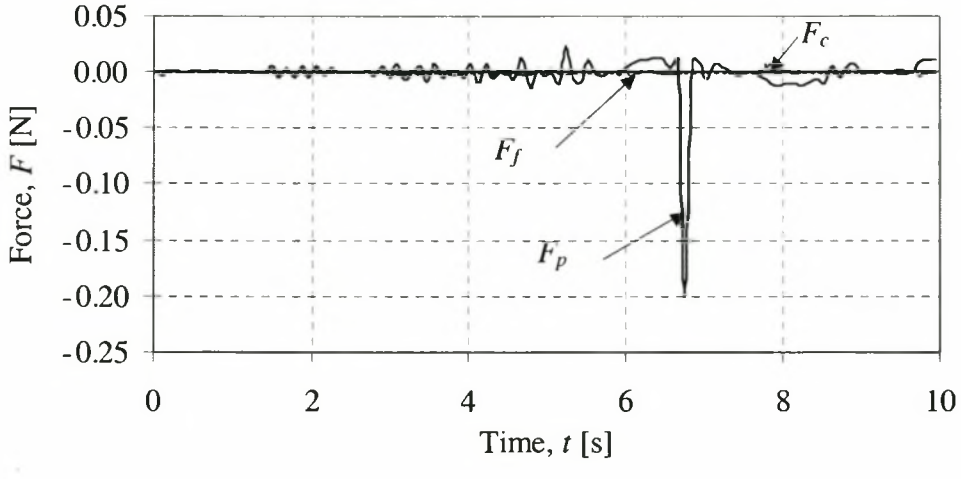

Figure 3.14 The contribution of the different forces exerted onto the liquid plug

The kinetic mass transfer model is more difficult to understand and interpret than the heat transfer mass transfer controlled model. To understand the heat and mass transfer characteristics of a vapour bubble better when using the kinetic mass transfer model the effect of h_{lfw} and $\hat{\sigma}$ on the T_{lf}, T_v, P_v, m_v and $\dot{m}_{lf}$ were investigated.

Figure 3.15 shows the effect of h_{lfw} on $T_{\ell f}$, T_v, P_v, m_v and $\dot{m}_{\ell f}$. It can be seen that as h_{lfw} increases that the amount by which T_v "overshoots" the wall temperature becomes more significant but that T_v reaches a steady state condition more quickly. It can also be seen that $T_{\ell f}$ and p_v attain a steady state condition more quickly as h_{lfw} increases. It can also be seen that as h_{lfw} increases that the time it takes for $\dot{m}_{\ell f}$ to reach a maximum and decrease to zero becomes shorter and that the maximum value for $\dot{m}_{\ell f}$ increases. The effect of increasing h_{lfw} does not have a significant influence on the final p_v and m_v.

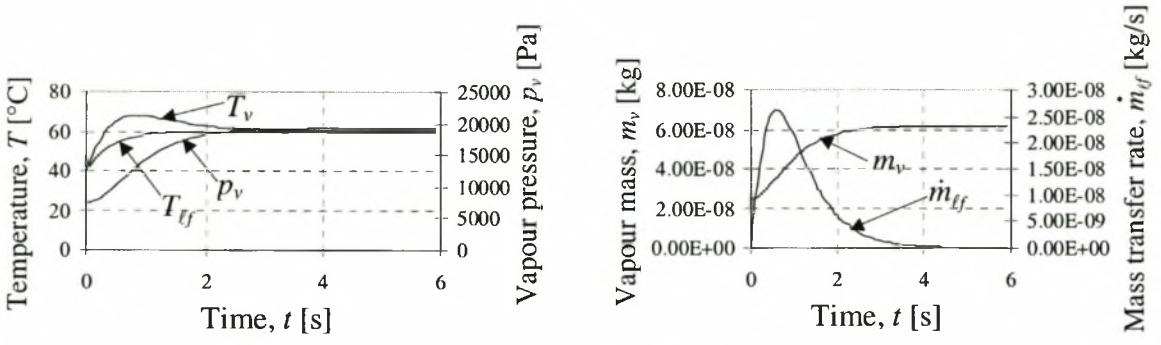

(a) h_{lfw} = 1000 W/m^{2}K

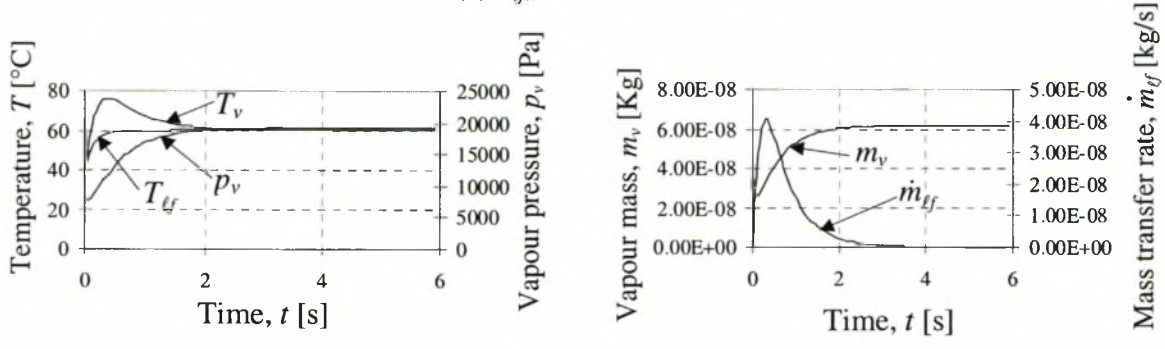

(b) h_{lfw} = 2000 W/m^{2}K

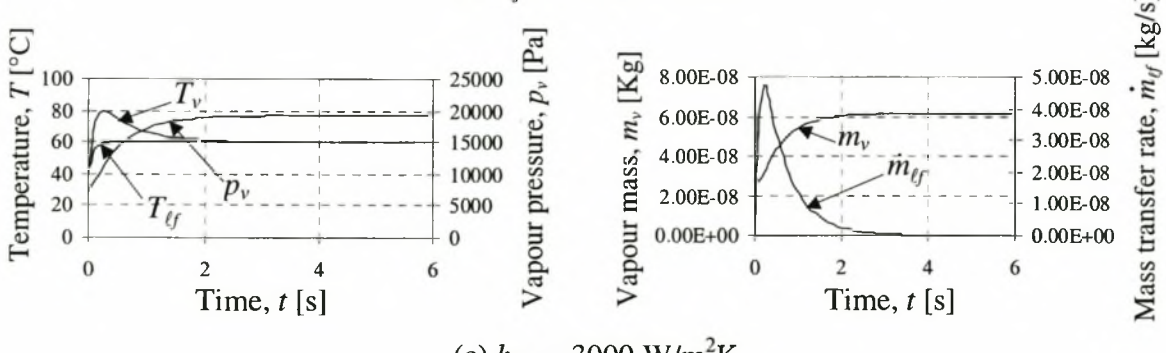

(c) h_{lfw} = 3000 W/m^{2}K

Figure 3.15 The variation of the vapour temperature, vapour pressure, film temperature, vapour mass and mass transfer rate for different values of h_{lfw}

Figure 3.16 shows the plug movement for an initial position of x_{p0} = 0.065 m. It can be seen that as h_{lfw} increases that the liquid plug attains a steady state value of x_p = 0.1125 m more quickly, although the difference in time for the plug to attain this position for h_{lfw} = 2000 and 3000 W/m^{2}K is less pronounced than for h_{lfw} = 1000 W/m^{2}K.

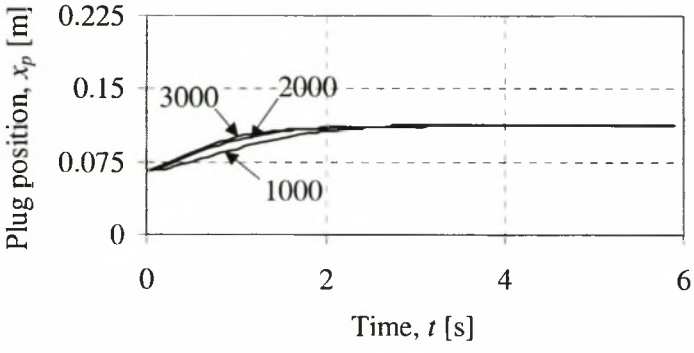

Figure 3.16 The variation of the plug position for different values of h_{lfw}

Figure 3.17 shows the effect of $\hat{\sigma}$ on $T_{\ell f}$, T_v, P_v, m_v and $\dot{m}_{\ell f}$. As as the case for h_{lfw} it can be seen that as $\hat{\sigma}$ increases that the amount by which T_v "overshoots" the wall temperature becomes more significant but that T_v reaches a steady state condition more quickly. It can also be seen that $T_{\ell f}$ and p_v attain a steady state condition more quickly as $\hat{\sigma}$ increases. It can also be seen that as $\hat{\sigma}$ increases that the time it takes for $\dot{m}_{\ell f}$ to reach a maximum and decrease to zero becomes shorter and that the maximum value for $\dot{m}_{\ell f}$ increases. The effect of increasing $\hat{\sigma}$ does not have a significant influence on the final p_v and m_v.

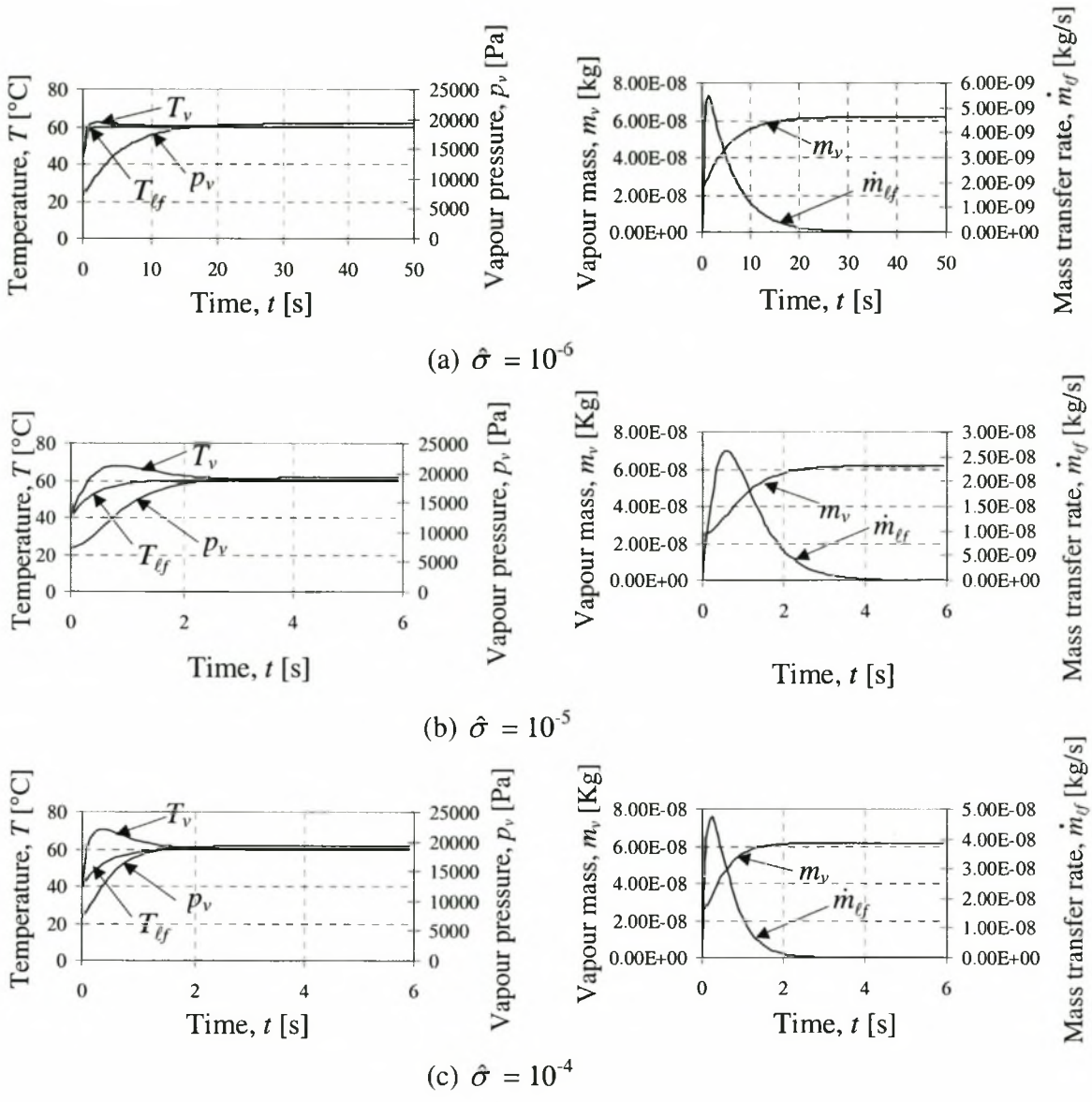

Figure 3.17 The variation of the vapour temperature, vapour pressure, film temperature, vapour mass and mass transfer rate for different values of $\hat{\sigma}$

Figure 3.18 shows the plug movement for an initial position of $x_{p0} = 0.065$ m. It can be seen that as $\hat{\sigma}$ increases that the liquid plug attains a steady state value of $x_p = 0.1125$ m more quickly, although the difference in time for the plug to attain this position is less pronounced for $\hat{\sigma} = 10^{-4}$ and 10^{-5} than for $\hat{\sigma} = 10^{-6}$.

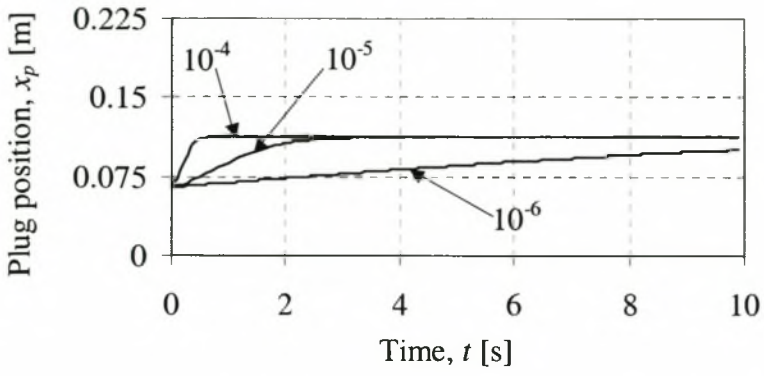

Figure 3.18 The variation of the plug position for different values of $\hat{\sigma}$

3.3.2 Multi-plug Pulsating Heat Pipe

The PHP shown in Figure 3.19 was simulated using the theoretical model in which the evaporation and condensation processes were simulated using the heat transfer controlled mass transfer model. Table 3.2 gives values for the initial conditions and geometry used in the program.

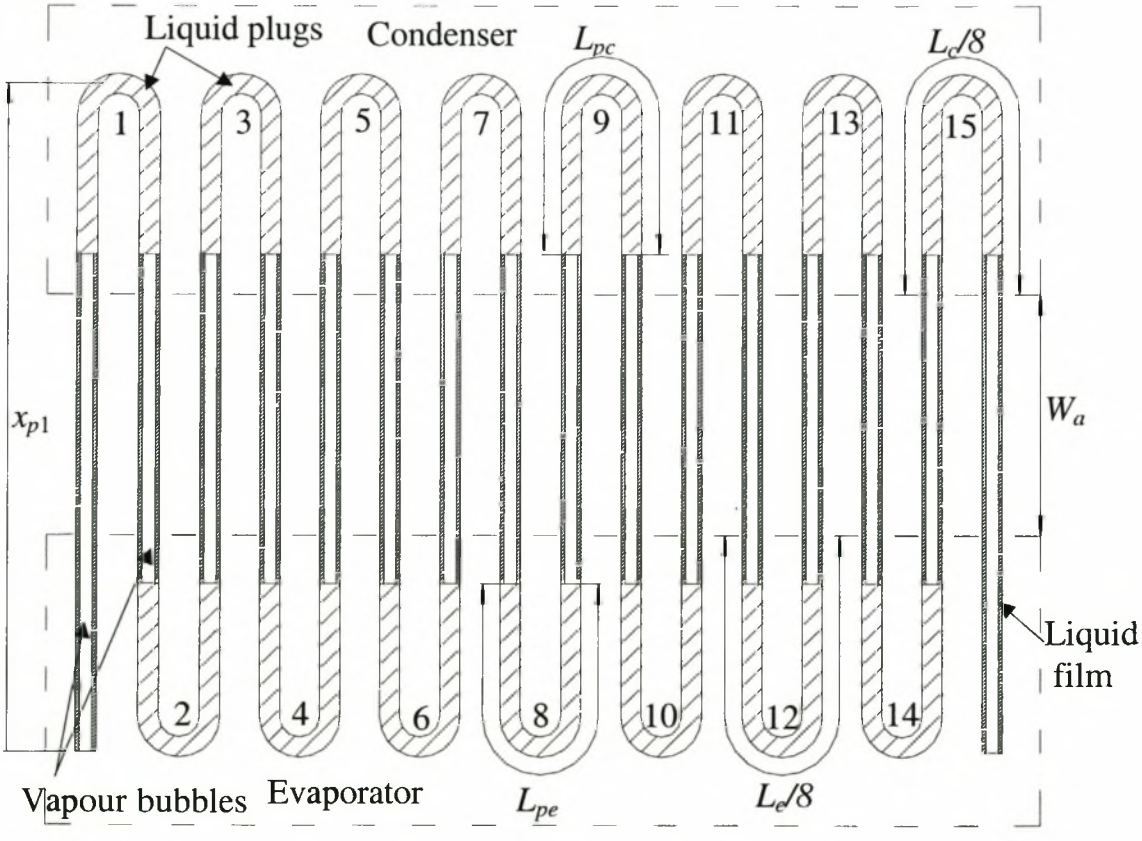

Figure 3.19 Muliti-plug PHP simulated by theoretical model

Table 3.2 Multi-plug initial conditions and geometry

$(x_{p0})_i$ (where i is the plug number)	270 x i mm
T_{v0}	40 °C
p_{v0}	7238
L_{pe}	140 mm
L_{pc}	150 mm
$L_c/8$	190 mm
$L_e/8$	190 mm
W_a	80 mm
L_{tube}	4 320 mm
d_i	3.34 mm
T_{we}	60 °C
T_{wc}	40 °C
$\delta_{\ell f}$	0.00001 m
$h_{\ell fw}$ (evaporator and condenser)	1000 W/m^{2}K
h_{wv} (evaporator and condenser)	10 W/m^{2}K
$h_{\ell fv}$ (evaporator and condenser)	10 W/m^{2}K
$h_{\ell fw}$, h_{wv}, $h_{\ell fv}$ (adiabatic region)	0 W/m^{2}K

The typical movement of the liquid plugs predicted by the theoretical model for water (filename: php1ver6H2O_multiplug.pas) is shown in Figure 3.20. Figure 3.21 shows the velocity of the liquid plugs as a function of time as predicted by the theoretical model. It can be seen in Figure 3.21 that the liquid plugs oscillate with a relatively small amplitude until before $t \sim 4$ s where the amplitude of the oscillations increases. Just after $t \sim 5$ s the amplitude decreases until $t \sim 12$ s where it increases again. The same sudden increase and subsequent decrease in amplitude is also observed at $t \sim 19$ and 26 s. This behaviour is reminiscent of the pulsating movement of the liquid plugs observed experimentally. From Figure 3.21 it can be seen that the maximum plug speed is $v_p \approx 0.75$ m/s which justifies the assumption made in section 3.1.7 regarding the estimation of the capillary force that $v_p < 10$ m/s.

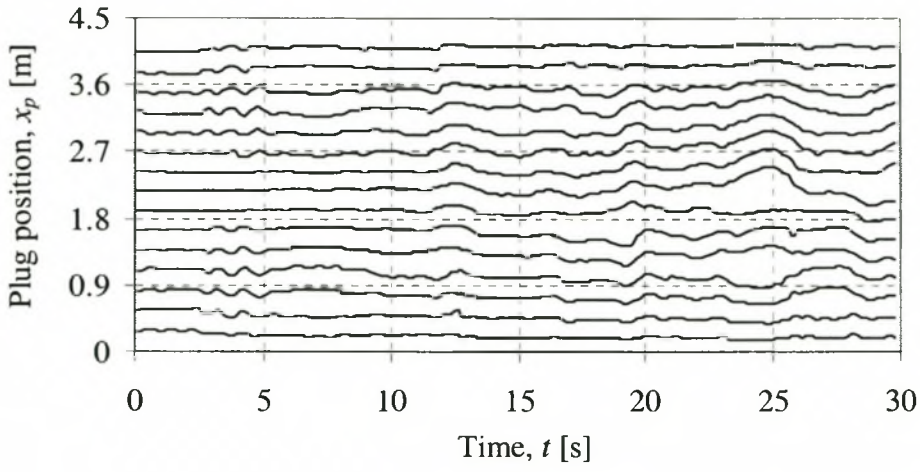

Figure 3.20 Typical movement of the liquid plugs as predicted by the theoretical model for water

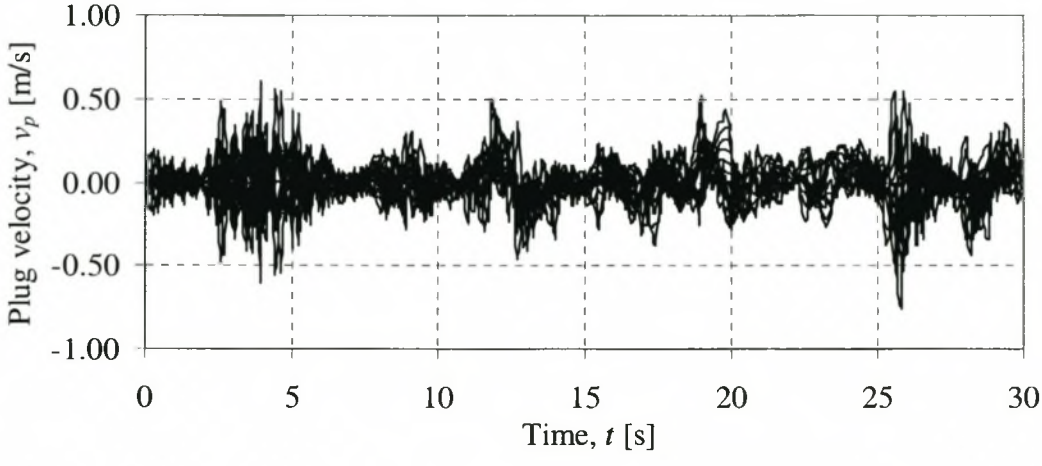

Figure 3.21 The velocity of the plugs predicted by the theoretical model for water

The PHP in Figure 3.19 was simulated using ammonia as the working fluid (filename: php1ver6NH3_multiplug.pas). The same initial conditions and geometry were used as given in Table 3.2. The typical movement of the liquid plugs predicted by the theoretical model is shown in Figure 3.22. Comparing Figure 3.22 with Figure 3.20 it can be seen that the movement of the liquid plugs for ammonia appears less dramatic than that of water. The displacement of the liquid plugs for ammonia is lower than that for water. However, looking at Figure 3.23 it can be seen that the velocity of the plugs for ammonia is higher than that of the water in Figure 3.21. From Figure 3.23 it is more difficult to identify pulsating movement than for water. From Figure 3.23 it can be seen that the maximum plug speed is v_p

≈ 1 m/s which again justifies the assumption made in section 3.1.7 regarding the estimation of the capillary force that $v_p < 10$ m/s.

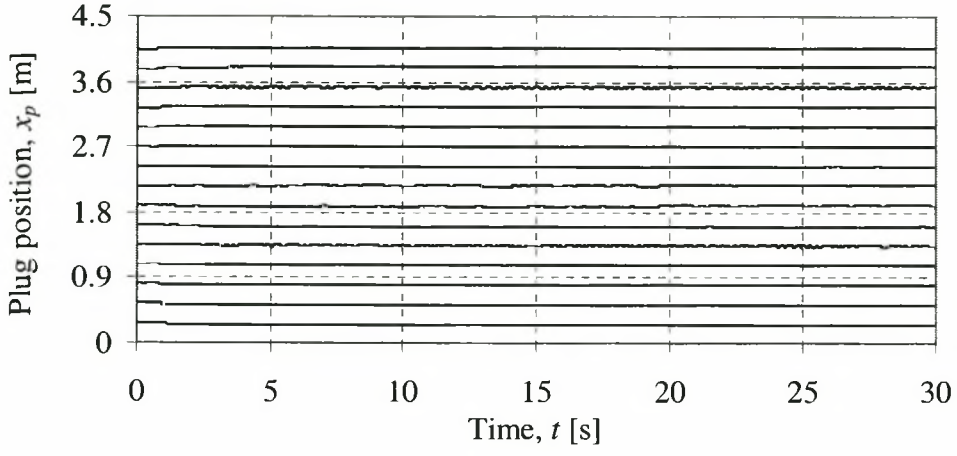

Figure 3.22 Typical movement of the liquid plugs as predicted by the theoretical model for ammonia

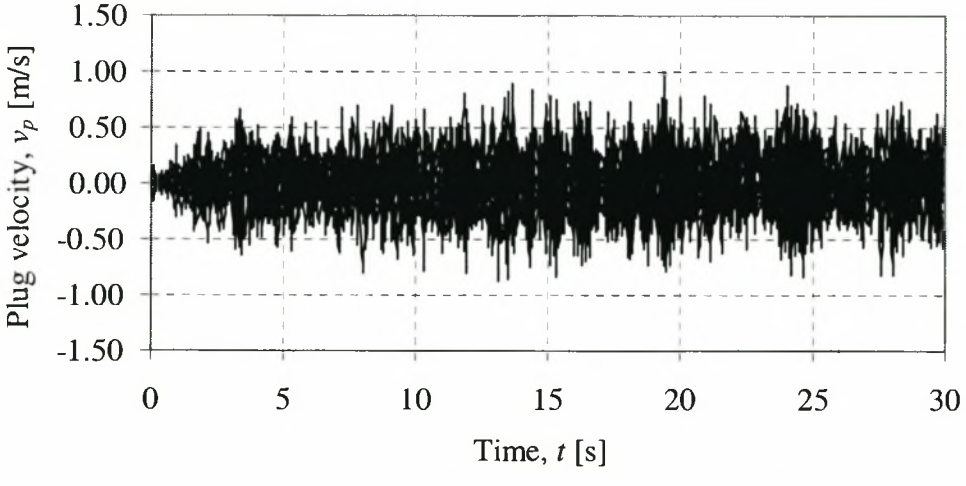

Figure 3.23 The velocity of the plugs as predicted by the theoretical model for ammonia

Figure 3.24 shows the variation of the heat transfer rate as predicted by the theoretical model using water and ammonia. It can be seen that the predicted heat transfer rate is significantly higher for ammonia than for water. It can also be seen that the inclination angle does not have a significant effect on the heat transfer rate for ammonia.

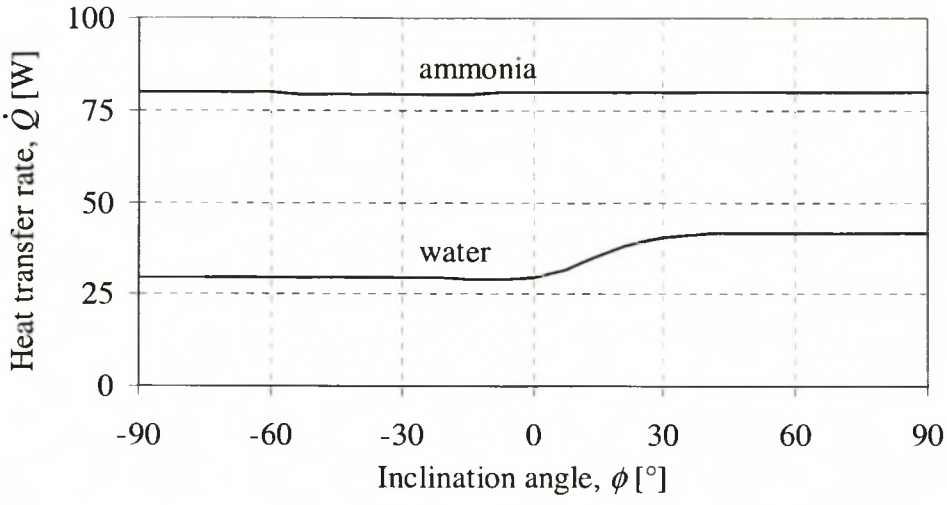

Figure 3.24 Variation of the heat transfer rate with inclination angle for different working fluids as predicted by the theoretical model

Figure 3.25 shows the variation of the heat transfer rate with the inclination angle for different filling ratios using water as the working fluid. To obtain different filling ratios the length of the liquid plugs is varied. Table 3.3 shows the different plug lengths used to obtain the different fill ratios. From Figure 3.25 it can be seen that the theoretical model predicts that the heat transferred by the PHP is less in the top heat mode than in the bottom heat mode which is consistent with experimental observations and that the heat transfer rate increases as the filling ratio decreases.

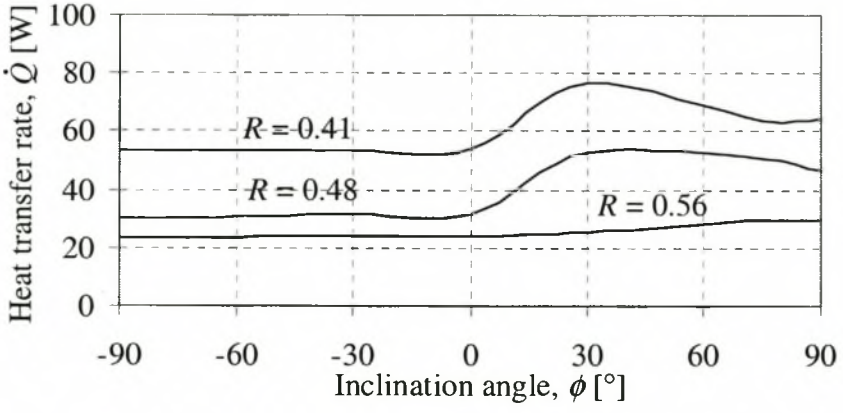

Figure 3.25 Variation of the heat transfer rate with inclination angle for different filling ratio as predicted by the theoretical model for water (n_{chan} = 16)

Table 3.3 Length of plugs for different fill ratios

R	L_{pe} [mm]	L_{pc} [mm]
0.41	110	124
0.48	130	147
0.56	151	170

Figure 3.26 shows the variation of the heat transfer with the inclination angle for different number of turns for water. To simulate PHPs with different number of channels, channels are merely added or taken away from the model as shown in Figure 3.19 and L_{tube} is adjusted as necessary compensate for the channels added or taken away. For every channels a liquid plug is also added. From Figure 3.26 it is unclear what the effect of the number of turns is on the heat transfer rate.

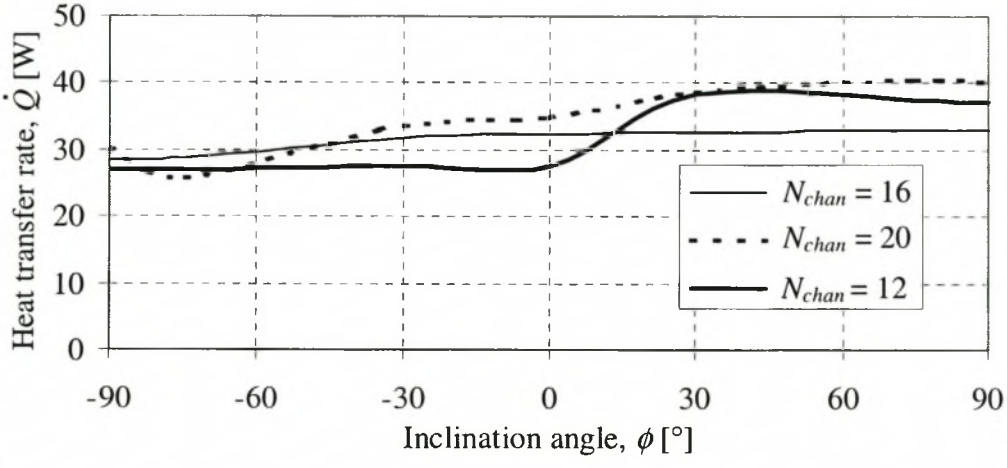

Figure 3.26 Variation of the heat transfer rate with the inclination angle for different number of turns for water (R = 0.51)

4 EXPERIMENTAL STUDY OF THE LIQUID FILM BEHAVIOUR

An experiment was set up to study the movement of a liquid plug inside a vertically orientated glass capillary tube under gravity. The aim of the experiment was to determine the thickness of the liquid film deposited on the wall at the trailing end of a liquid plug (as it moves through a capillary tube).

4.1 Experimental Set-up and Procedure

The experimental set-up consists of a capillary tube supported by a stand in a vertical position as shown in Figure 4.1. At the top end the capillary tube is connected to a syringe using a plastic tube. A video camera (JVC GV-DS1 and serial no. 082220222) is positioned as shown and is used to capture the movement of the liquid. A desk lamp is positioned behind a sheet of paper to attain the required lighting.

Before clamping the capillary tube to the stand the dry mass of the tube is measured (using a Precisa 40SM-200A, serial no. 73464 and store no. 248173 scale). The liquid to be tested is heated to the desired temperature and then positioned in a container at the bottom end of the capillary tube so that the end portion of the capillary tube is submerged in the liquid. The syringe is then used to suck the liquid into the capillary tube until the desired level of the liquid is obtained. The container with the liquid is then removed. The plastic tubing is quickly disconnected from the capillary tube and the liquid plug starts to move down the capillary tube due to gravity. This movement of the liquid plug is captured by the video camera.

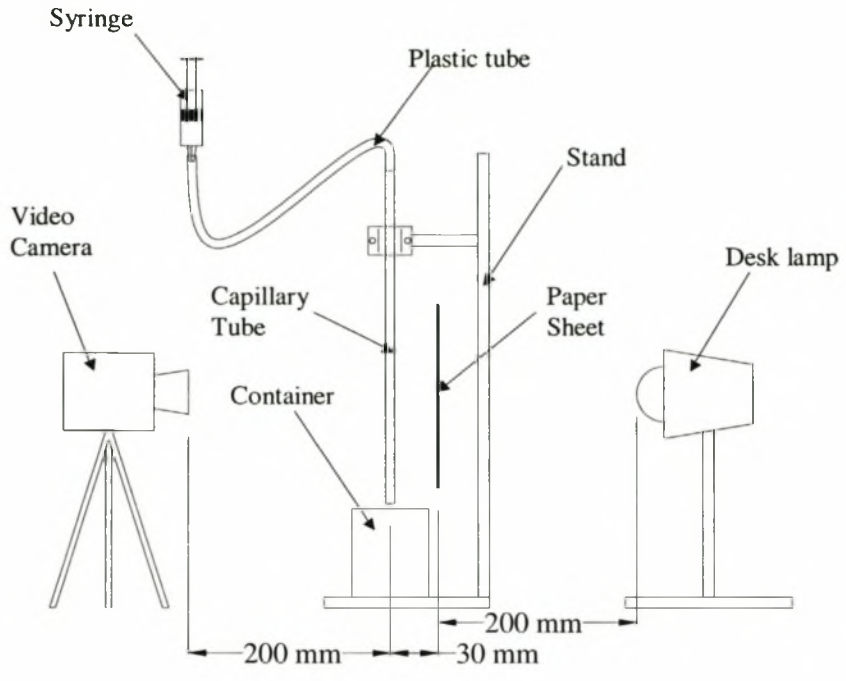

Figure 4.1 Experimental set-up to study liquid film behaviour in a capillary tube

4.2 Experimental Observations

The initial stationary position of the liquid plug of length L_{pi} is shown in Figure 4.2(a). After the plastic tube is disconnected the liquid plug starts to move and a liquid film is deposited at by trailing-end as shown in Figure 4.2(b). A portion of the liquid plug of a length L_{pmin} will remain in the tube depending on the magnitude of the momentum of the liquid plug, the friction and surface tension as shown in Figure 4.2(c). This length is determined by making a video "clip" of the movement and then to freeze the frame where the L_{pmin} can be measured. As the liquid film flows down the tube its thickness grows and several liquid plugs are formed along the tube. Droplets are also formed against the inside wall when film break up occurs. Some of the liquid film flows into the portion of the liquid plug at the exit as shown in Figure 4.2(c). The flow of the liquid film into the liquid plug will cause it to grow as shown in Figure 4.2(d). Only a certain mass of liquid can be supported by the capillary forces against gravity, and liquid leaves the tube in the form of droplets as shown in Figure 4.2(e) which are caught using a paper towel and weighed. After a while (± 1 second) equilibrium is achieved as shown in Figure 4.2(f).

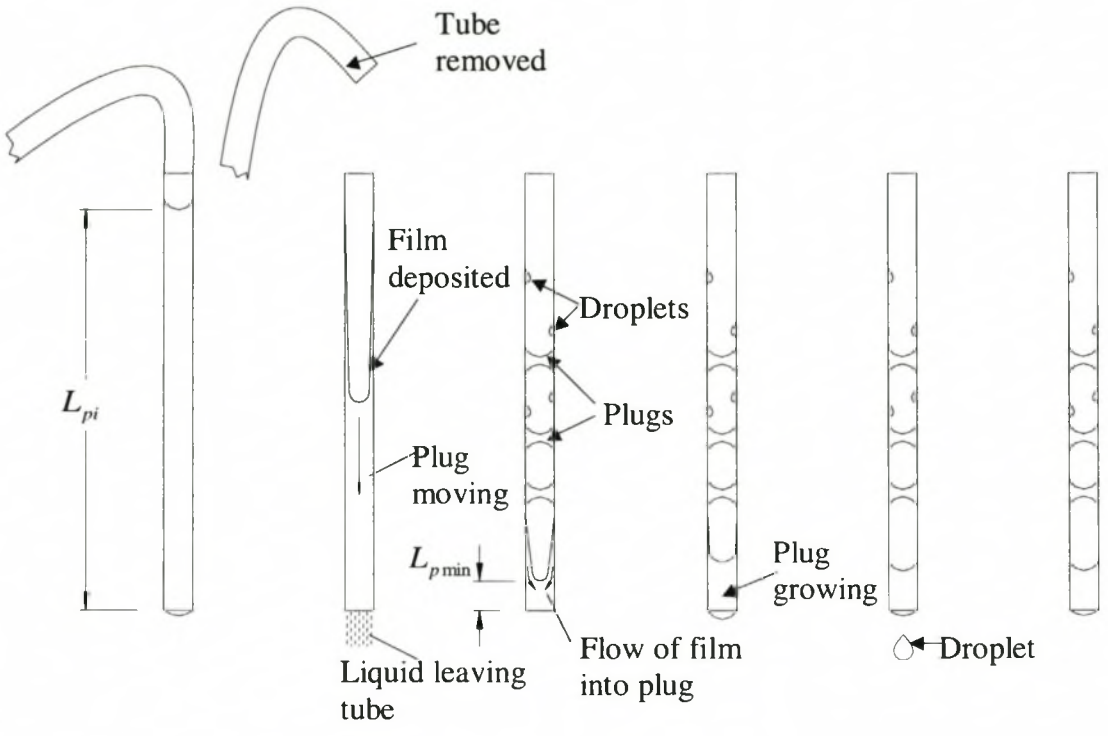

Figure 4.2 Experimental observations as a liquid plug moves in a capillary tube

The average thickness of the liquid film $\delta_{\ell f}$ is correlated with the inside diameter d_i of the tube, the surface tension σ and viscosity μ of the liquid water and the average velocity v_p of the exiting liquid plug with an equation of the form

$$\delta_{\ell f} = a_0 d_i^{a_1} \sigma^{a_2} v_p^{a_3} \mu^{a_4} \tag{4.1}$$

The average film thickness $\delta_{\ell f}$ in equation (4.1) is defined by the following equation

$$m_{\ell f} = \tfrac{1}{4}\pi\left(d_i^2 - \left(d_i - 2\delta_{\ell f}\right)^2\right)\left(L_{pi} - L_{p\min}\right)\rho_\ell \tag{4.2}$$

The mass of the liquid film deposited $m_{\ell f}$ is determined by subtracting the dry mass of the tube m_{td} and the mass of the liquid plug left in the tube due to surface tension $\pi d_i^2 \rho L_{pmin}/4$ from the mass of the tube partially filled with liquid $m_{t\ell}$ and adding the mass of the liquid drops m_{drops}

$$m_{\ell f} = m_{t\ell} - m_{td} - \tfrac{1}{4}\pi d_i^2 \rho_\ell L_{p\min} + m_{drops} \tag{4.3}$$

The average velocity of the liquid plug leaving the tube is calculated as follows

$$v_p = \frac{L_{pi} - L_{p\min}}{\Delta t} \tag{4.4}$$

4.3 Results

The natural logarithm are taken on both sides of equation (4.1) to give

$$\ln \delta_{tf} = \ln a_0 + a_1 \ln d_i + a_2 \ln \sigma + a_3 \ln v_p + a_4 \ln \mu \tag{4.5}$$

The coefficients are then determined using a standard multi-linear regression technique to give

$$\delta_{tf} = 6.031 \times 10^{-3} d_i^{0.485} \sigma^{1.931} v_p^{0.094} \mu^{-0.130} \tag{4.6}$$

This correlation is based on tube diameters of d_i = 1.5 to 2.86 mm, water as working fluid, surface tension of σ = 0.0671 to 0.078 N/m, average velocities of v_p = 0.33 to 1.8 m/s and viscosity of μ = 0.00049 to 0.00176 Pas. The film thickness as predicted by equation (4.6) is compared to the experimental values in Figure 4.3.

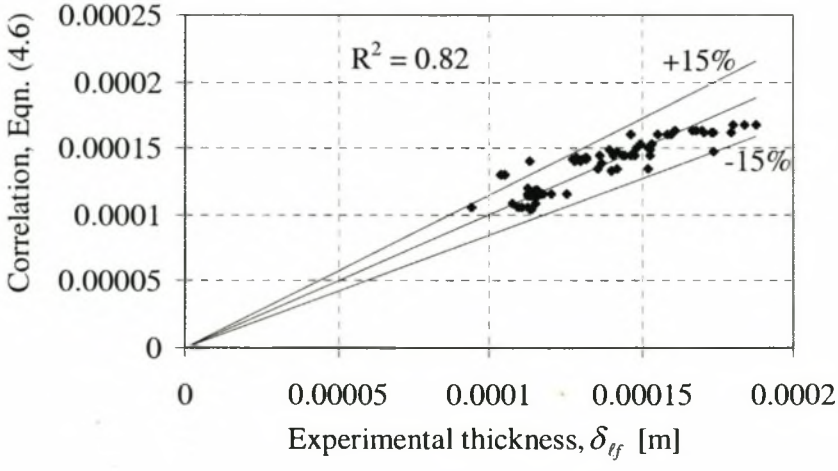

Figure 4.3 Film thickness as predicted by equation (4.6) compared to the experimental values

From the results in Figure 4.3 it can be seen that under the different testing conditions the average film thickness varies between 100 and 200 μm.

5 EXPERIMENTAL VERIFICATION OF THEORETICAL MODEL

Several experiments were devised to verify the theoretical model. The experiments include i) a single plug moving in a vertical glass U-tube, ii) a single plug moving in a horizontal tube, iii) a PHP made from glass tubes and pentane as the working fluid, iv) a stainless steel closed end PHP with water as the working fluid, v) an aluminium closed loop PHP with water as working fluid and, vi) a stainless steel closed end PHP with ammonia as the working fluid. The glass tube experiments assisted in understanding the working fluid behaviour by being able to visually observe the fluid movement.

5.1 Single Plug Vertical Glass U-tube

The single plug vertical glass U-tube experiment was done to study the movement of a single plug in a capillary tube due to heat transfer and gravity.

5.1.1 Experimental Set-up and Procedure

The experimental apparatus consists of a liquid plug inside a vertically orientated U-shaped glass capillary tube (2mm ID) with two containers filled with cold and hot water to serve as the condenser and evaporator sections as shown in Figure 5.1. Pentane is used as the working fluid. A video camera (JVC model GV-DS1 and serial no. 08220222) and desk lamp are positioned as shown to record the movement of the liquid plug.

Cold water is water poured into the bottom container first and then hot water is poured into the top container. Heat transfer takes place and the liquid plug starts to move. The position of the liquid plug is determined as a function of time from the video recording by tracking the displacement of the liquid plug between every frame.

Cooling one of the legs results in different vapour pressures in the two legs of the U-tube. Due to the difference in pressure the plug will move to a different position. By using this technique the initial position of the liquid plug can be controlled.

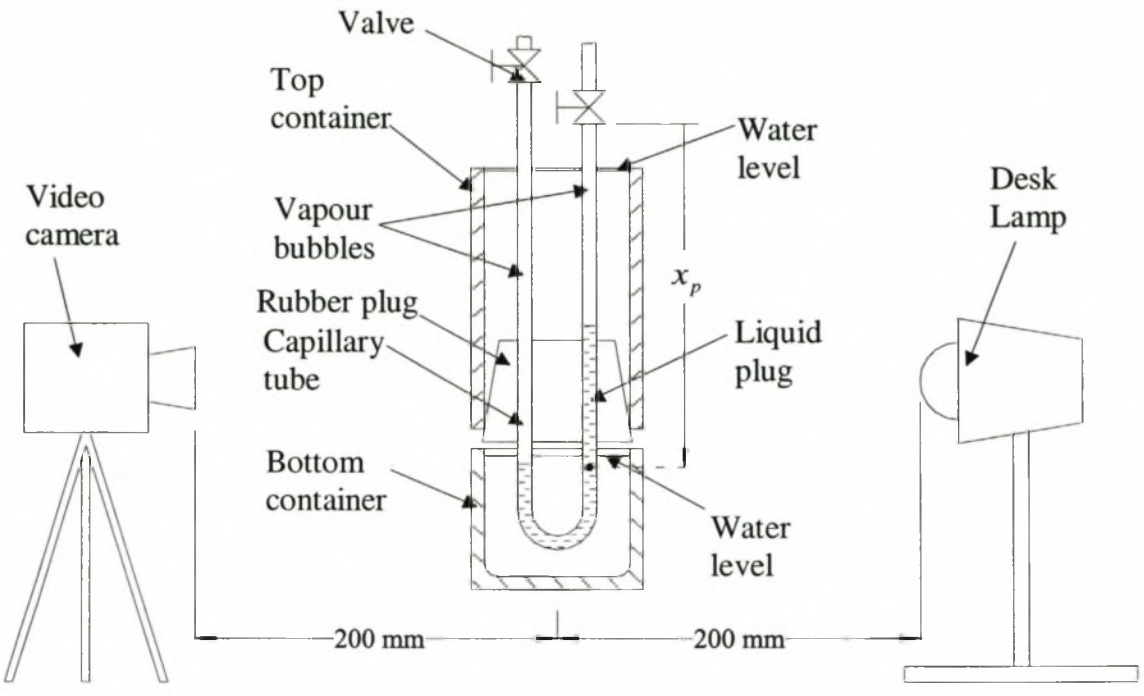

Figure 5.1 Study of movement of a liquid plug in a U-shape capillary tube

5.1.2 Experimental Observations and Results

It was found that the movement of the liquid plug is quite different for initial conditions that are apparently the same. Sometimes the liquid plug did not move while at other instances the liquid plug moved in a random oscillatory manner. However, after a while the liquid plug always stopped moving. It was also observed that a thin liquid film was deposited at the trailing edge of the liquid plug and the evaporation of the liquid film could also be noticed with the naked eye. No bubbles were seen in the liquid film while evaporation took place and it is therefore reasonable to believe that for this particular experimental set-up and testing conditions that nucleate boiling is not the mechanism whereby evaporation of the liquid film takes place.

5.1.3 Comparison of Experimental Results with Theoretical Results

The movement of the liquid plug was simulated using the theoretical model. The evaporation and condensation processes taking place were simulated using the kinetic mass transfer model. Figure 5.2 shows important dimensions of the experimental set-up as were used in the theoretical simulation (filename: php3ver2PentaanEksperiment2.pas). Table 5.1 gives numerical values for the initial conditions and geometry used in the program. Figure 5.3 shows the liquid plug position as a function of time as was experimentally determined

compared to the plug position as predicted by the theoretical model. From the figure it can be seen that the theoretical model does not predict the exact movement of the liquid plug, but it does predict the final stationary position of the liquid plug within (0.279 - 0.2598)/0.2598 x 100 = 7.39%.

From Figure 5.3 it can be seen that the theoretical model predicts that the liquid plug will reach a maximum position, and become stationary at this position, after t = 0.25 s whereas for the experimental case the time it took to reach a maximum and become stationary was t = 1.8 s.

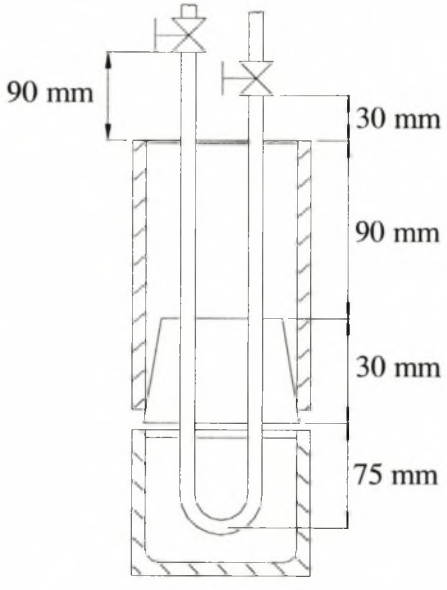

Figure 5.2 Important dimensions of experimental set-up

Table 5.1 Initial values and geometry used in theoretical model to predict plug movement in vertical U-shape tube

x_{p0}	192 mm
T_{v0}	20 °C
$T_{\ell f 0}$	20 °C
p_{v0}	55816 Pa
L_p	282 mm
L_{tube}	510 mm
d_i	3.34 mm
T_w for $30 < x \leq 120$ and $330 < x \leq 420$ mm	40 °C
T_w for all remaining x	0 °C
$\delta_{\ell f}$ for $30 < x \leq 40$	0.0001 m
δ_{dep}	0.0001 m
$h_{\ell fw}$ for $30 < x \leq 120$, $150 < x \leq$	1000 W/m^{2}K
h_{wv} for $30 < x \leq 120$, $150 < x \leq$	10 W/m^{2}K
$h_{\ell fv}$ for $30 < x \leq 120$, $150 < x \leq$	10 W/m^{2}K
$h_{\ell fw}$, h_{wv}, $h_{\ell fv}$ for all remaining x	0 W/m^{2}K

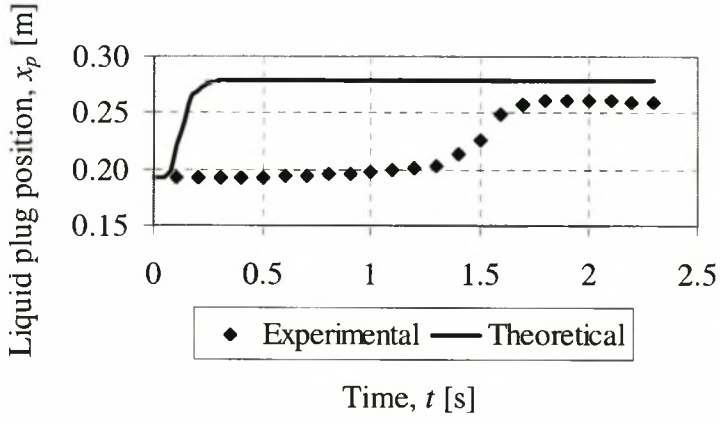

Figure 5.3 Comparison of experimental and theoretical predicted plug position

5.2 Single Plug Horizontal Glass tube

The single plug horizontal glass tube experiment was done to study the movement of a single plug in a capillary tube due to heat transfer.

5.2.1 Experimental Set-up

The experimental apparatus consist of a liquid plug inside a glass capillary tube (2 mm ID) positioned in three containers as shown in Figure 5.4. The middle container is first filled with ice water which functioned as the condenser and the outer two containers are then filled with warm water and functioned as evaporators. Pentane was used as the working fluid. For the filling procedure refer to APPENDIX E.

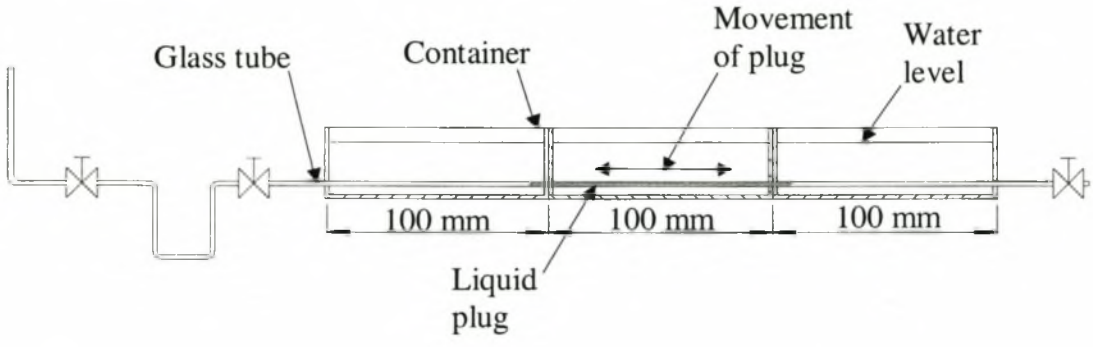

Figure 5.4 Study of the liquid plug movement in a horizontal capillary tube

5.2.2 Observations

When pouring the warm water into the outer containers the liquid plug starts to move. The movement of the plug is quite unpredictable and it is very difficult to repeat a particular movement of the plug. The movement of the plug varied from irregular oscillations with amplitudes of ~ 50 mm which stopped after ~ 2 s to more steady oscillations with amplitudes of ~ 1 mm which stopped after ~ 10 s. In some cases the liquid plug did not oscillate at all and moved relatively slowly from its initial position to a stationary position. During the movement a liquid film deposited at the trailing end of the liquid plug was observed. The evaporation of this film could actually be seen with the naked eye.

5.3 Glass Tube Pulsating Heat Pipe

A PHP was constructed from glass tubing to visually observe the operating mechanisms taking place inside the PHP.

5.3.1 Experimental Set-up

The experimental set-up consist of a capillary glass tube bent into the shape shown in Figure 5.5 to form a closed loop PHP. The PHP is filled with pentane as the working fluid (refer to APPENDIX F for filling procedure). Two containers are filled with water, cold water in the

one container that functioned as the condenser and warm water in the other which functioned as the evaporator. The PHP is then inserted into the containers as shown in Figure 5.6. The PHP starts to operate and it is possible to observe the movement of the liquid plugs.

Figure 5.5 Glass pulsating heat pipe

Figure 5.6 Glass pulsating heat pipe inserted into containers with water

5.3.2 Observations

When the PHP is inserted into the containers the liquid plugs move vigorously in what appears to be an irregular oscillatory manner. After ~ 10 s the movement of the plugs reduces drastically to a near standstill and move slowly back and forth. After a period of ~

120 s the liquid plugs generally start to move vigorously again but some times it just remains moving slowly back and forth.

It was observed that some of the liquid plugs split up to form two separate plugs and that two plugs sometimes coalesce to form a single plug. It was also possible to see the liquid film deposited at the trailing end of a liquid plug and the evaporation thereof.

5.4 Water Charged Stainless Steel Closed End Pulsating Heat Pipe

A PHP was manufactured from stainless steel (4.76 mm OD and 3.34 mm ID) and filled with water as the working fluid. The aim of the experiment was to define and determine a heat transfer coefficient which can be used to design PHPs in future and to determine the amount of heat transferred by the PHP and to compare it to that predicted by the theoretical model.

5.4.1 Experimental Set-up

A closed end PHP as shown in Figure 5.7(a) was constructed from 304 stainless steel tubing and was cast into aluminium to form the condenser and evaporator sections as shown in Figure 5.7(b) with W_e = 110 mm, W_a = 80 mm, W_c = 110 mm and L = 355 mm. The aluminium thickness of both the evaporator and condenser sections was 25 mm. The total length of the tube in the evaporator is L_e = 1.957 m and the total length of the tube in the condenser is L_c = 1.435 m. The number of channels is N_{chan} = 16.

A heating element consisting of electrical resistance wire and insulated with ceramic beads was inserted into the groove as shown in Figure 5.7(b) to serve as the heat source. Several cooling channels were drilled through the condenser section through which water flowed from a constant head source to serve as the heat sink. The water outlets can be seen in Figure 5.7(b). The PHP is mounted onto a stand as shown in Figure 5.8. The stand can rotate making it possible for the heat pipe to be rotated in order to evaluate its performance at different inclination angles. The inclination angle is defined as shown in Figure 5.9 to be consistent with the convention used in the theoretical model. The inclination angle of the PHP as shown in Figure 5.8 is therefore $\phi = 0°$, $\phi = +90°$ would be bottom heat mode and $\phi = -90°$ would be top heat mode.

A voltage regulator (Yokoyama, model SB-10, serial no. 24653 and store no. 231568) is connected to the heating element in the evaporator section making it possible to vary the heat input. At the water outlet a needle valve is connected to control the mass flow rate of the

cooling water. Temperature readings are taken at several locations in the evaporator and condenser sections, as well as the cooling water inlet and outlet using T-type thermocouples. The data is logged using a Hewlett Packard data logger (model 34970A, serial no. 37008090). The PHP is filled with water liquid that is treated to remove any non-condensable gasses. For the treatment of the water liquid and the filling procedure refer to APPENDIX A.

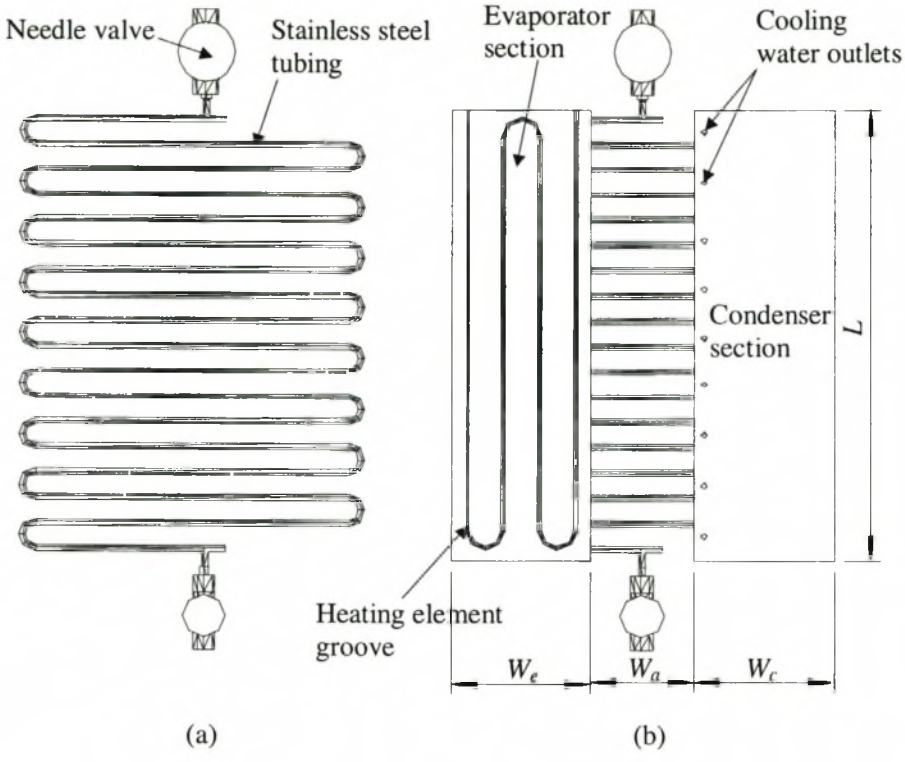

Figure 5.7 Stainless steel PHP (4.76mm OD, 3.34mm ID)

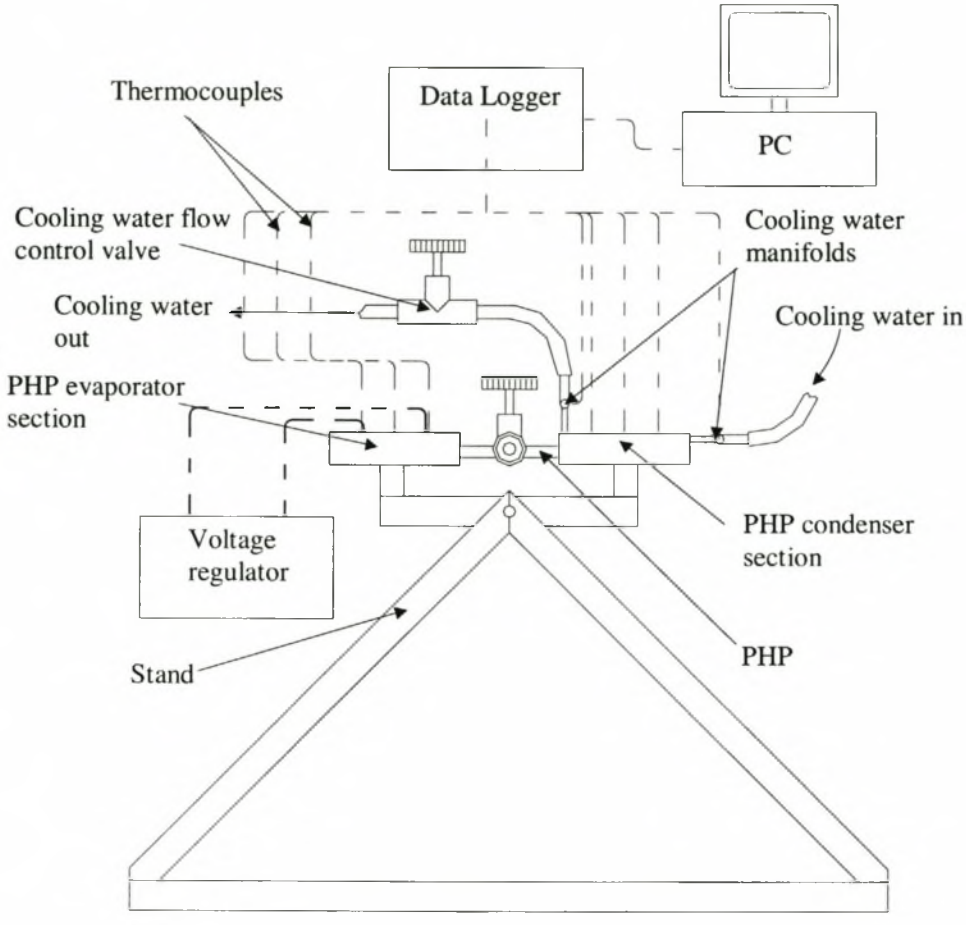

Figure 5.8 Experimental setup of stainless steel water charged PHP

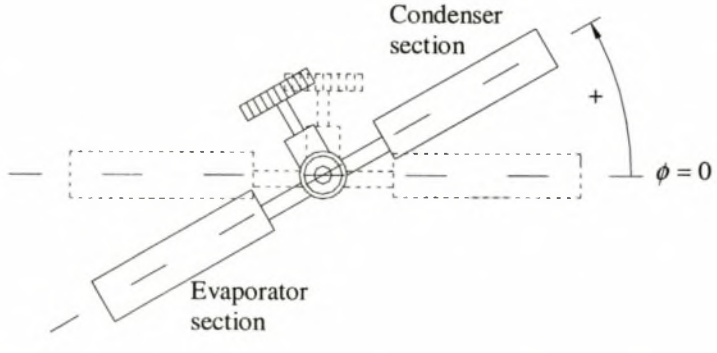

Figure 5.9 Definition of the inclination (to the horizontal) angle of the PHP

5.4.2 Results

Typical temperature readings obtained during the experiments are shown in Figure 5.10 for an inclination angle of ϕ = -30° and a filling ratio of R = 0.56. Also shown in Figure 5.10 is the electrical power input, $\dot{Q}_{elec}$, and the energy transferred to the cooling water, $\dot{Q}_{cw}$. From

Figure 5.10 it can be seen that as the average temperature of the evaporator section increases up to $\overline{T}_e \approx 55$ °C the PHP starts to transfer heat to the condenser section. The temperature of the condenser section starts to increase up to a point where it is more or less constant at $\overline{T}_c \approx$ 20 °C. At this point the operating temperature of the evaporator section is approximately $\overline{T}_e \approx$ 66 °C. From the results it can also be seen that the heat transferred to the cooling water follows the temperature of both the condenser and evaporator section. For example, at t ≈ 3000 s the temperature of the condenser section increases from $\overline{T}_c \approx 20$ to 25 °C accompanied by a drastic increase in the heat transferred to the cooling water from $\dot{Q}_{cw} \approx 50$ to 100 W. During this period the temperature of the evaporator decreases to $\overline{T}_e \approx 63$ °C. It is clear from the results that heat is not transferred steadily, but in a "pulsating" fashion due to the very physical nature of the PHP.

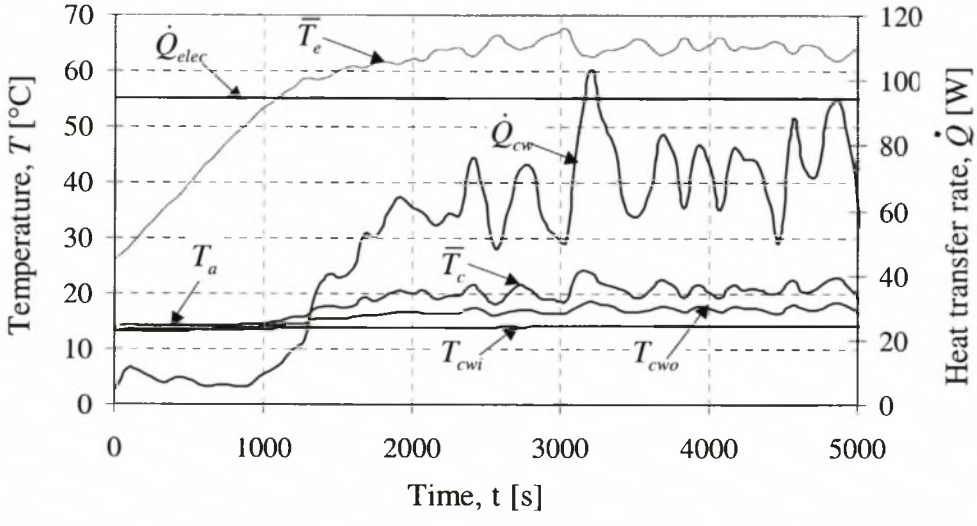

Figure 5.10 Typical results obtained for a water filled closed end PHP with a fill ratio of R = 0.56 operating at an inclination angle of ϕ = -30°

5.4.3 Pulsating Heat Pipe Heat Transfer Coefficient

A heat transfer coefficient will now be defined and determined. The heat transfer would assist in the design of similar PHPs in future. The important features of the PHP test set-up are shown in Figure 5.11. For convenience the important temperatures are shown separately in Figure 5.12. Based on these two figures a thermal resistance diagram of the PHP test set-up is given in Figure 5.13. Electrical power $\dot{Q}_{elec} = V^2/R_{elec}$ is supplied at a steady rate to the

evaporator and heat is removed from the condenser section by the cooling water as $\dot{Q}_{cw} = \dot{m}_{cw} c_{pcw} (T_{cwe} - T_{cwi})$. Heat is lost to the environment from the evaporator $\dot{Q}_{el} = (\overline{T}_e - T_a)/R_{el}$, condenser $\dot{Q}_{cl} = (\overline{T}_c - T_a)/R_{cl}$ and from the tubes between the evaporator and condenser $\dot{Q}_{wia} = (T_{wi} - T_a)/R_{wia}$.

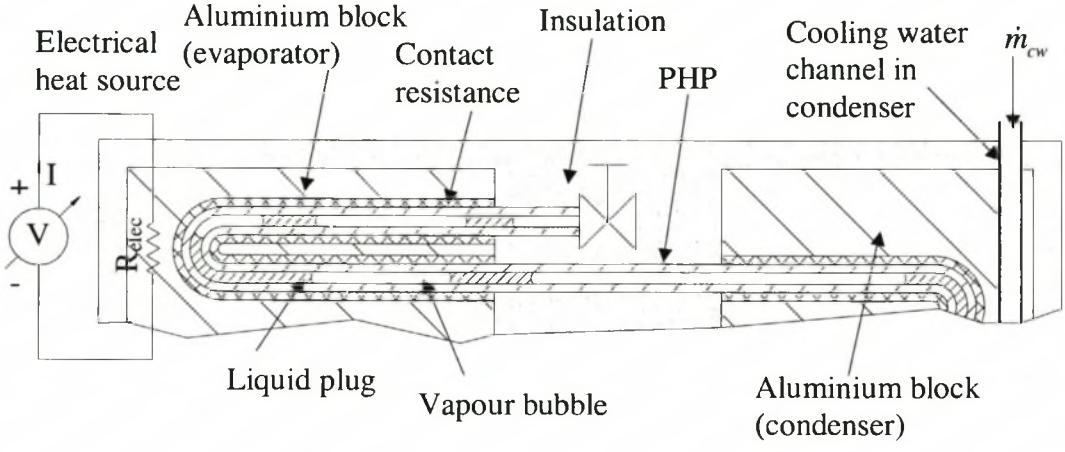

Figure 5.11 Important features of the PHP set-up

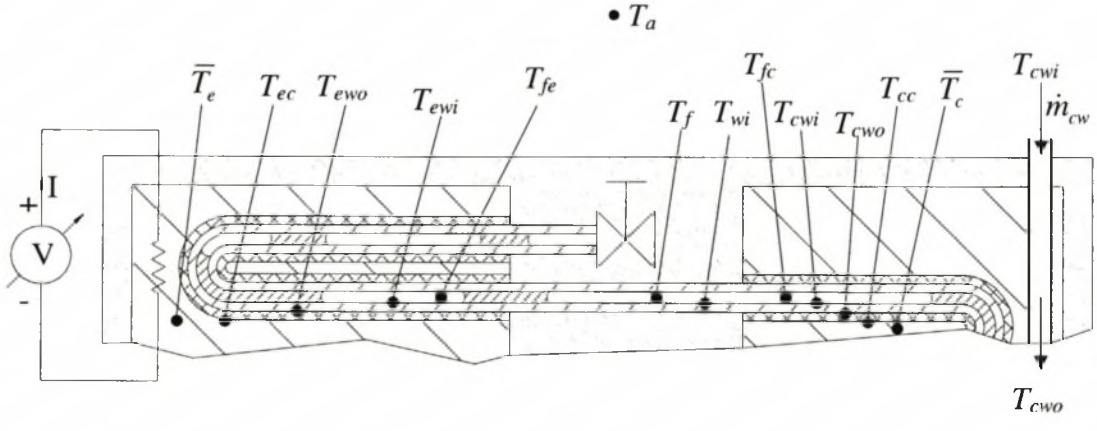

Figure 5.12 Important temperatures of the PHP test set-up

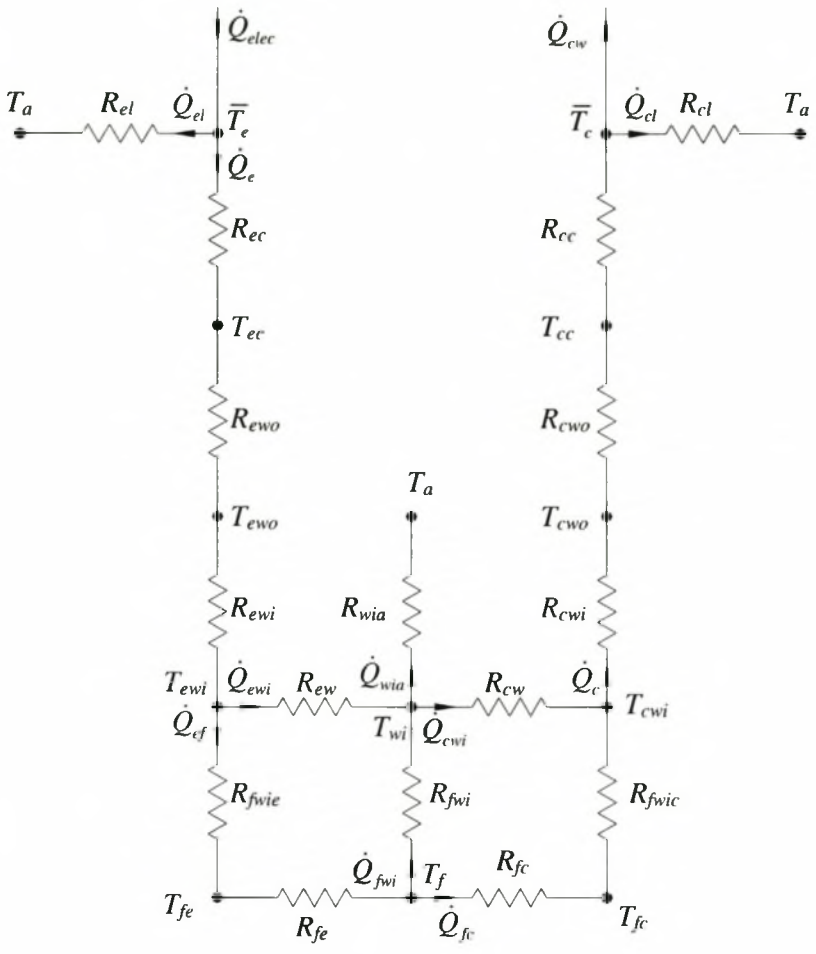

Figure 5.13 Thermal resistance diagram of the PHP test set-up

The thermal resistance diagram given in Figure 5.13 is still too complicated and may be further simplified. In APPENDIX C a sample calculation is done which illustrates that the difference in temperature between the evaporator and the inner wall of the PHP in the evaporator section is typically $\overline{T}_e - T_{ewi} \approx 0.08 + 0.169 = 0.249$ °C and therefore $\overline{T}_e \approx T_{ewi}$. This will also be true for the condenser section so that $T_{cwi} - \overline{T}_c \approx 0.229$ °C and $\overline{T}_c \approx T_{cwi}$. It is also shown that the loss $\dot{Q}_{wia} \approx \dot{Q}_{fwi} \approx$ 1.28 W. The heat conducted through the PHP walls from the evaporator to the condenser is therefore $\dot{Q}_{ewi} = \dot{Q}_{cwi} = \left(\overline{T}_e - \overline{T}_c\right)/\left(R_{ew} + R_{cw}\right)$. Taking the above into account the thermal diagram in Figure 5.13 is further simplified as given in Figure 5.14.

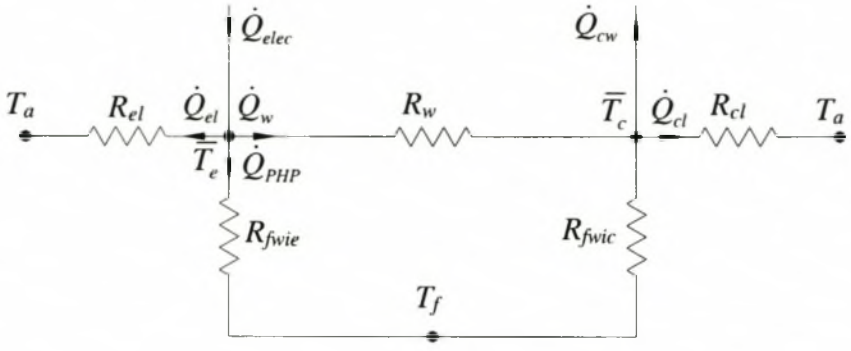

Figure 5.14 Simplified thermal resistance diagram of the PHP test set-up

The simplified thermal resistance diagram in Figure 5.14 allows a definition of a heat transfer coefficient h_{ei} between the inner wall and the working fluid for the evaporator as

$$\dot{Q}_{PHP} = \frac{\overline{T}_e - T_f}{R_{fwie}} \tag{5.1}$$

where $R_{fwie} = \dfrac{1}{h_{ei}\pi d_i L_e}$

Similarly a heat transfer coefficient h_{ci} between the inner wall and the working for the condenser is

$$\dot{Q}_{PHP} = \frac{T_f - \overline{T}_c}{R_{fwic}} \tag{5.2}$$

where $R_{fwic} = \dfrac{1}{h_{ci}\pi d_i L_c}$

However, no indication exist as to what the temperature of the fluid is since it was not measured. Even if it was measured, the fluid temperature would still be ill-defined since the temperature at any position in the PHP will vary as liquid plugs and vapour bubbles pass this point. As a compromise a *heat transfer coefficient* h_{PHP} is defined by the following two equations

$$\dot{Q}_{PHP} = \frac{\overline{T}_e - \overline{T}_c}{R_i} \tag{5.3}$$

where $R_i = R_{fwie} + R_{fwic} = \dfrac{1}{h_{ei}\pi d_i L_e} + \dfrac{1}{h_{ci}\pi d_i L_c}$

It is not possible to be able to define a constant temperature for the working fluid T_f. Consequently it is defined that $h_{ei} \approx h_{ci} \approx h_{PHP}$ and equation (5.3) becomes

$$\dot{Q}_{PHP} = \frac{h_{PHP}\pi d_i\left(\overline{T}_e - \overline{T}_c\right)}{\dfrac{1}{L_e} + \dfrac{1}{L_c}} \tag{5.4}$$

To calculate h_{PHP} $\dot{Q}_{el}$ or $\dot{Q}_{cl}$ and $\dot{Q}_w$ are required. $\dot{Q}_{el}$ and $\dot{Q}_{cl}$ may be determined experimentally. This is done by drawing a vacuum in the PHP and applying a constant electrical power input to the set-up. The cooling water is also turned off which results in a further simplification of the thermal circuit in Figure 5.14 to the thermal resistance diagram shown in Figure 5.15. When steady conditions are reached the heat loss from the evaporator section is known for the temperature difference between the evaporator section and the ambient temperature and similarly the heat loss from the condenser is known for the temperature difference between the condenser section and the ambient. Different electrical power inputs are applied to the evaporator section to obtain different heat losses for different temperature differences between the evaporator and condenser sections and the ambient. The results of the heat loss calibration are shown in Figure 5.16 as $\dot{Q}_{el} = 0.2433\left(\overline{T}_e - T_a\right)$ and $\dot{Q}_{cl} = 0.1926\left(\overline{T}_c - T_a\right)$.

The heat conducted by the tube walls may be given by

$$\dot{Q}_w = \left(\overline{T}_e - \overline{T}_c\right) / R_w \tag{5.5}$$

where $R_w = \dfrac{1}{\dfrac{k}{W_a}A_w}$, $A_w = n_{chan}\pi(d_o^2 - d_i^2)/4$

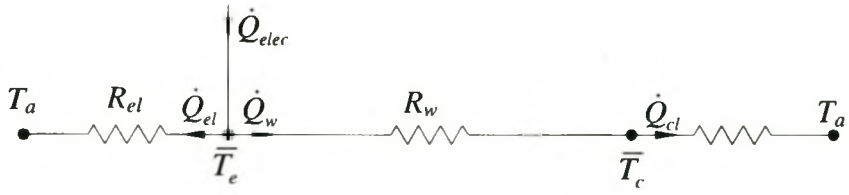

Figure 5.15 Thermal resistance diagram for the heat loss calibration for PHP set-up

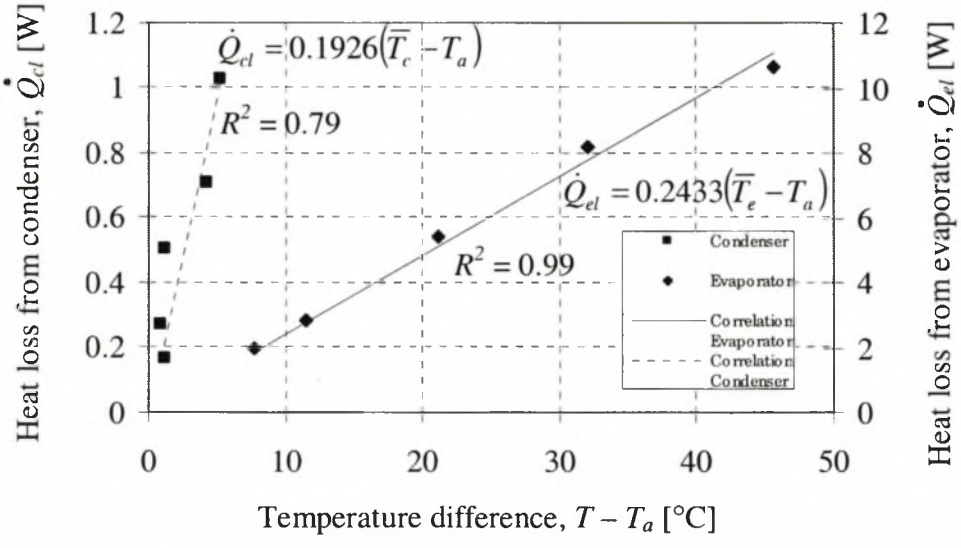

Figure 5.16 The evaporator and condenser heat losses to the ambient

The PHP heat transfer coefficient can now be determined. The PHP heat transfer coefficient is determined for different operating conditions of which the results are shown in Figure 5.17. From the results it can be seen that the inclination angle has an effect on the performance of the PHP. The heat transfer coefficient in the top heat mode (ϕ = -90°) is less than when the heat pipe is operated in the bottom heat mode (ϕ = +90°). It can also be seen that the filling ratio, R, affects the performance of the PHP. The heat transfer coefficient is higher for R = 0.56 than for both R = 0.61 and R = 0.46, suggesting that the optimum filling ratio for this PHP lies approximately in the range $0.45 < R < 0.6$.

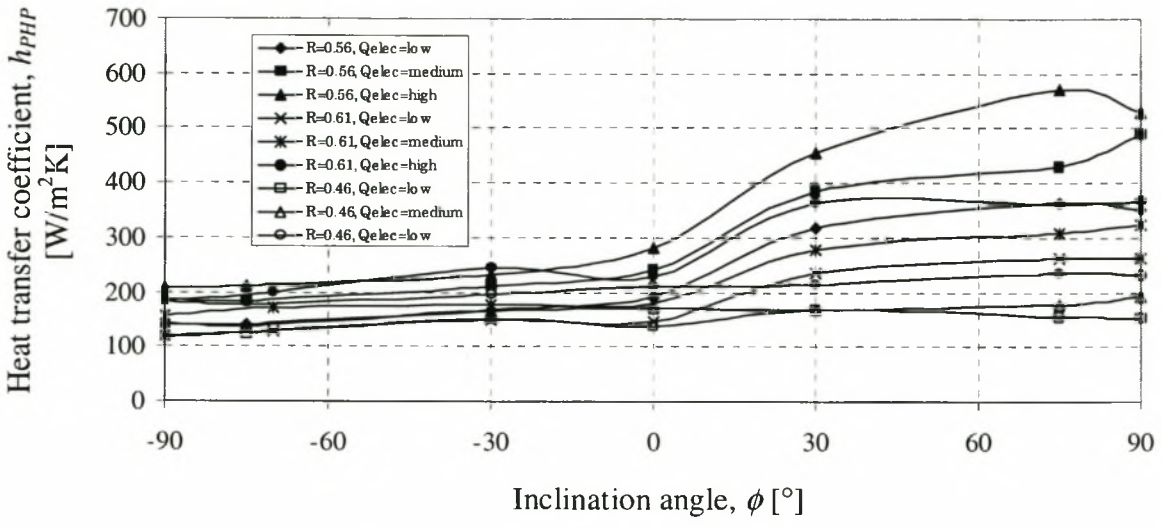

Figure 5.17 Experimental results of the heat transfer coefficient h_{PHP} of the water filled PHP at different inclination angles and electrical power input

The heat transfer coefficient was correlated with the temperature difference, $\overline{T}_e - \overline{T}_c$, $\phi + 92°$ (the reason for adding 92° will follow) and R as follows

$$h_{PHP} = 9224.207\left(\overline{T}_e - \overline{T}_c\right)^{-1.041}(\phi + 92)^{0.007} R^{-0.095} \tag{5.6}$$

The heat transfer coefficient was also correlated with $\overline{T}_e - \overline{T}_c$, ϕ + 92°, R and $\frac{\overline{T}_e + \overline{T}_c}{2}$ as follows

$$h_{PHP} = 1.392\left(\overline{T}_e - \overline{T}_c\right)^{-2.304}(\phi + 92)^{0.043} R^{-0.377}\left(\frac{\overline{T}_e + \overline{T}_c}{2}\right)^{3.524} \tag{5.7}$$

The coefficients in equation (5.6) (5.7) are determined by performing a multi-linear regression analysis on the data as was similarly done in section 4.3. In order to do the regression the numerical values of the inclination angle had to be changed to avoid taking the natural logarithm of negative numbers. The values of the inclination angles were therefore changed by adding 92°. The inclination angle is a convention defined to assist in visualising the experimental set-up more effectively. By adding 92°, the results are not effected in anyway and are still in agreement with the physical phenomena taking place. The values of h_{PHP} predicted by equation (5.6) are compared to the experimental values in Figure 5.18 and

that by equation (5.7) in Figure 5.19. It can be seen that the R^2 value is higher for the correlation given by equation (5.7) than the correlation given by equation (5.6).

Looking at equation (5.6) and (5.7) it can be seen that the greater the temperature difference between the fluid temperature and the condenser section the lower the heat transfer coefficient. It can also be seen that the heat transfer coefficient is proportional to the inclination angle meaning that it will be higher when the PHP is operated in the bottom heat mode than when operated in the top heat mode. The correlations also predict that the heat transfer coefficient will be higher for a smaller filling ratio.

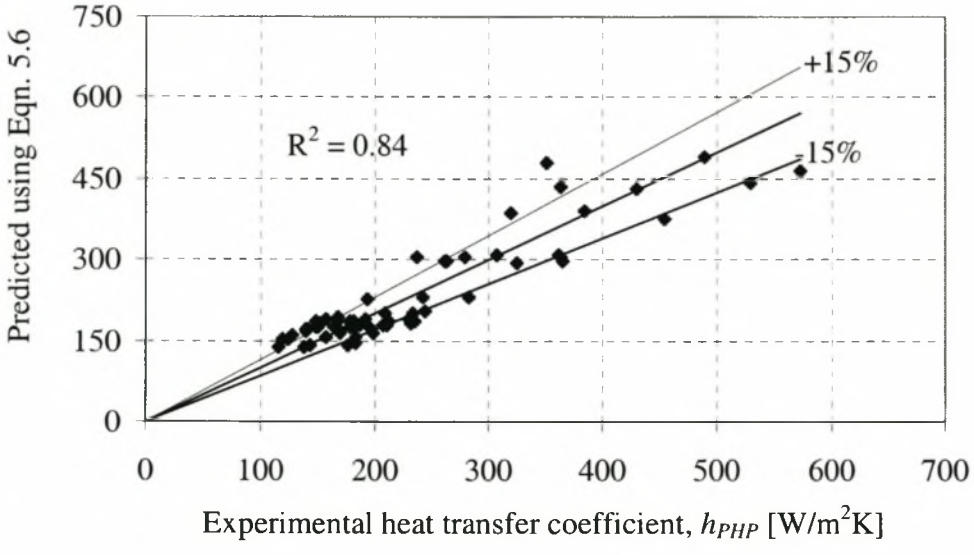

Figure 5.18 Heat transfer coefficient h_{PHP} as predicted by Equation (5.6) compared to the experimental values

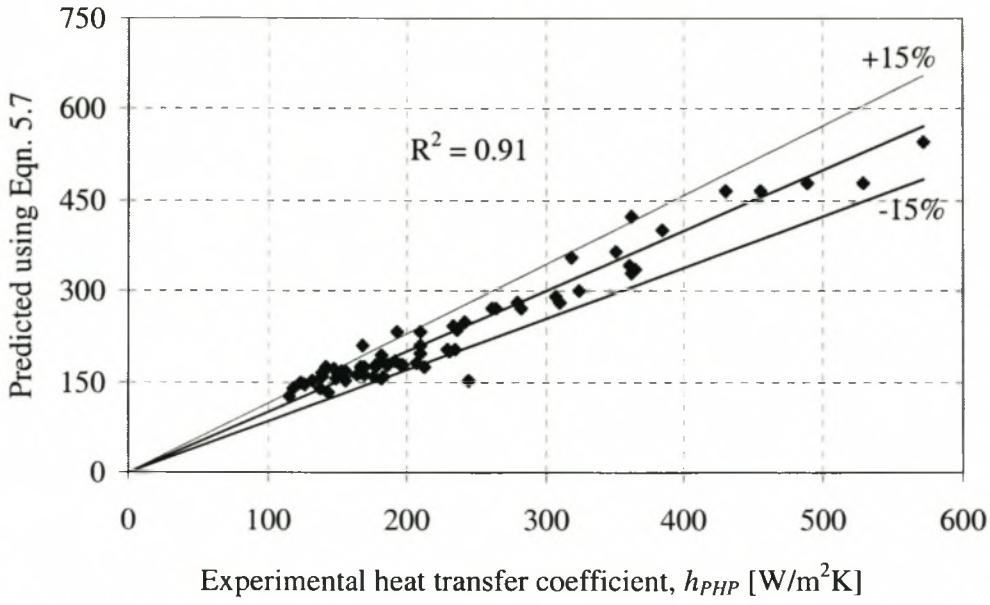

Figure 5.19 Heat transfer coefficient h_{PHP} as predicted by Equation (5.7) compared to the experimental values

5.4.4 Comparison of Experimental Results with Theoretical Results

The closed end stainless steel PHP was numerically modelled using the theoretical model (filename: php1ver6H2O_multiplug_actual.pas). The values used for the geometry and initial conditions are summarised in Table 5.2. Refer to Figure 3.19 for the definition of the geometry. The geometry of the theoretical model does not match that of the actual model due to the restricted capabilities of the program to divide the PHP into finite elements. The heat transfer rate as a function of the inclination angle predicted by the theoretical model is compared to that experimentally obtained for the PHP with R = 0.46 and $\dot{Q}_{elec}$ = 78 W in Figure 5.20. It can be seen that the theoretically predicted heat transfer rate compares good with the experimental results for the top heat mode ($-90° < \phi < 0°$). In the bottom heat mode the theoretically predicted values are significantly higher than the experimentally determined values.

Table 5.2 Initial conditions and geometry to simulate a closed end PHP

$(x_{p0})_i$ (where i is the plug number)	281.25 x i mm
T_{v0}	40 °C
p_{v0}	7238 Pa
L_{pe}	135 mm
L_{pc}	140 mm
$L_c/8$	181.125 mm
$L_e/8$	221.375 mm
W_a	80 mm
L_{tube}	4 500 mm
d_i	3.34 mm
T_{we}	60 °C
T_{wc}	40 °C
$\delta_{\ell f}$	0.0001 m
$h_{\ell fw}$ (evaporator and condenser)	800 W/m^{2}K
h_{wv} (evaporator and condenser)	10 W/m^{2}K
$h_{\ell fv}$ (evaporator and condenser)	10 W/m^{2}K
$h_{\ell fw}$, h_{wv}, $h_{\ell fv}$ (adiabatic region)	0 W/m^{2}K

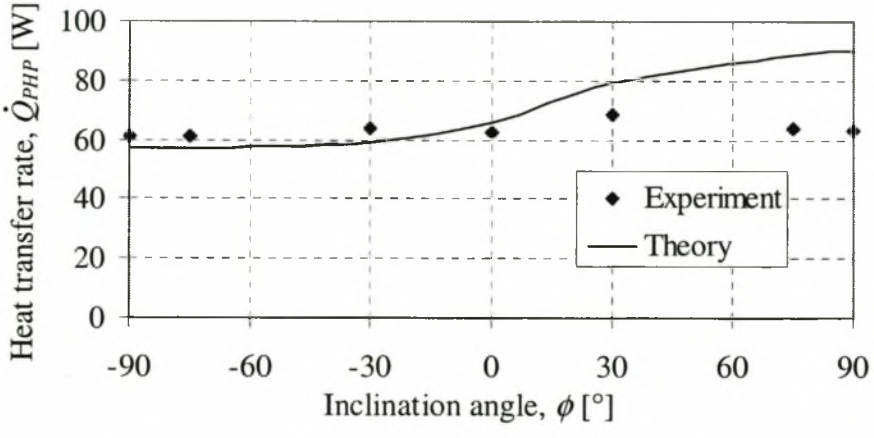

Figure 5.20 Comparison of the experimentally determined heat transfer rate with the theoretically predicted heat transfer rate

5.5 Water Charged Aluminium Pulsating Heat Pipe

The PHP of section 5.4 was made of stainless steel. Another PHP was manufactured from 3003 aluminium (4.76 mm OD and 3.34 mm ID) and filled with water as the working fluid. The aim of the experiment was to determine amount of heat transferred by the PHP and the PHP heat transfer coefficient as defined by equation (5.4).

5.5.1 Experimental Set-up

The PHP constructed was of the closed loop type and is shown in Figure 5.21(a). The PHP was positioned into grooves machined into aluminium blocks with L = 364 mm, W_e = 115 mm, W_a = 80 mm and W_c = 111 mm as shown in Figure 5.21(b). The total length of the tube in the evaporator is L_e = 1.953 m and the total length of the tube in the condenser is L_c = 1.965 m. The number of channels is N_{turns} = 18. The grooves were filled with pure tin to ensure good thermal contact between the aluminium blocks and the outer wall of the aluminium tube. The assembly as shown in Figure 5.21(b) was insulated, mounted onto the rotating stand, connected to the data capturing system, electrical power and cooling water supply in the same manner as for the closed end stainless steel PHP (see section 5.4).

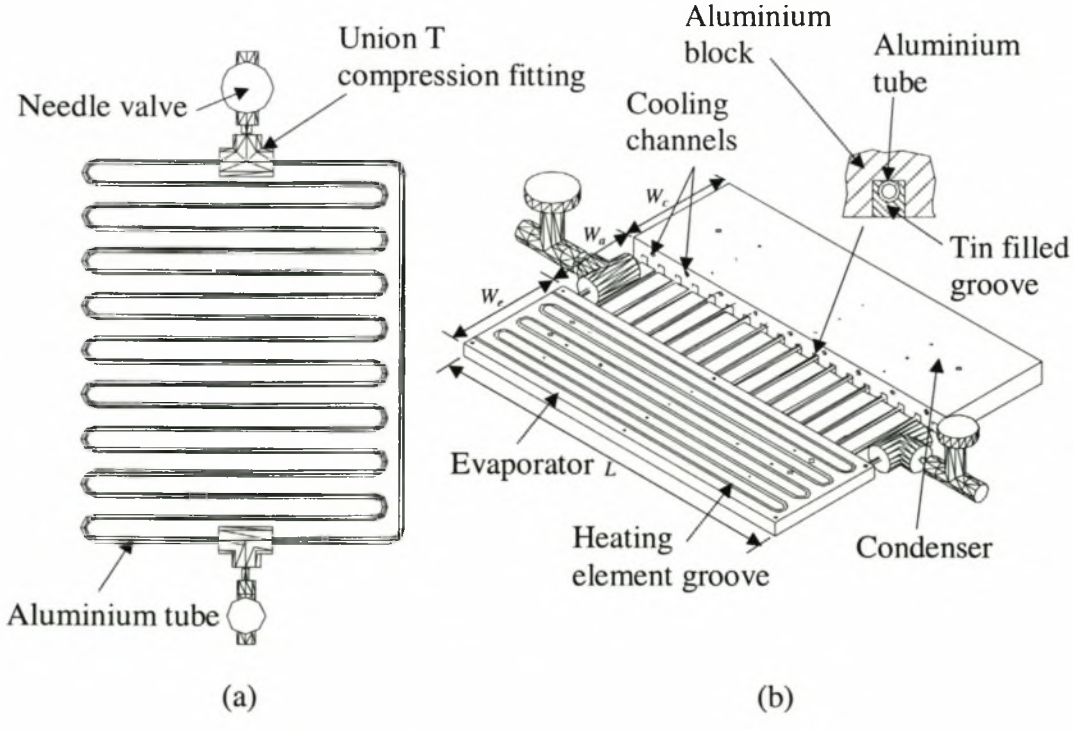

Figure 5.21 Aluminium closed loop PHP (4.76m OD, 3.34mm ID)

5.5.2 Results

Typical temperature readings obtained during the experiments are shown in Figure 5.22 for an operating angle of $\phi = 30$ ° and a filling ratio of $R = 0.46$. The electrical power $\dot{Q}_{elec}$ supplied to the evaporator and the heat transferred to the cooling water $\dot{Q}_{cw}$ are also indicated in Figure 5.22. It can be seen from the results that the temperature of the evaporator increases to $\overline{T}_e \approx 43$ °C where it starts to transfer heat to the condenser at $\overline{T}_c \approx 23$ °C.

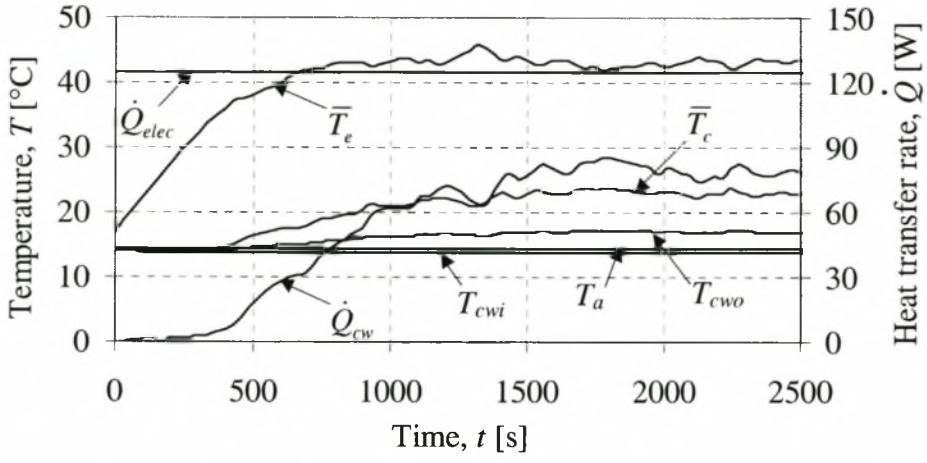

Figure 5.22 Typical results obtained for a water filled closed loop PHP with a fill ratio of $R = 0.46$ operating at an inclination angle of $\phi = 30$ °

5.5.3 Pulsating Heat Pipe Heat Transfer Coefficient

The heat transfer coefficient h_{PHP} in the evaporator section as defined by equation (5.4) is shown in Figure 5.23 as a function of different inclination angles, filling ratios and electrical power inputs. As with the closed end stainless steel PHP it can be seen that the heat transfer coefficient is a minimum in the top heat mode ($\phi = -90°$) and increases to obtain maximum values in the bottom heat mode ($\phi = 30° - 90°$). It can be seen that no results are available for $R = 0.66$, $\dot{Q}_{elec}$ = medium at $\phi = -90°$, $R = 0.66$, $\dot{Q}_{elec}$ = low at $\phi = -90°$, -75°, -30°, 0° and $R = 0.5$, $\dot{Q}_{elec}$ = low at $\phi = -90°$, due to the fact that the PHP did not operate at these testing conditions. From the results it is unclear what the optimum fill ratio is.

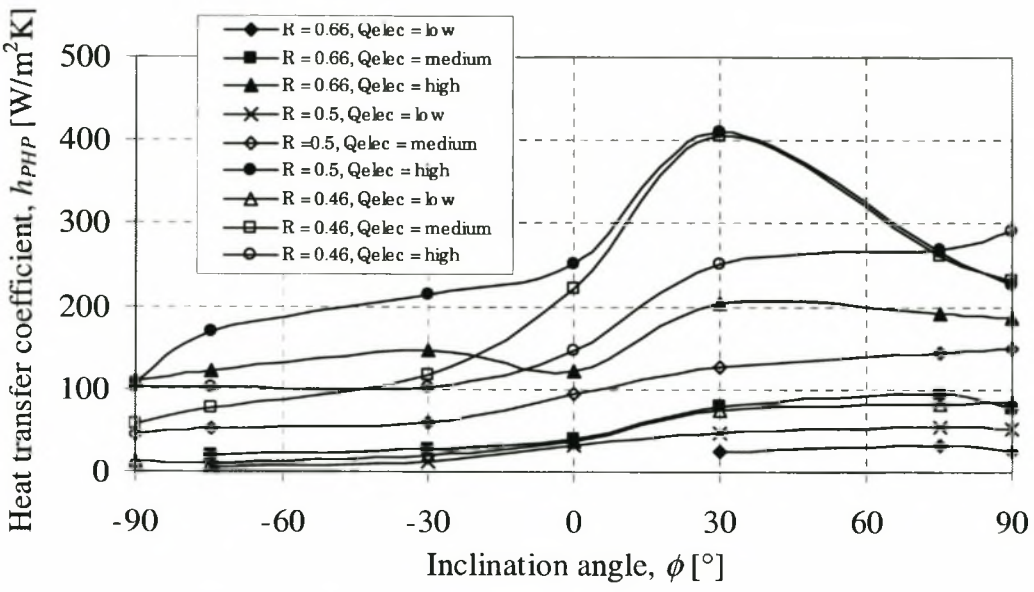

Figure 5.23 Heat transfer coefficient h_{PHP} as a function of the incliniation angle for different filling ratios and electrical power inputs for the water filled aluminium closed loop PHP

The heat transfer coefficient h_{PHP} was correlated with the temperature difference $\overline{T}_e - \overline{T}_c$, $\phi +$ 92° and R as

$$h_{PHP} = 7.117\times10^{9}\left(\overline{T}_e - \overline{T}_c\right)^{-3.884}\left(\phi + 92\right)^{-0.269} R^{2.304} \tag{5.8}$$

The heat transfer coefficient was also correlated with $\overline{T}_e - \overline{T}_c$, $\phi + 92°$, R and $\frac{\overline{T}_e + \overline{T}_c}{2}$ as

$$h_{PHP} = 1.932\times10^{7}\left(\overline{T}_e - \overline{T}_c\right)^{-6.383}\left(\phi + 92\right)^{-0.205} R^{1.882}\left(\frac{\overline{T}_e + \overline{T}_c}{2}\right)^{4.196} \tag{5.9}$$

The coefficients in equation (5.8) and (5.9) are determined by performing a linear regression analysis on the experimental data. The values of h_{PHP} predicted by equation (5.8) are compared to the experimental values in Figure 5.24 and that by equation (5.9) in Figure 5.24.

From equations (5.8) and (5.9) it can be seen that the greater the difference between the evaporator and fluid temperatures the lower the heat transfer coefficient. According to equations (5.8) and (5.9) the heat transfer coefficient increases with decreasing inclination angle which means that the heat transfer coefficient will be higher in the top heat mode than

in the bottom heat mode despite the fact that the PHP did not operate at some instances in the top heat mode.

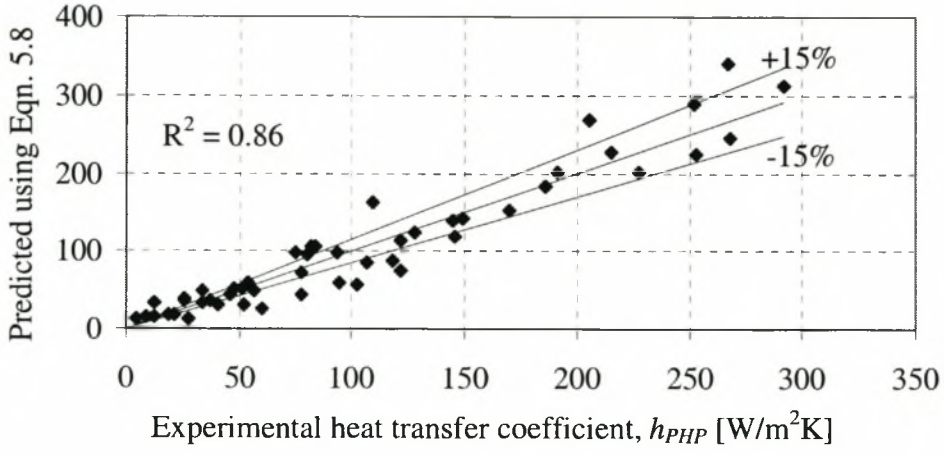

Figure 5.24 Heat transfer coefficient as predicted by equation (5.8) compared to the experimental values

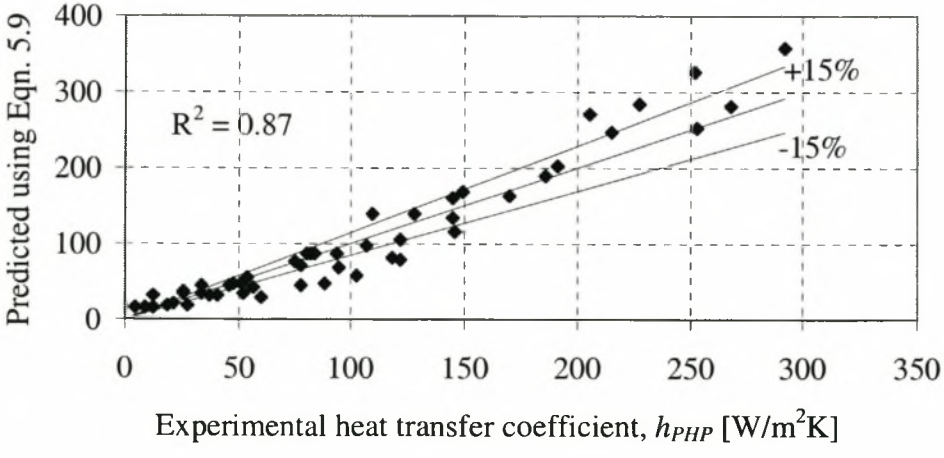

Figure 5.25 Heat transfer coefficient as predicted by equation (5.7) compared to the experimental values

5.6 Ammonia Charged Stainless Steel Pulsating Heat Pipe

The closed end stainless steel PHP as described in section 5.4 was filled with ammonia as the working fluid. The aim of the experiment was to determine the amount of heat transferred by the PHP and the PHP heat transfer coefficient as defined by (5.4).

5.6.1 Experimental set-up

The experimental set-up for this experiment is exactly the same as described in section 5.4. The only difference is that the PHP is filled with ammonia now instead of water. For the filling procedure refer to APPENDIX B.

5.6.2 Results

It was found that the PHP was capable to transfer heat only in the range $0° < \phi \leq 90°$. Typical temperature readings obtained during the experiments with inclination angles of $30° \leq \phi \leq 75°$ are shown in Figure 5.26. The results shown in Figure 5.26 are for an operating angle of $\phi = 30°$ and a filling ratio of $R = 0.46$. Also shown in Figure 5.26 is the electrical power input, $\dot{Q}_{elec}$, and the energy transferred to the cooling water, $\dot{Q}_{cw}$. From Figure 5.26 it can be seen that the average temperature of the evaporator section slowly increases up to $\overline{T}_e \approx 18$ °C where the PHP starts to transfer heat to the condenser section at a relatively steady rate. The temperature of the condenser section starts to increase up to a point where it is more or less constant at $\overline{T}_c \approx 21$ °C. At this point the operating temperature of the evaporator section is approximately $\overline{T}_e \approx 27$ °C and also remains relatively constant.

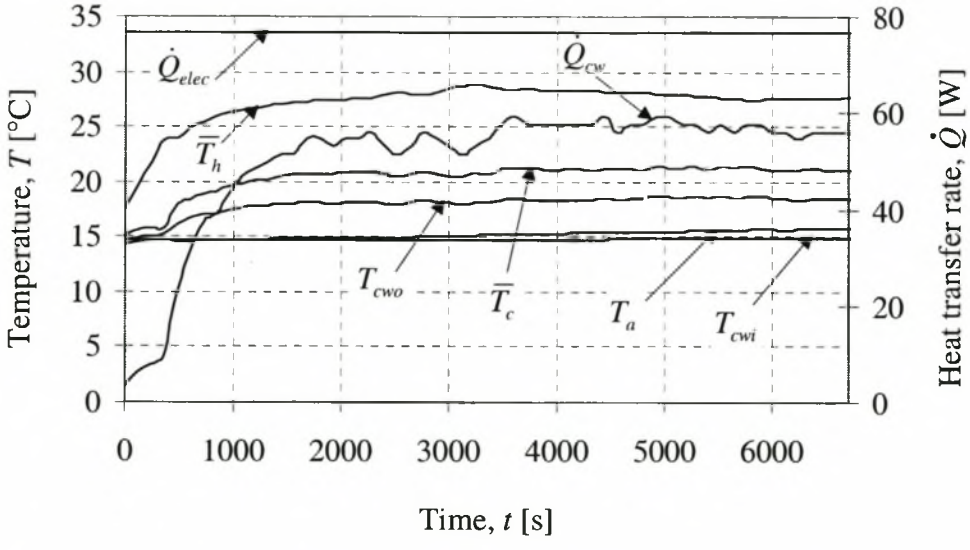

Figure 5.26 Typical experimental results for an ammonia filled closed end PHP with a fill ratio of $R = 0.46$ operating at an inclination angle of $\phi = 30°$

The typical results for an inclination angle of $\phi = 90°$ and fill ratio $R = 0.46$ are shown in Figure 5.27. Comparing the results in Figure 5.27 to the results in Figure 5.26 it can be seen

that the variation of the heat transferred to the cooling water, $\dot{Q}_{cw}$, is more erratic. This and the fact that the PHP does not transfer heat in the range $-90° \leq \phi \leq 0°$ suggest that the mechanism by which heat is transferred by the ammonia PHP is similar to that of a thermosyphon. A thermosyphon cannot transfer heat in the top heat mode, and if too much working fluid is present flooding can occur in a thermosyphon causing relatively high fluctuations in the heat transfer. To investigate whether this is the case consider the results shown in Figure 5.28 for a PHP with different fill ratios and $\phi = 90°$. From Figure 5.28 it can be seen that the heat transfer rate is more smooth for R = 0.16 than for R = 0.46. Also, the operation of a PHP relies on the formation of liquid plugs and vapour bubble inside the tube. In order for liquid plugs and vapour bubbles to form inside the tube, the inside diameter must be less than $d_i = 1.8(\sigma/(\rho_\ell - \rho_v)g)^{1/2} = 1.8(0.0181/(579.5-12)9.8)^{1/2} = 2.96$ mm at an operating temperature of T = 40 °C. The inside diameter of the stainless steel PHP is d_i = 3.34 mm which means that the flow inside the PHP is mostly stratified like in the case for a thermosyphon. It can therefore be concluded that the ammonia filled PHP is in fact a thermosyphon consisting of various interconnected tubes.

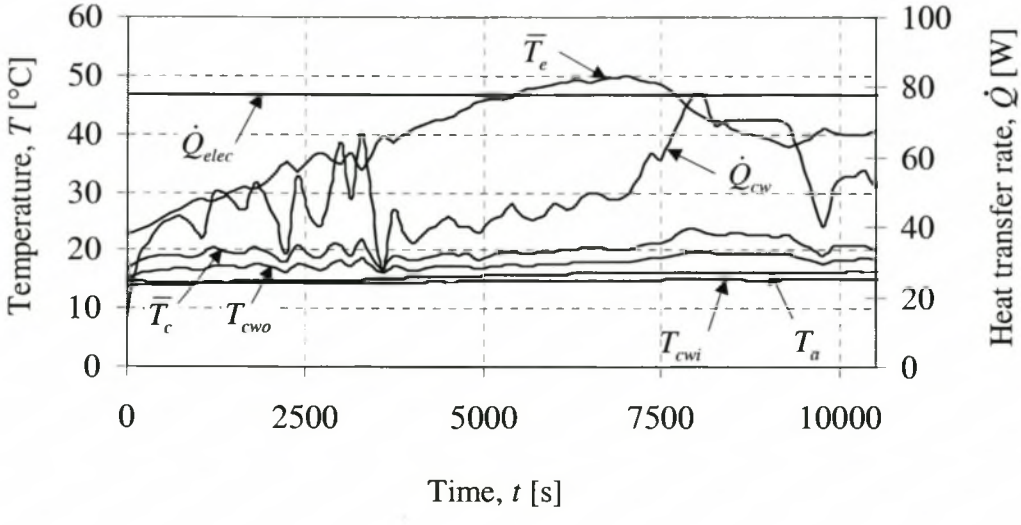

Figure 5.27 Typical experimental results for an ammonia filled PHP with a fill ratio of R = 0.46 operating at an inclination angle of $\phi = 90°$

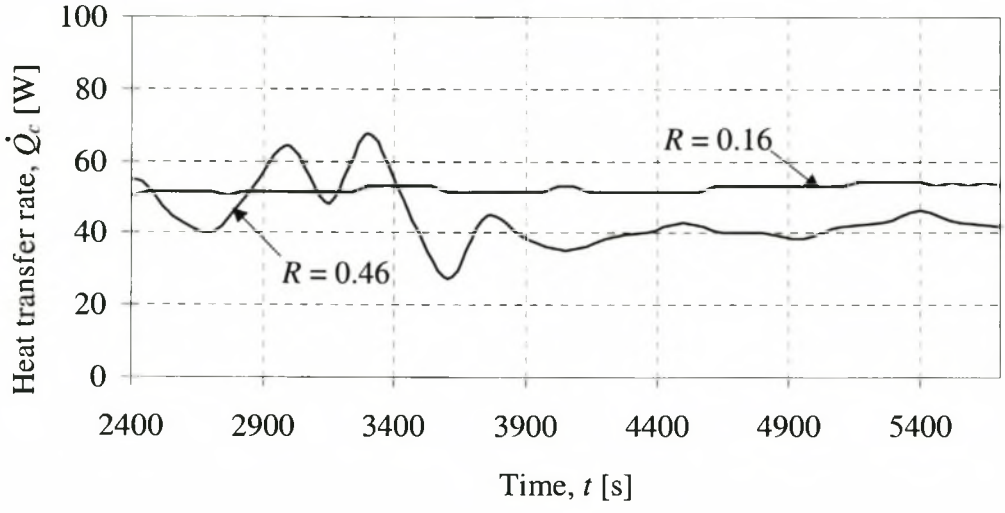

Figure 5.28 Comparison of the heat transfer rate to the cooling water for ϕ = 90 °, $\dot{Q}_{elec}$ = 75 W and different fill ratios

5.6.3 Pulsating Heat Pipe Heat Transfer Coefficient

The heat transfer coefficient in the evaporator section h_{PHP} as defined in equation (5.4) is shown in Figure 5.29 as a function of the inclination angle for different fill ratios and electrical power inputs. From Figure 5.29 it can be seen that the heat transfer coefficient is a minimum for ϕ = 90° increasing to a maximum in the region ϕ = 60 - 70° and then steadily decreases. The fact that the heat transfer coefficient is a minimum for ϕ = 90° supports the suggestion that flooding occurs at this angle.

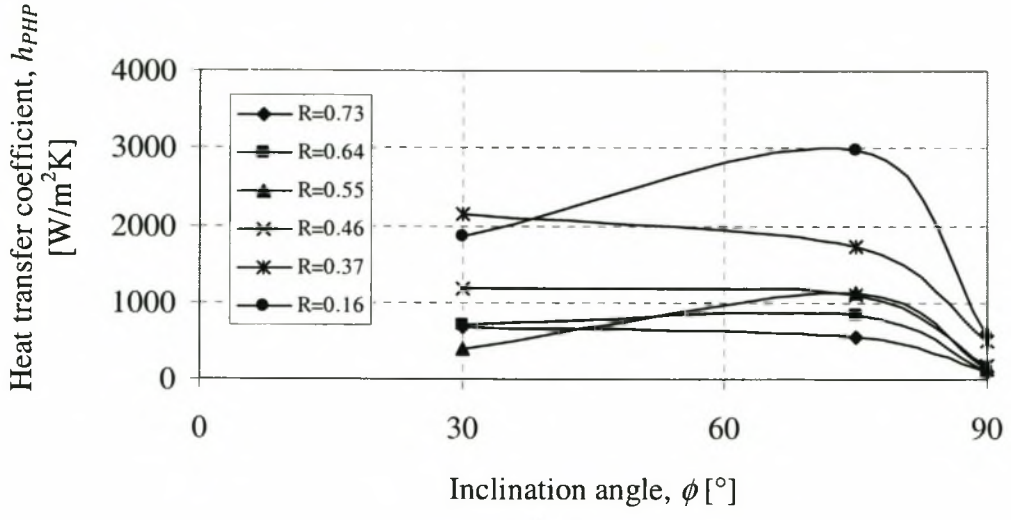

(a) $\dot{Q}_{elec}$ = 40 W

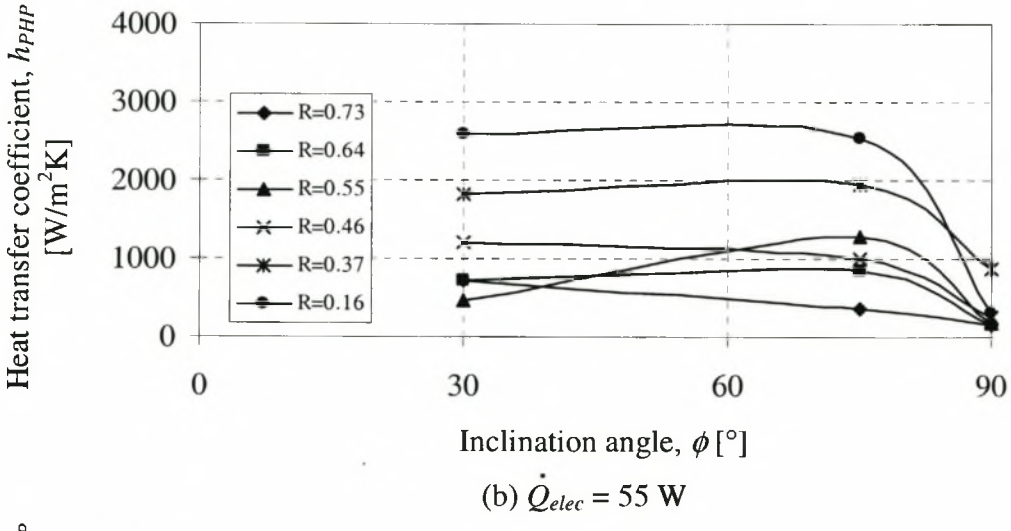

(b) $\dot{Q}_{elec}$ = 55 W

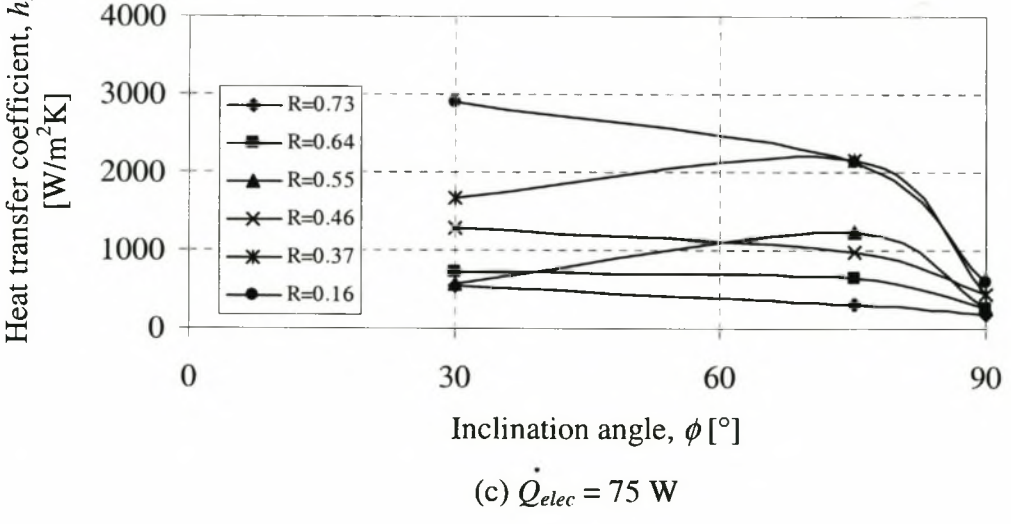

(c) $\dot{Q}_{elec}$ = 75 W

Figure 5.29 Heat transfer coefficient h_{PHP} as a function of the inclination angle for different power inputs for the ammonia filled stainless steel PHP

The heat transfer coefficient was correlated with the temperature difference $\overline{T}_e - \overline{T}_c$, ϕ and R as

$$h_{PHP} = 6667.373\left(\overline{T}_e - \overline{T}_c\right)^{-0.923} \phi^{-0.098} R^{-0.112} \tag{5.10}$$

The heat transfer coefficient was also correlated with $\overline{T}_e - \overline{T}_c$, ϕ, R and $\frac{\overline{T}_e + \overline{T}_c}{2}$ as

$$h_{PHP} = 26.563\left(\overline{T}_e - \overline{T}_c\right)^{-1.409} \phi^{-0.0406} R^{-0.028} \left(\frac{\overline{T}_e + \overline{T}_c}{2}\right)^{-0.923} \tag{5.11}$$

The coefficients in equations (5.10) and (5.11) are determined by performing a linear regression analysis on the data. The values of h_{PHP} predicted by the equation (5.10) are compared to the experimental values in Figure 5.30 and that by equation (5.11) in Figure 5.31. From equations (5.10) and (5.11) it can be seen that the greater the difference between the fluid temperature and the evaporator section the lower the heat transfer coefficient. The heat transfer coefficient is also indirectly proportionate to the filling ratio. From Figure 5.30 and Figure 5.31 it can be seen that the R^2 values is slightly higher for the correlation given by equation (5.11) than that given by equation (5.10).

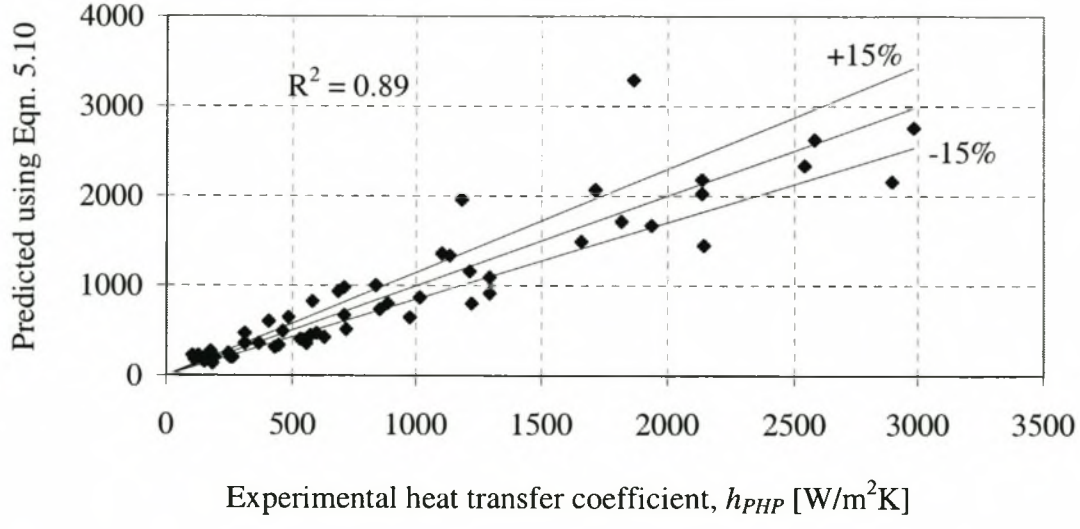

Figure 5.30 Heat transfer coefficient as predicted by equation (5.10) compared to the experimental values

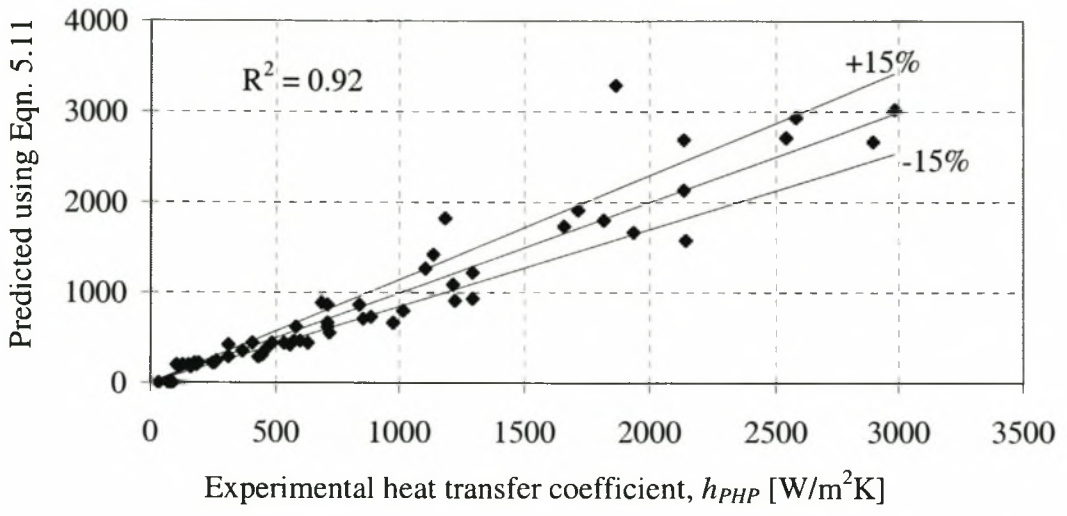

Figure 5.31 Heat transfer coefficient as predicted by equation (5.10) compared to the experimental values

6 APPLICATION OF PULSATING HEAT PIPES IN HEV's

An objective of this thesis is the investigation of the feasibility of using PHP technology for the thermal management of HEVs. Two components in particular were investigated namely the batteries and IGBTs. Several concepts were developed for the thermal management of these components and some problem areas were also identified regarding the thermal management.

6.1 Thermal Management of HEV Batteries

For the thermal management of HEV batteries a concept was developed using PHPs to control the temperature of the Optima Spirocell® (12 V, 65 Amp hour) lead acid batteries as used by CAE. Currently the batteries are positioned in the boot of the HEV as indicated in Figure 6.1. The batteries are covered with rubber sheets during the time this picture was taken and are therefore not visible in the figure. Figure 6.2 shows three batteries partially uncovered. As can be seen the batteries are in a confined space which is relatively well insulated. As a consequence the possibility exists that the temperature of the batteries could increase to above that of the desired temperature of 35 °C not only due to the normal operation of the batteries but also due to the heating of the boot when driving in sunny conditions. The batteries are also stacked against one another which means that the heat transfer area is effectively decreased. A possible solution to this problem could be developed using flat lane PHPs. The PHPs could be inserted between the batteries as shown in Figure 6.3 so that the heat can be transported away from the batteries to the outside of the body of the car where the heat can be rejected by natural convection when the car is stationary and by forced convection when the car is moving. When the car is moving forward the air will flow over the PHPs as indicated in Figure 6.3. To minimise radiation heat transfer from the sun to the PHPs, the surface of the PHPs should be coated with high emissivity and low absorptivity paint, or if this is inadequate, the PHPs could be covered with radiation shields or louvres. These radiation shields should be designed to allow convective heat transfer to still take place.

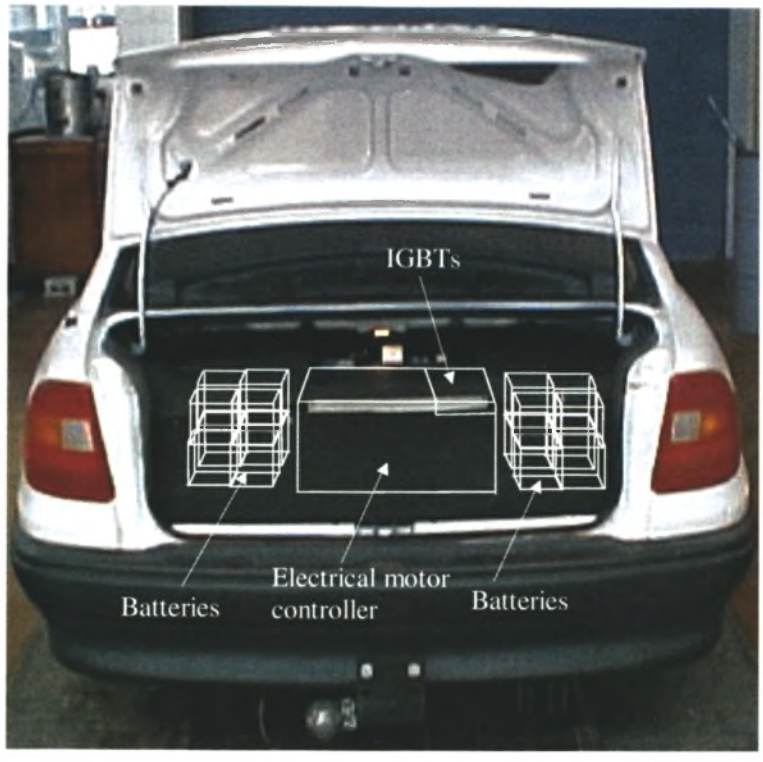

Figure 6.1 Positioning of the batteries and motor controller in the boot of the HEV

Figure 6.2 Partially uncovered batteries

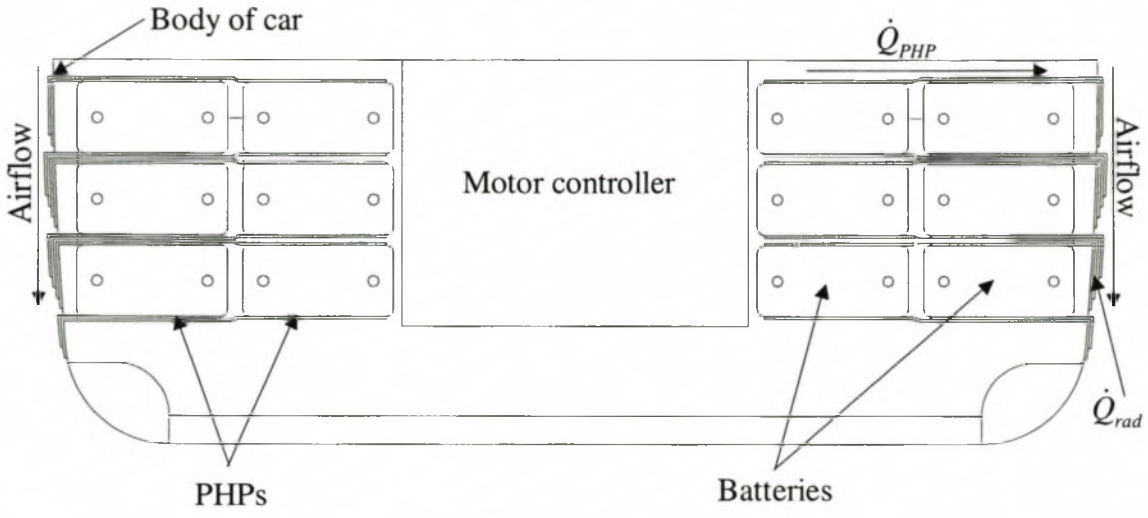

Figure 6.3 Concept illustrating how PHPs can be used to transport heat away from the batteries to the outside surface of the boot of the HEV

Richter (2000) conducted experiments whereby Raylite model 647 batteries were charged with a current of 40 A to determine the temperature response of the battery. It was found that the conduction thermal resistance of the battery-casing wall alone constitutes 65% of the thermal resistance from the middle of the battery to the environment. This means that the inside temperature of the battery could well exceed the specified 35 °C long before heat can be removed by the cooling concept described above due to the high thermal resistance of the battery-casing wall.

A solution to this problem might be that the PHP forms an integral part of the battery as shown in Figure 6.4. In Figure 6.4 the PHP is inserted into the battery so that it is in direct contact with the contents of the battery. This configuration will definitely be best from a heat transfer point of view, but it is unclear to what extent the performance of the battery will be influenced by the presence of the PHP. A more simple solution would be to manufacture the battery-casing from a material with higher thermal conductivity. The battery cell walls and casings may in fact be manufactured from casing material with PHPs embedded in the material itself. These suggestions would imply a redesign of batteries, which, for the present HEV project, is not practical or cost efficient.

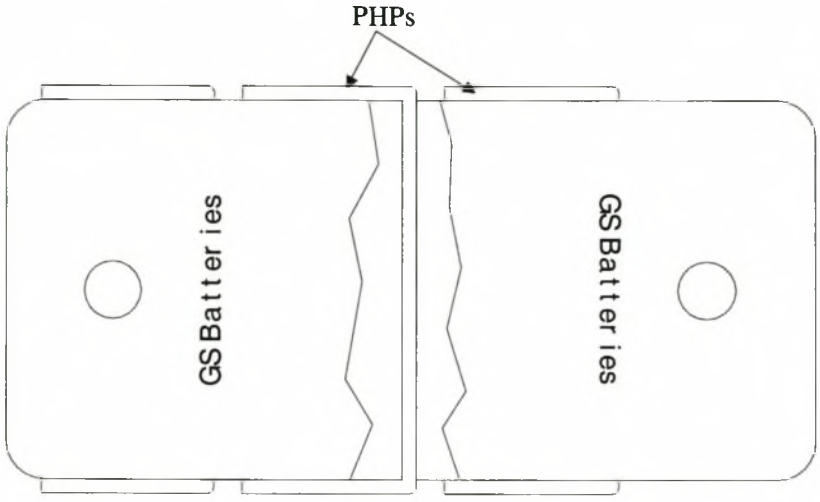

Figure 6.4 Insertion of PHPs into battery to transfer heat to outside of battery

The current HEV configuration does not include any thermal management of the batteries. It is recommended that status quo be maintained but that the thermal behaviour of the batteries should be determined when the HEV enters its testing phase. It can then be decided from the data obtained during the testing phase what the future course of action should be.

6.2 Thermal Management of IGBTs

The position of the IGBTs in the boot of CAE's HEV is indicated in Figure 6.1. Figure 6.5 shows a close-up view of the IGBTs and the cooling system. Figure 6.6 illustrates the cooling system more clearly. The method currently employed by the CAE to cool the IGBTs is to position the IGBTs on top of fins and to cool the fins using a fan. At the moment the cooling air is expelled back into the boot again, which theoretically will cause the air temperature to increase up to a stage where the IGBTs cannot be cooled. In practice, however, it is possible that a draft can exist in the boot which causes cooler air to enter the boot so that it is not a problem for the cooling air to be expelled back into the boot.

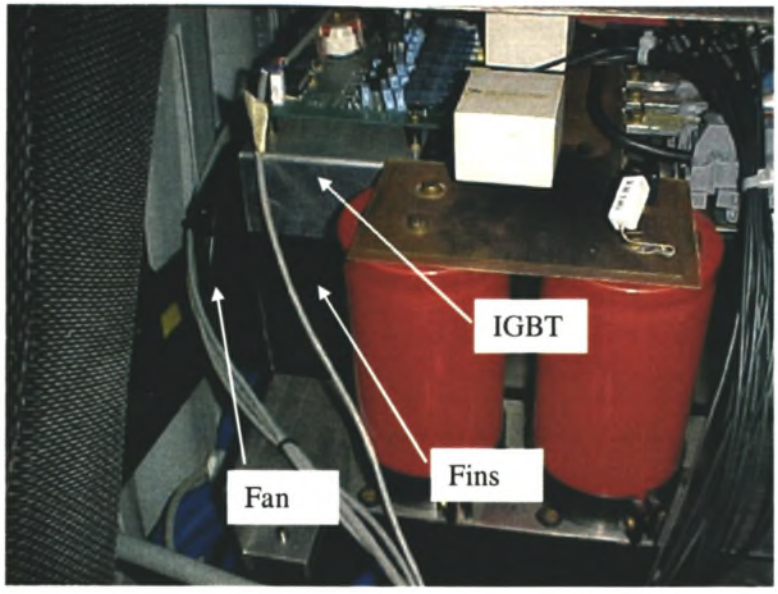

Figure 6.5 Close-up view of the IGBTs, fan and fins

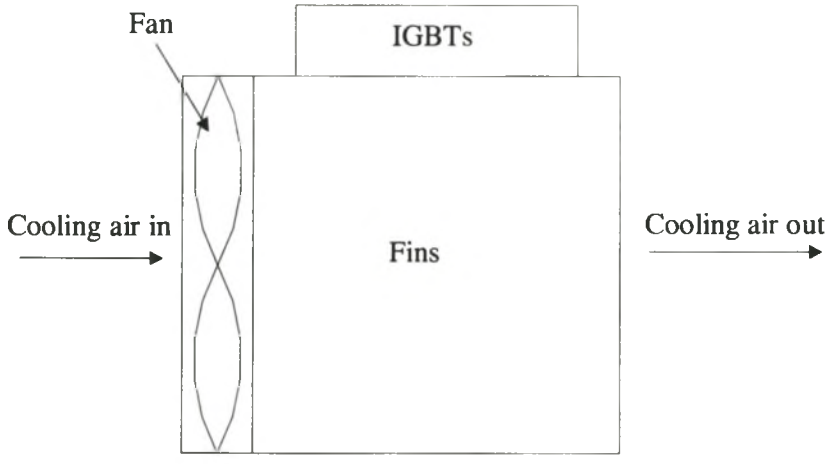

Figure 6.6 Cooling of the IGBTs using a fan and fins

It will be illustrated how a commercially available PHP product a "Stereo-type heat lane" can be used for the thermal control of the IGBTs. Figure 2.5, repeated below in Figure 6.7, shows the Stereo-type heat lane. It basically consists of a PHP sandwiched between two plates as was previously shown in Figure 2.4. The IGBTs are mounted on both sides of the Stereo-type heat lane as shown in Figure 6.7 and air is forced through the Stereo-type heat lane to cool the IGBTs. This concept of cooling is exactly the same as illustrated in Figure 6.6 except for the fact that in the case of the Stereo-type heat lane the fin temperature is more or less isothermal due to the low thermal resistance of the PHP so that the fin efficiency is much higher than traditional fins.

Test equipment has been constructed to investigate whether the Stereo-type heat lane would be able to maintain the case temperature of the IGBT at the specified 100 °C. Figure 6.8 shows the Stereo-type heat lane positioned in a testing duct with a metal block mounted onto the Stereo-type heat lane. A fan is connected to the duct to force air through the Stere-type heat lane. Electrical elements are inserted into the metal block to provide heat to simulate an IGBT. From tests conducted by De Villiers (2000) it was found that with an average air velocity of 2 m/s and an electrical heat input of 1 000 W that the surface temperature of the metal block does not exceed 100 °C. A traditional fin assembly used by the Department of Electrical Engineering at the University of Stellenbosch for the same purpose is 5 times larger than the Stereo-type heat lane. This method is therefore an effective space saving way of cooling IGBTs.

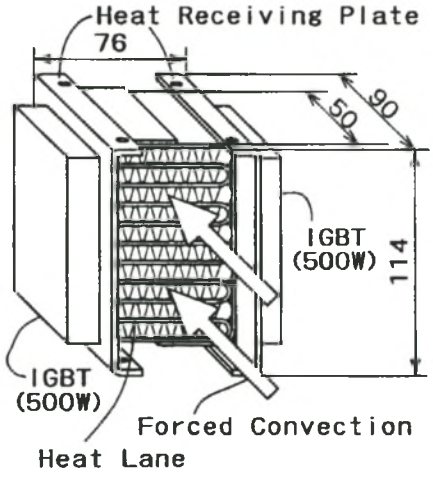

Figure 6.7 Cooling of IGBTs using a Stereo-type heat lane (Akachi and Miyazaki, 1997)

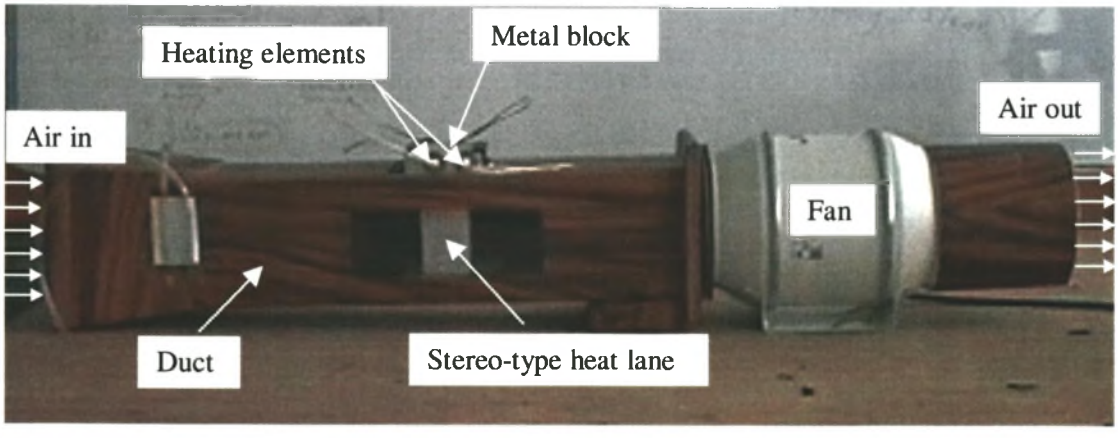

Figure 6.8 Test set-up for the evaluation of the Stereo-type heat lane

7 DISCUSSION AND CONCLUSIONS

The major focus area of this thesis was the development of a theoretical model to simulate PHPs and to compare the theoretical predicted heat transfer rate to the experimentally determined heat transfer rate. A theoretical model was developed consisting of a tube containing liquid plugs, vapour bubbles and a liquid film on the inner wall of the tube as shown in Figure 3.1. The governing equations were derived by considering the conservation of energy of the vapour bubbles and the liquid film, the conservation of momentum of the liquid plugs and the conservation of mass of the vapour bubbles.

As a liquid plug moves in a tube a film is deposited at the trailing end and if a film is present at the leading end some complex interaction exist between the liquid plug and the film. A strategy was developed to model this interaction which is illustrated in detail in section 3.2. It was assumed that a liquid film of a prescribed thickness is deposited at the trailing end of the plug and that a portion of the film at the leading end is sucked into the liquid plug. The strategy did not take the conservation of mass into account, i.e. the mass of the liquid plug remained constant despite the fact that mass leaves the plug to be deposited as a liquid film at the trailing end and that mass enters the plug as it moves across a film at the leading end. It is believed that this approach is acceptable since the mass of the film is much smaller than that of the liquid plug and the mass deposited as a film nullifies the mass entering the plug at the leading end.

Closely related to the interaction of the plug with the liquid film is the capillary force experienced by the liquid plug due to surface tension. When a liquid plug moves across an already wetted surface the contact angle at the leading end will be lower than when it moves across a dry surface. According to equation (2.9) the capillary pressure difference between the leading and trailing of the liquid plug will decrease as the leading contact angle decreases. This implies that the capillary force experienced by a liquid plug moving in a capillary tube will be smaller when the liquid plug moves across an already wetted surface. Information regarding the magnitude of the capillary force is not available. A conservative approach was followed, in which it was assumed that the liquid plug moves across a dry surface and that the maximum possible value for the advancing contact angle is 90° and the minimum possible value for the receding angle is 0°, to derive an expression which relates the capillary pressure difference between the advancing and receding end of the plug to the velocity of the plug.

To complete the theoretical model it is necessary to relate the vapour bubble pressure to its temperature, volume and mass and to model the evaporation and condensation processes. The vapour was modelled as an ideal gas. The pressure of the vapour bubble was therefore related to its temperature, volume and mass using the ideal gas equation. To model the evaporation and condensation processes two different equations were used. The one equation was derived from the kinetic gas theory which is mainly pressure difference controlled given by equation (3.6), and dubbed the kinetic mass transfer model, and the other equation is temperature difference controlled given by equation (3.7), and dubbed the heat transfer controlled mass transfer model.

The equations constituting the theoretical model were numerically solved using an explicit finite difference scheme as shown in section 3.2. A single plug PHP as shown in Figure 3.9 was modelled to investigate the effect of the choice of mass transfer model on the heat and mass transfer characteristics of a vapour bubble. It was found that for the heat transfer controlled mass transfer model that the vapour bubble temperature and pressure reached steady state values of 60 °C and 8 000 Pa respectively after $t \sim 200\ \mu s$. For the kinetic mass transfer model steady state values for the vapour bubble temperature and pressure of 60 °C and 18 000 Pa respectively, were attained after t ~ 3 s. The heat transfer controlled mass transfer model therefore attains steady state values for the temperature and pressure much faster than for the kinetic mass transfer model. The final pressure predicted by the heat transfer controlled mass transfer model is lower than predicted by the kinetic mass transfer model. The vapour bubble temperature overshot the temperature of the wall by ~ 8 °C in the case of the kinetic mass transfer model.

The single plug PHP shown in Figure 3.9 was used to investigate the effect of the initial position on the subsequent movement of the liquid plug for both the heat transfer controlled mass transfer model and the kinetic mass transfer model. It was found that the movement of the liquid plug is much more vigorous for the heat transfer controlled mass transfer model than for the kinetic mass transfer model as shown in Figure 3.12(a). On closer investigation it was found that the movement of the plug in the case of the heat transfer controlled mass transfer model is related to film dry-up as shown in Figure 3.13. The fact that the pressure of the vapour bubbles increases very quickly causing pressure pulses, also explains why the plug exhibits small oscillations. Numerical instabilities were encountered as the mass of the vapour bubbles became very small. A check was built into the program to ensure that the

mass of the vapour bubble could not decrease below a specified minimum mass (i.e. not become negative). As the time step was decreased the minimum mass could also be decreased. The time step and minimum vapour mass were decreased until the computer running time was only just acceptable (25 minutes computer running time to simulate 10 s).

Despite the initial plug position the liquid plug always moved to the centre of the tube and became stationary for the kinetic mass transfer model as shown in Figure 3.12(b). To understand the heat and mass transfer characteristics of the vapour bubbles better when using the kinetic mass transfer model and to attempt to achieve similar plug movement as the heat transfer controlled mass transfer model, the effect of the heat transfer coefficient h_{lfw} and the accommodation coefficient $\hat{\sigma}$ were investigated. It was found that as these parameters were increased that the vapour bubble temperature overshoot became more pronounced but attained a steady state value more quickly. The maximum value of the mass transfer rate increased and was achieved in a shorter time period as h_{lfw} and $\hat{\sigma}$ were increased. Despite these efforts the liquid plug movement was still not similar to that predicted by the heat transfer controlled mass transfer model and to the movement of the liquid plugs experimentally observed (see sections 5.2, 5.3 and 5.1).

Also using the single plug PHP the magnitude of the capillary force was determined and compared to the pressure and friction force in Figure 3.14. The average pressure force for this simulation was found to be $F_p = 7.03 \times 10^{-3}$ N, followed by the friction force $F_f = 5.73 \times 10^{-4}$ N and then the capillary force $F_c = 1.56 \times 10^{-5}$. It can be seen that the capillary force is negligible in comparison to the other forces.

The theoretical model, using the heat transfer controlled mass transfer model, was used to simulate a PHP consisting of several liquid plugs and vapour bubbles as shown in Figure 3.19. The effect of several parameters on the heat transfer rate of the PHP was studied using the theoretical model. These parameters included the working fluid, gravity, the filling ratio and the number of channels. Water and ammonia were used as the different working fluids. It was found that the movement of the liquid plugs is more pronounced when water instead of ammonia is used (refer to Figure 3.20 and Figure 3.22), however referring to Figure 3.23 the velocity achieved by the liquid plugs was higher for ammonia than water (Figure 3.21). As shown in Figure 3.24 it was found for ammonia that the heat transfer rate is quite insensitive to the inclination angle (and hence gravity) in contrast with water for which the effect can clearly be seen, in the bottom heat mode ($\phi = 90°$) the heat transfer rate is 1.4 times higher

than in the top heat mode (ϕ = -90°). The average heat transfer rate for all the tested inclination angles for ammonia was 80 W and for water 34 W. The theoretical model predicts that ammonia is superior to water as a working fluid.

The multi-plug PHP model shown in Figure 3.19 was used to determine the effect of the filling ratio on the heat transfer rate. The filling ratio was varied by varying the length of the liquid plugs as shown in Table 3.3. It is reasonable to believe that more liquid is present in the condenser section; hence the length of the liquid plugs in the condenser was chosen to be longer than in the evaporator. As shown in Figure 3.25 it was found that the heat transfer rate increases as the fill ratio decreases. For the heat transfer controlled mass transfer model the mass transfer rate is a function of the temperature difference between the liquid film and the vapour bubble and the area across which heat transfer takes place. The heat transfer rate will therefore increase as the area increases. The filling ratio is decreased by shortening the length of the liquid plugs therefore increasing the area where heat transfer can take place. In retrospect just by investigating the heat transfer mass transfer controlled model the effect of the filling ratio could have been predicted.

The effect of the number of channels on the heat transfer rate was also investigated using the theoretical model. From Figure 3.26 no definite conclusion could be made from the results, although the heat transfer rate should increase with the addition of channels due to the increase of the heat transfer area.

Several parameters were found to have an influence on the heat transfer rate of the PHP predicted by the theoretical model but were not thoroughly investigated. These parameters include d_i, L_e/L_c, δ_{lf}, δ_{dep}, L_{pe} and L_{pc}.

It was attempted to use the kinetic mass transfer model to simulate a multi-plug PHP but efforts to handle numerical instabilities that arose as the mass of the liquid film approached small values were unsuccessful. A strategy that was used to prevent this was to assign a minimum mass beyond which the mass of the liquid film was not allowed to decrease. Numerical instabilities still occurred despite considerably decreasing the time step. Efforts were then stopped due to the extremely long computer running times of 40 minutes for the simulation of 5 s (in hindsight this was the reason why the liquid film was taken to be the same as the wall temperature in the heat transfer controlled mass transfer model).

In Chapter 4 an experiment was conducted to determine the average thickness of the liquid film deposited on the wall at the trailing end of a water plug as it moves through a capillary tube due to gravity. The average thickness was correlated with the inside diameter of the tube, surface tension, average velocity of the plug and viscosity. It was found that the average thickness varied between 100 and 200 μm. Although the derived correlation is limited to a certain range of parameters and for water in a glass tube, an average thickness of 100 μm was used to model a stainless steel PHP with water as the working fluid. Since it was found that the film dry-up played an important role in the plug movement of a single plug PHP, an average film thickness of 10 μm was used to investigate the results of the theoretical model in section 3.3 to reduce computer run-time.

Several experiments were devised to verify the theoretical model and to visually observe the fluid motion. One such an experiment shown in Figure 5.1 was the investigation of the movement of a liquid plug in a vertically orientated U-shaped capillary tube and to predict the movement using the theoretical model. It was very difficult to control the initial conditions and it was found that the movement of the plug was quite different for similar initial conditions. However, it was possible to obtain initial conditions for which the plug movement was repeatable. The plug movement predicted by the theoretical model does not exactly match that observed experimentally as shown in Figure 5.3 but the final steady state position was predicted within 7.39%. For the theoretical model the kinetic mass transfer model was used. From the initial conditions shown in Table 5.1 it can be seen that only the one end of the liquid plug was exposed to the evaporator. In the actual experiment a liquid film was not observed on the tube inner wall. Evaporation initially occurred at the meniscus region of the liquid plug and not from a liquid film. To model the meniscus in the theoretical model an initial film was defined at the end of the liquid plug exposed to the evaporator as indicated in Table 5.1. As the liquid plug moved it was possible to see the liquid film deposited at the trailing end and to observe it evaporating.

An experiment was devised in which the movement of a liquid plug in a straight horizontal orientated tube was observed as shown in Figure 5.4. As was the case for the plug moving in the vertically orientated U-tube, it was very difficult to control the initial conditions of the plug. Different types of movement varying from regular oscillations with small amplitudes (~ 1 mm) to highly irregular oscillations with relatively large amplitudes (~ 50 mm) were

observed. Again it was possible to observe the deposition and evaporation of the liquid film at the trailing end of the plug.

A glass tube PHP as shown in Figure 5.5 was manufactured to visually observe the fluid motion inside the PHP. The liquid plugs always started to move vigorously for about 10 s after which it moved slowly back and forth. After a while the plugs started to move again or just kept on moving slowly back and forth. It was observed that some of the liquid plugs split up to form two separate plugs and that it is possible for two plugs to coalesce to form a single plug. The deposition and evaporation of the liquid film at the trailing end of the plugs were observed.

A closed end PHP as described in section 5.4 was constructed from stainless steel and filled with water as the working fluid. The heat transfer rate of the PHP was determined for different inclination angles, electrical power inputs and filling ratios. From the experimental data (Figure 5.10) it was seen that heat is not transferred steadily but in a "pulsating" fashion. To assist in the design of future PHPs a heat transfer coefficient h_{PHP} was defined and determined. The ideal situation would be to define a h_{PHP} in terms of the temperature difference between the inner wall of the tube and the internal fluid temperature and the heat flux. However, the internal fluid temperature was not experimentally determined and due to the very nature of the PHP the temperature of the internal working fluid is not constant. Some uncertainty surrounding the internal fluid temperature therefore exists. To compromise the heat transfer coefficient was defined in terms of the difference between the average evaporator and condenser temperature $\overline{T}_e - \overline{T}_c$, the heat transfer rate of the PHP $\dot{Q}_{PHP}$ and some average area based on the length of tube in the evaporator L_e and condenser L_c repeated here for convenience

$$\dot{Q}_{PHP} = \frac{h_{PHP}\pi d_i\left(\overline{T}_e - \overline{T}_c\right)}{\frac{1}{L_e} + \frac{1}{L_c}} \tag{7.1}$$

The heat transfer coefficient was found to be $100 < h_{PHP} < 500$ W/m^{2}K. Defining the heat transfer coefficient in terms of L_e and L_c immediately implies that the usage of the heat transfer coefficient is restricted to PHPs with similar geometry as the tested PHPs, but with limited information available the determined values can be used for design purposes.

The heat transfer coefficient defined by equation (7.1) was first correlated with $\overline{T}_e - \overline{T}_c$, ϕ and R to give equation (5.6) and then with $\overline{T}_e - \overline{T}_c$, ϕ, R and $(\overline{T}_e + \overline{T}_c)/2$ to get equation (5.7). It was found that the latter correlation fit the data better ($R^2 = 0.91$) than the former ($R^2 = 0.84$). The working fluid properties are related to $(\overline{T}_e + \overline{T}_c)/2$. Equation (5.7) therefore accounts for the properties of the working fluid and as a result is preferable to equation (5.6).

The theoretical model with the initial conditions and geometry in Table 5.2 was used to predict the heat transfer rate of the PHP as a function of the inclination angle. As shown in Figure 5.20 the theoretically predicted heat transfer rate compared well with the experimental values in the top heat mode ($-90° \leq \phi \leq 0°$) but not as good in the bottom heat mode ($0° < \phi \leq 90°$). The average experimental heat transfer rate in the top heat mode ($-90° \leq \phi \leq 0°$) was 62 W compared to 60 W predicted by the theoretical model. In the bottom heat mode ($0° < \phi \leq 90°$) the average experimental heat transfer rate was 65 W compared to the predicted value of 86 W.

A closed loop PHP as described in section 5.5 was manufactured from aluminium and filled with water as the working fluid. The heat transfer rate of the PHP was determined for varying electrical power input, inclination angle and filling ratio as shown in Figure 5.23. The values obtained for h_{PHP} were in the range $0 < h_{PHP} \leq 400$ W/m^{2}K. The heat transfer coefficient h_{PHP} was then firstly correlated with $\overline{T}_e - \overline{T}_c$, ϕ and R to give equation (5.8) and then with $\overline{T}_e - \overline{T}_c$, ϕ, R and $(\overline{T}_e + \overline{T}_c)/2$ to give (5.9). It was found that equation (5.8) ($R^2 = 0.86$) fitted the data slightly better than equation (5.9) ($R^2 = 0.87$). According to both correlations h_{PHP} will increase as ϕ decrease which is in contrast with the experimental results where the PHP was unable to transfer heat in some instances for lower ϕ. Just from investigating the results in Figure 5.23 it appears that h_{PHP} should increase with increasing ϕ. This contradiction indicates that the correlations given by equation (5.8) and (5.9) does reflect reality and should not be used.

In section 5.6 the closed end stainless steel PHP was filled with ammonia as working fluid. The heat transfer coefficient h_{PHP} was determined and is shown in Figure 5.29. It was found that the PHP was unable to transfer heat for $\phi \leq 0°$. From the experimental results it was concluded that the device is in fact not a PHP but operates as a thermosyphon. For the typical operating temperatures the internal diameter of the tubes should be less than 2.96 mm.

The inside diameter of the tubes used to construct the PHP was 3.34 mm which exceeds the required diameter. It is postulated that due to the slightly larger internal diameter it was not possible for liquid plugs to form due to surface tension inside the tubes. The flow inside the tubes was therefore stratified and whence the thermosyphon-like behaviour. The heat transfer coefficient h_{PHP} was then firstly correlated with $\overline{T}_e - \overline{T}_c$, ϕ and R to give equation (5.10) and then with $\overline{T}_e - \overline{T}_c$, ϕ, R and $(\overline{T}_e + \overline{T}_c)/2$ to give equation(5.11). Equation (5.11) (R^2 = 0.92) fits the data better than equation (5.10) (R^2 = 0.89). Equation (5.11) accounts for the properties of the working fluid by the inclusion of $(\overline{T}_e + \overline{T}_c)/2$ and as a result is preferable to equation (5.10)

A testing facility was built to demonstrate/evaluate the ability of the Stereo-type heat lane to maintain the temperature of an IGBT at an acceptable temperature. It was found that the use of the Stereo-type heat lane heat sink significantly reduces the size of systems currently used for the thermal management of IGBTs by a factor of 5.

8 RECOMMENDATIONS

In the theoretical model it was assumed that a liquid film of specified thickness is deposited at the trailing end of the liquid plug and that the film at the leading end is sucked into the liquid plug. Clearly this will cause the mass (and length) of the liquid plug to change. However, in the theoretical model the mass (and length) of the liquid plugs was constant. It is recommended that the effect of this assumption be further investigated.

The effect of d_i, L_e/L_c, $\delta_{\ell f}$, δ_{dep}, L_{pe} and L_{pc} on the heat transfer rate predicted by the theoretical model should be investigated in more detail by varying the parameters and determine how the heat transfer rate predicted by the theoretical model is influenced.

For the heat transfer controlled mass transfer model the energy equation for the liquid film is neglected and the temperature of the liquid film is taken to be equal to the wall temperature. It is recommended that the implications of this assumption be investigated by including the energy equation for the liquid film and to compare the heat transfer rate then predicted by the theoretical model to the heat transfer rate predicted with $T_{\ell f} = T_w$.

Currently only the heat transfer controlled mass transfer model is used in the modelling of multi-plug PHPs. It is recommended that the kinetic mass transfer model should also be used and the predicted heat transfer rate be compared to that of the heat transfer controlled mass transfer model.

The theoretical model currently only caters for closed end PHPs. It is recommended that the model be extended to include closed loop PHPs.

The internal diameter of the PHPs is too great for ammonia to be used as working fluid. It is recommended that a PHP be constructed with $d_i < 2.5$ mm to allow for ammonia to be used as working fluid.

To get an indication of the working fluid temperature it is recommended that the working fluid temperature be measured at several locations along the PHP. The results should be interpreted cautiously since at anytime liquid or vapour could be present at the position where a temperature reading causing different temperature readings.

If it is found that the temperature of the IGBTs in CAE's HEV exceeds its limit during the HEV's testing phase, it is recommended that a study should be conducted to determine the feasibility of controlling the temperature of the IGBTs using a Stereo-type heat lane.

In the case of the batteries several cooling concepts have been proposed and should be considered if it is found that the temperature of the batteries is out of the specified range during the testing phase of the HEV.

9 REFERENCES

Adamson, W. H. *Physical Chemistry of Surfaces*. John Wiley & Sons, 1990.

Akachi, H. and Miyazaki, Y. Stereo-Type Heat Lane Heat Sink. 10th Int. Heat Pipe Conf., Stuttgart, 21-25 September 1997.

Akachi, H. and Polášek, F. Pulsating Heat Pipes. *5th International Heat Pipe Symposium*, Melbourne, Australia, 17-20 November 1996.

Akachi, H. and Polášek, F. Thermal Control of IGBT Modules in Traction Drives by Pulsating Heat Pipes. 10th Int. Heat Pipe Conf., Stuttgart, 21-25 September 1997.

Blake, T. D. and Haynes, J. M. Kinetics of Liquid-Liquid Displacement. *J. Colloid Interface Sci.*, 30, 421, 1969.

Çengel, Y. A. and Boles, M. A. *Thermodynamics: An Engineering Approach*. McGraw-Hill, 1994.

Burch, S. D., Parish, R. C. and Keyser, M. A. Thermal Management of Batteries Using Variable-Conductance Insulation (VCI) Enclosure. *The Intersociety Energy Conversion Engineering Conference*, Orlando, Florida, July 31 – August 4, 1995.

Burelbach, J. P., Bankoff, S. G. and Davis, S. H. Nonlinear Stability of evaporating/condensing liquid films. *J. Fluid Mech*, vol. 195, pp. 463-494, 1988.

Carey, V. P. Liquid-vapour Phase Change-Phenomena: An Introduction to the Thermophysics of Vaporization and Condensation Processes in Heat Transfer Equipment. Hemisphere, 1992.

Charoensawan, P., Terdtoon, P., Tantakom, P., Ingsuwan, P. and Groll, M. Effects of Inclination Angles, Filling Ratios and Total Lengths on Heat Transfer Characteristics of A Closed-Loop Oscillating Heat Pipe. *Preprints of the 6th International Heat Pipe Symposium*, Chiang Mai, Thailand, 5-9 November 2000.

De Villiers, J. F. *Cooling of Electronics Using Pulsating Heat Pipes*. Pre-graduate Thesis, University of Stellenbosch, 2000.

Dobson, R. T. and Harms, T. M. Lumped parameter analysis of closed and open oscillatory heat pipes. *11th Int. Heat Pipe Conf*, Tokyo, 12-16 Sept. 1999.

Dunn, P. D. and Reay, D. A. *Heat Pipes*. Pergamon, 1994.

Faghri, A. *Heat Pipe Science and Technology*. Taylor & Francis, 1995.

Friz, G. On the Dynamic Contact Angle in the Case of Complete Wetting. *Z. Angew. Phys*, 19, 374, 1965.

Gutoff, E. B. and Kendrick C. E. Dynamic Contact Angles. *AIChE Jornal*, Vol. 28, No. 3, 1982.

Kandlikar, S. G., Shoji, M. and Dhir, V. K. *Handbook of Phase Change: Boiling and Condensation*. Taylor & Francis, 1999.

Holm, F. W. and Goplen S. P. Heat Transfer in the Meniscus Thin Film Transition Region. *J. Heat Transfer*, vol. 101, pp. 543-547, 1979.

Kawabata, K., Niekawa, J. and Watanabe, K. Variable Conductance Heat Pipe (VCHP) for Cooling Sodium-Sulfur (NAS) Batteries. *10th Int. Heat Pipe Conf.*, Stuttgart, 21-25 September 1997.

Khrustalev, D. and Faghri, A. Heat Transfer During Evaporation on Capillary Grooved Structures of heat Pipes. *J. Heat Transfer*, vol. 117, pp. 740-747, 1995.

Kobayashi, Y., Ikeda, S. and Iwasa, M. Evaporative Heat Transfer at the Evaporative Section of a Grooved Heat Pipe. *Journal of Thermophysics and Heat Transfer*, vol. 10 no. 1, January-March 1996.

Maezawa, S., Izumi, T. and Gi, K. Experimental Chaos in Oscillating Capillary Tube Heat Pipes. *10th Int. Heat Pipe Conf.*, Stuttgart, 21-25 September 1997.

Maezawa, S., Sato, F. and Gi, K. Chaotic Dynamics of Looped Oscillating Heat Pipes. *Preprints of the 6th International Heat Pipe Symposium,* Chiang Mai, 5-9 November 2000.

Mills, A. F. *Heat Transfer*. Irwin, 1992.

Paul, B. Compilation of Evaporation Coefficients. *ARS J.*, vol. 32, pp. 1321-1328, 1962.

Peterson, G. P. *An Introduction to Heat Pipes*. John Wiley & Sons, 1994.

Richter, C. *Thermal management of Hybrid Electrical Vehicles Using Heat Pipes*. Pre-graduate Thesis, University of Stellenbosch, 2000.

Schneider, M., Khandekar, S., Schäfer, P., Kulenovic, R. and Groll, M. Visualisation of Thermofluiddynamic Phenomena in Flat Plate Closed Loop Pulsating Heat Pipes. *Preprints of the 6th International Heat Pipe Symposium*, Chiang Mai, Thailand, 5-9 November 2000.

Solov'ev, S. L. and Kovalev, S. A. Mechanism of Evaporation of a Liquid From a Porous Surface. *Proc. 5th Int. Heat Pipe Conf.* Tsukuba, Japan, 1984.

Strogatz, S. H. *Nonlinear Dynamics and Chaos*. Addison-Wesley, 1995.

Sukhatme, S. P. and Rohsenow, W. M. Heat transfer during film condensation of a liquid metal vapor. *J. Heat Transfer*, vol. 88, pp. 19-28, 1966.

Swanepoel, G., Taylor, A. B. and Dobson, R. T. Theoretical Modelling of Pulsating Heat Pipes. *Preprints of the 6th International Heat Pipe Symposium*, Chiang Mai, Thailand, 5-9 November 2000.

Wong, T. N., Tong, B. Y., Lim, S. M. and Ooi, K. T. Theoretical Modelling of Pulsating Heat Pipe. *11th Int. Heat Pipe Conf. Tokyo, 12-16 Sept. 1999.*

Yaws, C. L. *Chemical Properties Handbook*. McGraw-Hill, 1999.

Zuo, Z. J., North, M. T. and Ray, L. *Combined Pulsating and Capillary Heat Pipe Mechanism for Cooling of High Heat Flux Electronics*. http:\\www.Thermacore.com. 2001.

APPENDIX A FILLING AND DISCHARGING PROCEDURE: WATER

To fill the PHP with water the water is first treated to remove as much non-condensable gasses as possible. This is done by first boiling the water and allowing it to cool down. This cycle is repeated at least 5 times. After the boiling process sufficient water (fill ratio amount plus 10 g) is poured into the filling cylinder shown in Figure A.1. The filling cylinder is heated with the valve in the open position. After a while boiling of the water commences. The valve is firmly closed to prevent any non-condensable gasses from entering the cylinder. The mass of the remaining water in the cylinder is weighed using a Mettler P10 scale (serial no. 402455 and store no. 047287). The boiling-off of the water is repeated until the desired mass plus 2-5g is still in the cylinder to cater for wastage during the filling procedure. (From experience it was found that 2-5g is trapped in the piping and fittings during the filling procedure.)

Figure A.1 Water filling cylinder

The diagram in Figure A.2 shows how the PHP is connected to a vacuum pump (Galileo model Vacsound D08, serial no. 200142 and store no. 308502) and the cylinder containing water. Valve 1 and 4 are closed and 2 and 3 are opened. A vacuum is then drawn. After drawing the vacuum valve 3 is closed. After closing valve 3 valve 4 is opened allowing the water to flow into the PHP. After the PHP is filled valve 2 is closed.

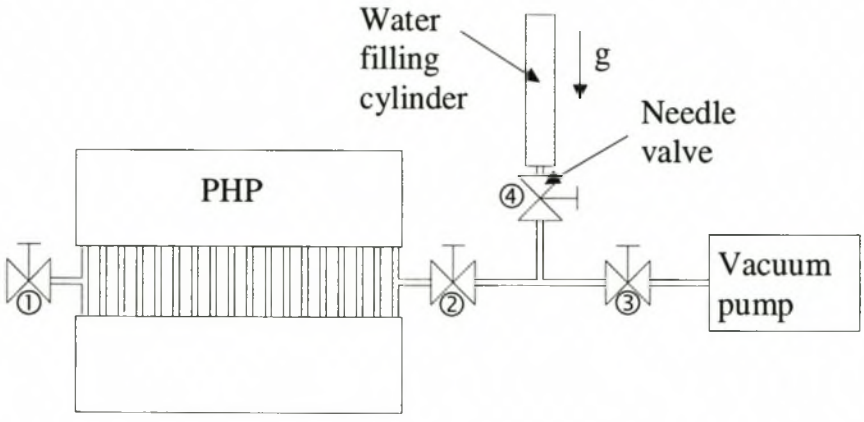

Figure A.2 Diagram for the filling procedure of the PHP with water

At this stage the exact filling ratio is unknown. After carrying out the testing a cylinder containing pressurised nitrogen is connected to valve 2 as shown in Figure A.3. A container is positioned at the outlet valve and valves 1, 2 and 3 are opened. The liquid content of the PHP is emptied into the container. A lightweight container should be used to accurate determine the liquid mass. For this purpose a standard plastic cup was used. The water in the container is then weighed using a Precisa 40SM-200A scale (serial no. 73464 and store no. 248173), which is more sensitive than the Mettler scale, and the filling ratio is determined. Pressurized nitrogen is preferred above normal pressurized workshop air due to the possibility that unwanted elements such as oil might enter the PHP when using pressurized workshop air.

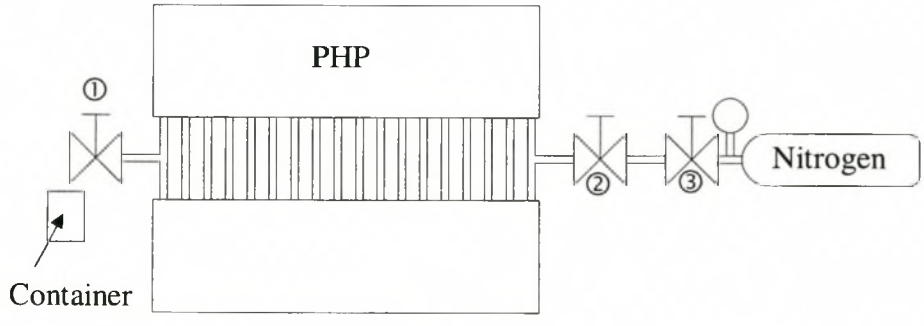

Figure A.3 Diagram for discharging procedure of water filled PHP

APPENDIX B FILLING AND DISCHARGING PROCEDURE: AMMONIA

The PHP is inserted into ice to further reduce the pressure and the cylinder containing ammonia is heated by inserting it in warm water until the pressure increases to 1500 kPa. The diagram in Figure B.1 shows how the PHP is then connected to a vacuum pump and cylinder containing ammonia. Valve 1 and 4 are closed and valve 2 and 3 are open. A vacuum is drawn in the PHP. Valve 2 is closed. Valve 1 is opened to fill the PHP. Valve 1 and 3 are then closed.

The PHP is weighed before and after the filling procedure to determine the mass of ammonia in the PHP.

To determine different filling ratios a (*strengthless*) plastic bag of known volume is connected to valve 4. Valve 4 is opened to slowly fill the plastic bag. The mass of the ammonia vapour is estimated from the ideal gas law. Ammonia vapour is let out until the desired amount of vapour is still in the PHP and the PHP is then tested. To test the next filling ratio the process is repeated. This is repeated for all the desired fill ratios. The PHP is then emptied still using the bag. When the PHP is completely empty the mass per bag is determined by dividing the number of times the bag was filled into the mass of ammonia originally in the PHP. In this way a good estimation can be obtained for the filling ratios.

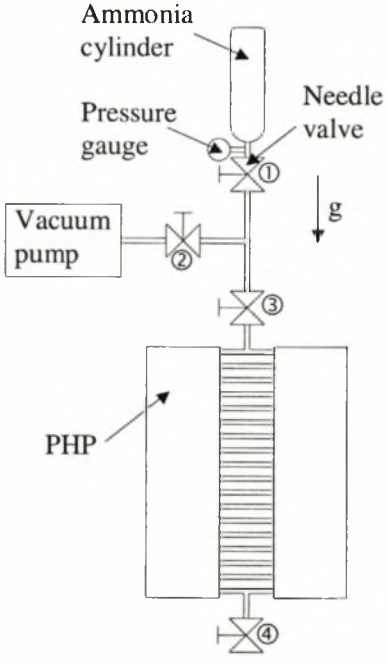

Figure B.1 Diagram for the filling procedure of the PHP with ammonia

APPENDIX C SAMPLE CALCULATION FOR THE PHP HEAT TRANSFER COEFFICIENT h_{PHP}

The sample calculation h_{PHP} will be done from the experimental calculations obtained for the stainless steel open loop PHP operated at and angle of ϕ = -30° and filling ratio of R = 0.56. The experimental numerical values required for the calculation are summarised in Table C.1. To determine h_{PHP} the thermal resistance diagram in Figure 5.13 has to be solved. For convenience the diagram will be redisplayed below in Figure C.1.

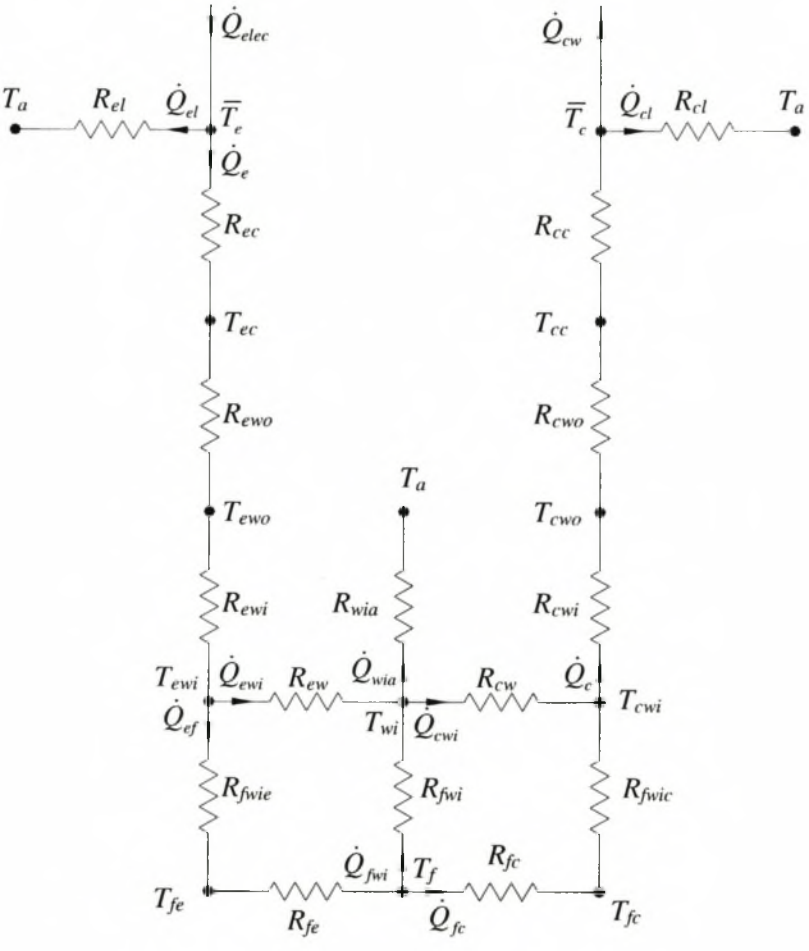

Figure C.1 Thermal resistance diagram of the PHP test set-up

To solve the thermal resistance diagram in Figure C.1 an estimation has to be made for the R_{wia}. The resistance R_{wia} consists of the sum of the resistance due to conduction through the insulation and the convective heat transfer from the outer surface of the insulation to the environment

$$R_{wia} = \frac{\delta_{ins}}{k_{ins} 2W_a L_t} + \frac{1}{h_c 2W_a L_t} \tag{C.1}$$

In equation (C.1) δ_{ins} is the thickness of the insulation, k_{ins} is the thermal conductivity of the insulation and h_c is the convective heat transfer coefficient between the outer surface of the insulation and the environment. R_{wia} is determined by following an iterative procedure. It is assumed that the temperature of the inner surface of the insulation is equal to T_{wi} and that T_{wi} = 0.5($\overline{T}_e + \overline{T}_c$) = 0.5(66.5 + 23.6) = 39.5°C. The outside surface temperature of the insulation is guessed as T_{io} = 20.78°C. R_{wia} will be a minimum when the PHP is operated at an angle of $\phi = \pm 90°$. At this angle the heat transfer coefficient h_c will be a maximum. Mills (1992) gives the Nusselt number for natural convection from a vertical heated surface as (Item 8 Table 4.10)

$$Nu = 0.68 + 0.67\left(\frac{\beta(T_{io} - T_a) g W_a^3}{\nu^2} \Pr \left[1 + \left(\frac{0.492}{\Pr} \right)^{9/16} \right]^{-16/9} \right)^{0.25} \qquad (C.2)$$

The fluid properties in equation (C.2) is calculated at the average temperature between the outer surface temperature and the ambient temperature T_{ave} = 0.5(T_{io} + T_a) = 0.5(22.78 + 17.3) = 20.04°C. From Table A.7 in Mills (1992) the fluid properties are Pr = 0.69, ν_{air} = 14.77 x 10^{-6} m^2/s and k_{air} = 0.0261 W/mK. The thermal coefficient of volume expansion is calculated as β = 1/(T_{ave} + 273.15) = 3.411 x 10^{-3} K^{-1}. Substituting these values into (C.2) the Nusselt number is Nu = 12.644. The heat transfer coefficient follows from the Nusselt number h_c = k_{air} x Nu /W_a = .0261 x 12.644/0.08 = 4.125 W/m^2K. Substituting the numerical values into (C.1) R_{wia} = 19.174 K/W. With R_{wia} known the heat losses to the environment can be determined $\dot{Q}_{wia}$ = (T_{wi} – T_a)/ R_{wia} = (41.9 – 17.3)/19.174 = 1.28 W. With the heat losses known the outside surface temperature of the insulation can be calculated by solving $\dot{Q}_{wia}$ = (T_{wi} – T_{io})/($\delta_{ins}/k_{ins}2W_aL_t$) for T_{io} to get T_{io} = T_{wi} - $\dot{Q}_{wia}$ ($\delta_{ins}/k_{ins}2W_aL_t$) = 41.9 – 1.28 x 0.0254/(0.03 x 2 x 0.08 x 0.355) = 22.776°C. The difference between the calculated and guessed value for T_{io} is acceptable and therefore no further iterations are required. The heat loss $\dot{Q}_{wia}$ is small relative to the electrical power input $\dot{Q}_{elec}$ and is therefore negligible. Consequently $\dot{Q}_{fwi}$ may also be approximated as zero.

The conduction resistance R_{ec} will now be estimated. It is assumed that the tubes may be approximated as a buried cylinder as in Item 8 in Mills (1992). Mills (1992) defines a shape factor S so that $\dot{Q} = \underline{kS}\Delta T = \Delta T/(1/kS) = \Delta T/ R_{ec}$. The shape factor is given by

$$S = \frac{2\pi L_e}{\cosh^{-1}(2h/d_o)} \qquad (C.3)$$

where h is the depth at which the cylinder is buried

Substituting numerical values into (C.3) the shape factor is S = 2 x π x 1.957/(acosh^{-1}(2 x 0.01/0.00476) = 5.816 m so that R_{ec} = 1/$k_{al}S$ = 1/(200 x 5.816) = 8.597 x 10^{-4}. R_{el} is determined from the heat loss calibration curve in Figure 5.16 as R_{el} = 1/0.2433 = 4.11 K/W. The heat losses from the evaporator is determined as $\dot{Q}_{el} = (\overline{T}_e - T_a)/R_{ec}$ = (66.5 – 17.3)/4.11 = 11.97 W. With the losses known the heat conducted to the outer wall of the PHP is $\dot{Q}_e = \dot{Q}_{elec} - \dot{Q}_{el}$ = 100 – 11.97 = 88.03 W. The temperature just before the outer wall temperature can now be determined by solving $\dot{Q}_e = (\overline{T}_e - T_{ec})/R_{ec}$ as $T_{ec} = \overline{T}_e$ - $\dot{Q}_e$ R_{ec} = 66.5 – 88.03 x 8.597 x 10^{-4} = 66.42°C. It can be seen that the temperature drop $\overline{T}_e$ - T_{ec} = 66.5 – 66.42 = 0.08°C is negligible. Since the tubes were cast into the evaporator section it will be assumed that good thermal contact exists between the evaporator section and the outer wall of the PHP tubes so that $R_{ewo} \approx 0$ and $T_{ewo} \approx T_{ec}$.

The resistance for the conduction through the tube wall is given by $R_{ewi} = \ln(d_o/d_i)/(2\pi L_e k_t)$ = ln(4.76/3.34)/(2 x π x 1.957 x 15) = 0.0019 K/W. The difference between the outer and inner wall temperature is determined from $T_{ewo} - T_{ewi} = R_{ewi}\ \dot{Q}_e$ = 0.0019 x 88.03 = 0.169 K which is negligible. So far it had been shown that $\overline{T}_e \approx T_{ewi}$ and that $\dot{Q}_{wia} \approx \dot{Q}_{fwi} \approx 0$ W. It can be similarly be shown that $\overline{T}_c \approx T_{cwi}$. Taking these approximations into account the thermal resistance diagram in Figure C.1 reduces to that shown in Figure 5.14 repeated in Figure C.2 for convenience.

From Figure C.2 the heat conducted by the wall is given by $\dot{Q}_w = (\overline{T}_e - \overline{T}_c)/R_w$ where $R_w = W_a/(k_t \frac{1}{4}\pi(d_o^2 - d_i^2)n_{tubes})$ = 0.08/(200 x 0.25 x π x (0.004762 – 0.003342) x 16) = 36.9 K/W. The heat conducted by the tube walls is therefore $\dot{Q}_w$ = (66.5 – 23.6)/36.9 = 1.163 W which is negligible but will be taken into account to maintain a generic approach for the solution of h_{PHP} since $\dot{Q}_w$ will not be negligible for the aluminium closed loop PHP where the conductivity of the aluminium tube is much higher than that of the stainless steel tube in this case.

The heat transferred by the PHP is now determined from $\dot{Q}_{PHP} = \dot{Q}_{elec} - \dot{Q}_{el} - \dot{Q}_{w}$ = 100 – 11.97 – 1.163 = 86.867 W. The PHP heat transfer coefficient is now determined from equation (5.4) as

$$h_{PHP} = \frac{\dot{Q}_{PHP}\left(\frac{1}{L_e}+\frac{1}{L_c}\right)}{\pi d_i\left(\overline{T}_e - \overline{T}_c\right)} = \frac{86.867\left(\frac{1}{1.957}+\frac{1}{1.435}\right)}{\pi d_i\left(66.5-23.6\right)} = 233\ \mathrm{W/m^2K} \qquad \text{(C.4)}$$

Table C.1 Values required for sample calculation

$\overline{T}_e$	66.5 °C
$\overline{T}_c$	23.6 °C
T_a	17.3 °C
$\dot{Q}_{elec}$	100 W
L_e	1.957 m
L_c	1.435 m
W_a	0.08 m
Pr	0.69
n_{tubes}	16
k_f	15 W/mK
k_{al}	200 W/mK
d_i	0.00334 m

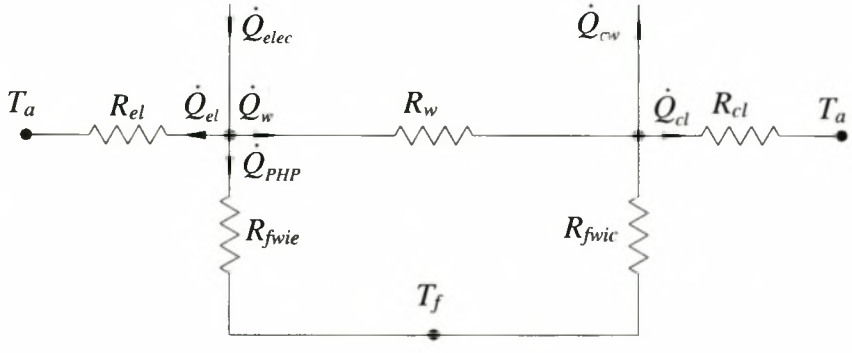

Figure C.2 Simplified thermal resistance diagram of the PHP test set-up

APPENDIX D COMPARISON BETWEEN CALCULATED AND ACTUAL ENTHALPY VALUES

Table D.1 shows the data obtained from steam tables in Çengel and Boles (1994), i_{vt} compared to the calculated values i_{vc}. The percentage difference is defined as $\Delta_{diff} = 100(i_{vc} - i_{vt})/i_{vt}$.

Table D.1 Comparison between calculated and tabulated enthalpy values for water vapour

Temperature [°C]	Pressure [Pa]	i_{vt} [J/kgK]	i_{vc} [J/kg/K]	$\Delta diff$
45.81	10 000	2584.7	2584.5	-0.0077
50	10 000	2592.6	2595.7	0.1196
100	10 000	2687.5	2774.2	3.2260
81.33	50 000	2645.9	2646	0.0038
100	50 000	2682.5	2710.6	1.0475
99.63	100 000	2675.5	2679.747	0.1587
100	100 000	2676.2	2681	0.1794

APPENDIX E FILLING PROCEDURE OF HORIZONTAL GLASS TUBE EXPERIMENTAL APPARATUS

To fill the horizontal tube valve 1 is closed and valve 2 and 3 are open. A vacuum pump is connected to valve 3 and a vacuum is drawn. Valve 2 and 3 are closed. The middle container is filled with ice water. Pentane is poured into the feeding tube. Valve 1 is slowly opened and the pentane is allowed to flow into the u-section. Valve 1 is closed when the u-section is filled with pentane. Care should be exercised during this step to ensure that air does not enter the u-section. The indicated container is filled with water warm water (~40 °C) and positioned to allow the u-section to be covered by the warm water. Valve 2 is slowly opened to allow the pentane to evaporate and condense in the cold region in the middle container. Valve 2 is closed when a liquid plug of the required length is obtained.

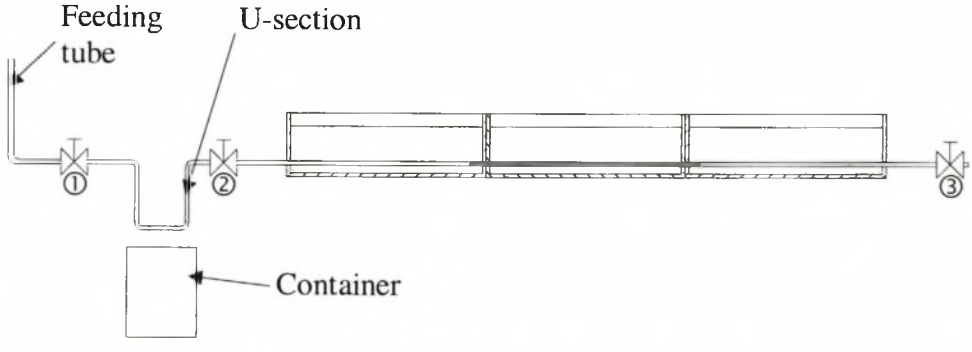

Figure E.1 Diagram for the filling procedure of the horizontal tube experimental apparatus

APPENDIX F FILLING PROCEDURE OF GLASS TUBE PHP

To fill the glass tube PHP valve 1 is closed and valve 2 is open and connected to a vacuum pump. A vacuum is drawn in the PHP and valve 2 is closed. Pentane is poured into the feeder tube. Valve 1 is opened to allow the pentane to flow into the PHP. Care should be exercised during this step to prevent any air from entering the PHP via the feeder tube.

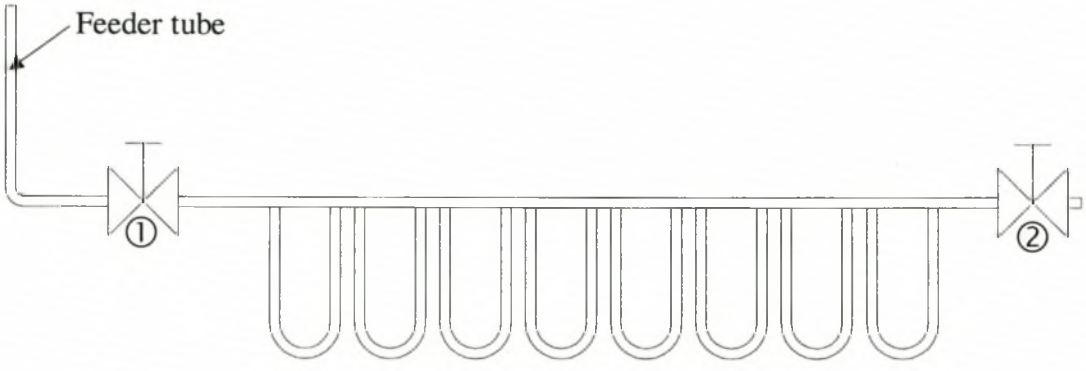

Figure F.1 Diagram for the filling procedure of the glass tube PHP